Growth of InAs/InP Nanowires by Molecular Beam Epitaxy

Growth of InAs/InP Nanowires by Molecular Beam Epitaxy

By

Christopher Michael Haapamaki, B.Eng,

A Thesis

Submitted to the School of Graduate Studies

in Partial Fulfilment of the Requirements

for the Degree

Doctor of Philosophy

McMaster University

©Copyright by Christopher Michael Haapamaki, December 2012

DOCTOR OF PHILOSOPHY (2012) McMaster University

(Department of Engineering Physics) Hamilton, Ontario

TITLE: Growth of InAs/InP Nanowires by Molecular Beam Epitaxy

AUTHOR: Christopher Michael Haapamaki, B.Eng, (McMaster University)

SUPERVISOR: Dr. Ray R. LaPierre

Abstract

InP nanowires with short InAs segments were grown on InP (111)B substrates by Au assisted vapour-liquid-solid (VLS) growth in a gas source molecular beam epitaxy system (GSMBE). Nanowire crystal structure and morphology were investigated by transmission electron microscopy as a function of temperature, growth rate, and V/III flux ratio. At 370°C predominantly kinked nanowires with random morphology and low areal density were observed with a rough parasitic 2D film. At 440°C, nanowire density was also reduced but the 2D film growth was smoother and nanowires grew straight without kinking. An optimum temperature of 400°C maximized areal density with uniform nanowire morphology. At the optimum temperature of 400°C, an increase in V/III flux ratio changed the nanowire morphology from rod-shaped to pencil like indicating increased radial growth. Growth rate did not affect the crystal structure of InP nanowires. For InAs nanowires, changing the growth rate from 1 to 0.5 μm/hr reduced the presence of stacking faults to as low as one per nanowire. Short InAs segments in InP nanowires were found to grow through two mechanisms for nanowires of length L and diameter D. The first mechanism described the supply of In to the growth front via purging of In from the Au droplet where $L \propto D$. The second mechanism involved direct deposition of adatoms on the nanowire sidewall and subsequent diffusion to the growth front where $L \propto D^{-1}$. For intermediate growth durations, a transition between these two mechanisms was observed.

For InP and InAs nanowires, the growth mode was varied from axial to radial through the inclusion of Al to form a core shell structure. $Al_xIn_{1-x}As(P)$ shells were grown on InAs cores with Al alloy fractions between 0.53 and 0.2. These nanowires were examined by transmission electron microscopy and it was found, for all values of x in InAs-$Al_xIn_{1-x}P$ structures, that relaxation had occurred through the introduction of dislocations. For InAs-$Al_xIn_{1-x}As$ structures, all values except $x = 0.2$ had relaxed

through dislocation formation. A critical thickness model was developed to determine the core-shell coherency limits which confirmed the experimental observation of strain relaxation.

The effects of passivation on the electronic transport and the optical properties were examined as a function of structural core-shell passivation and chemical passivation. The mechanisms for the observed improvement in mobility for core-shell versus bare InAs nanowires was due to the reduction in ionized impurity scattering from surface states. Similarly an increase in photoluminescence intensity after ammonium sulfide passivation was explained by the reduction of donor type surface states.

Acknowledgements

First and foremost I thank my colleagues in the LaPierre Group at McMaster University. My supervisor Dr. Ray LaPierre was responsible for engaging me in research as an undergrad and was able to transform me from a lost and unfocused student to an efficient, focused researcher. Perhaps most importantly he has strengthened my ability to think critically and for this I am forever grateful. The “figure it out, and do whatever it takes” approach to research is now permanently ingrained in my psyche. Thanks also go to the members of Team LaPierre past and present. I am thankful to have gained such a large group of great friends. Members of the “old guard”, Martin Plante, Hanna Budz, and Subir Ghosh were instrumental in the early years of my time at McMaster and I would like to specifically thank them for this. I look back fondly on those days in CRL basement. Thanks also go to my supervisory committee Dr. John Preston and Dr. Adrian Kitai for their valuable advice.

I would like to acknowledge in general the technical staff at McMaster University whom without this work would not have been possible. The maintenance of the equipment and training activities provided by these individuals were of paramount importance. For MBE growth I am deeply grateful to Brad Robinson for his guidance and for our many discussions. Naturally I am equally grateful to his successor Sharam Tavakoli. I would like to thank the staff in the Centre for Emerging Device Technologies Doris Stevanovic, Zhilin Peng for clean room related support and keeping everyone in the lab safe. Thanks go to Paul Dube for keeping the supply of liquid helium flowing, for his help chasing leaks, and for teaching me so much about cryogenics and vacuum systems. I thank all those from the CCEM for their assistance with electron microscopy, specifically Fred Pearson, Carmen Andrei, Steve Koprich, and Julia Huang. And last but not least from McMaster I thank the administrative staff in the Department of Engineering Physics and CEDT, Marilyn, Linda, Samantha, Nadine, Alex, and Fran.

A special thank you goes out to our collaborators from IQC for help in this work and for showing me the fascinating world of quantum information, specifically Dr. Jonathan Baugh for welcoming me into his lab.

Finally I must thank my family. My mother has been an unwavering pillar of support throughout this work, and without her this endeavour would not have been possible. I have received the same level of unconditional support from my partner Ashley, and I stress unconditional. Having a partner understand fully the parameters of a path makes said path much easier to traverse. The path was truly enjoyable and I could not imagine this experience without you...Loves. Thanks also go out to my brother and Don, for their understanding and support, and to my extended family. Thanks for being there.

I dedicate this work to my family and friends

Table of Contents

Abstract iii

Acknowledgements v

List of Figures xi

List of Tables xiii

Chapter 1 Introduction **1**

1.1 VLS Growth 2

1.2 Modern Approaches 5

1.3 Motivations of Present Work 6

1.4 Thesis Overview 8

Chapter 2 Growth and Characterization Techniques **11**

2.1 Molecular Beam Epitaxy (MBE) 11

2.2 Sample Preparation 13

2.3 Electron Microscopy 15

2.3.1 Scanning Electron Microscopy 17

2.3.2 Transmission Electron Microscopy 19

2.4 Micro-Photoluminescence Spectroscopy 20

2.4.1 Lasers 21

2.4.2 Optics 22

2.4.3 Spectrometer and Detectors 24

2.4.4 Cryostat 25

2.5 I-V Characterization 26

Chapter 3 Growth of InP and InAs Nanowires **29**

3.1 Introduction 29

3.2 Experimental Details 30

3.3 Results and Discussion 32

3.4 Conclusions 45

Chapter 4 InAs/AlInAs(P) Core-Shell Nanowires **46**

4.1 Introduction 46

4.2 Growth of InAs-AlInAs(P) Nanowires 49

4.2.1 Experimental Details 49

4.2.2 Results and Discussion 51

4.2.3 Summary 59

4.3 Strain Model 60

4.3.1 Martin Transformation 60

4.3.2 Core-Shell Nanowire Model 66

4.3.3 Results and Discussion 73

4.3.4 Summary 77

Chapter 5 Nanowire Passivation **78**

5.1 Introduction 78

5.2 Electron Transport 79
5.2.1 Introduction 79
5.2.2 Experimental Details 80
5.2.3 Results and Discussion 80
5.2.4 Conclusion 86
5.3 Ammonium Sulfide Passivation 87
5.3.1 Introduction 87
5.3.2 Experimental Details 88
5.3.3 Results and Discussion 89
5.3.4 Conclusion 90

Chapter 6 Conclusion and Future work **91**

6.1 Thesis Summary 91
6.2 Future Work 92

References **95**

Appendix A Strain Model Supplementary Information **105**

A.1 Derivation of Displacement Coefficients 105
A.2 MAXIMA Code 108
A.3 GNU Octave Code 111

List of Figures

1.1 Schematic of the VLS process 4

2.1 McMaster CEDT GSMBE schematic 14

2.2 SEM sample mounting geometry 18

2.3 Schematic representation of the μPL system. 21

2.4 Reflectance vs. wavelength for Thorlabs PF10-03-P01 mirror 23

2.5 Reflectivity vs. wavelength for the Thorlabs B NIR coating 23

2.6 Quantum efficiency (CCD detector) and responsivity (InGaAs photodiode) as a function of wavelength 25

3.1 SEM images of InP NWs 33

3.2 Nanowire height distributions as a function of V/III ratio 35

3.3 Bright field TEM images of InP NWs 36

3.4 HAADF image and EDX linescan of InAs segment in InP NW 37

3.5 Length versus diameter for Samples D and E 38

3.6 Length versus 1/diameter for Samples D and E 38

3.7 Length versus diameter of the InAs segment for Sample D and E . . . 39

3.8 HAADF image of Sample F 42

3.9 InAs segment length versus diameter for Sample F 44

4.1 SEM image of InAs-AlInAs NWs 52

4.2 BFTEM, HAADF, EDX of InAs-AlInAs(P) nanowires 53

4.3 HRTEM image showing dislocations and corresponding SAD pattern 56

4.4 Geometry of the InAs-$Al_xIn_{1-x}As(P)$ core shell system 67

4.5 Body element for a system described in cylindrical coordinates 69

4.6 $Al_xIn_{1-x}As$ critical shell thickness vs. InAs core diameter 74

4.7 SAD pattern for InAs-$Al_xIn_{1-x}As$ core-shell nanowires 76

4.8 SAD pattern for InAs-$Al_xIn_{1-x}P$ core-shell nanowires 76

5.1 Schematic representation of an InAs-AlInAs nanowire field effect transistor (NWFET). 81

5.2 SEM image of InAs-AlInAs NWFET 82

5.3 Conductance versus backgate voltage for core-shell nanowire FET Device 1 at various temperatures. 82

5.4 Pinchoff threshold voltage as a function of temperature for Device 1. . 84

5.5 Field effect and effective mobility versus backgate voltage for Device 1 at T = 14 K. 84

5.6 Peak effective electron mobility versus temperature for core-shell Devices 1-3. 85

5.7 Peak effective electron mobility versus temperature for unpassivated Devices 4-6. 87

5.8 Representative room temperature μPL spectra showing pre- and post-passivation results on a single nanowire. 89

6.1 HAADF image showing 5 InAs quantum dots grown axially in an InP nanowire, surrounded by a AlInAs shell lattice matched to InP. . . . 92

List of Tables

2.1 Specifications of the gratings installed in the spectrometer. 24

3.1 InP/InAs nanowire growth conditions 30

4.1 Description of InAs/AlInAs(P) nanowire samples 50

4.2 Non-zero components of the stiffness tensor c_{ij}. 66

5.1 Description of InAs-AlInAs and InAs nanowire FET devices. 81

Chapter 1

Introduction

Since the beginning of the electronic age, progress towards more advanced electronic devices and research into the fundamental physics underlying condensed matter have existed side by side. Both seemingly different pursuits, when examined closely, share many of the same architectures and methodologies. They share the same characterization tools, the same fabrication tools, and most importantly sit on the bleeding edge of innovation both theoretically and in terms of real world applications. It is this fact that has blurred the line between the engineer and the physicist. With this motivation, the development of nanostructures is being pursued very aggressively. New physics, and potential device improvements can be realized by “going small” and harnessing the effects of quantum mechanics. To observe and harness quantum mechanical effects however, systems must be electronically clean meaning that they are free from the disorder and defects that scatter electrons. The semiconductor crystal, with its close to perfect periodic lattice, ability to be doped, and high carrier mobility is a natural choice. Growth of semiconductor crystals is now a mature industry carrying with it a proud history of innovative discoveries and accomplishments. Specifically, the epitaxial growth of compound semiconductors, materials consisting of combinations of Group III and Group V elements by molecular beam epitaxy, have led the way. Pioneering engineering achievements such as the laser and the high electron mobility transistor, and Nobel prize winning condensed matter discoveries such as the fractional quantum hall effect share the same origin; the vacuum chamber of a molecular beam epitaxy system.

This introductory chapter will provide the reader with an overview of the history of nanowire growth beginning in Section 1.1 with the development of the vapour-liquid-solid (VLS) method. The transition into more modern interpretations of nanowire growth will be described in Section 1.2. A discussion in Section 1.3, of the motivations for the continued development of nanotechnology and the role that III-V nanowires can fill in that story, followed finally by an overview of this thesis, will be provided in Section 1.4.

1.1 VLS Growth

Prior to the 1960's the dislocation mediated growth method for crystals grown from vapour was widely accepted. At this time it was proposed as a mechanism for the growth of micron-diameter, millimetre-length whiskers. Eshelby showed that a screw dislocation could provide a self perpetuating spiral growth front by which the whisker would continuously elongate from the substrate [1]. This growth method is known as the Frank mechanism, and it describes the process whereby crystals grow at relatively low supersaturation due to the high adatom sticking coefficients on steps originating from screw dislocations. This approach was justified by showing that classical nucleation theory predicted supersaturations required to form monolayers that were much too high when compared to experiment [2]. In 1964 however the VLS method was proposed by Wagner and Ellis [3], and thereafter the Frank mechanism was put into question as the universally accepted growth method of whiskers [4]. VLS growth was described as a method by which Si whiskers with Au particles grew vertically from a Si $\langle 111 \rangle$ substrate when exposed to $SiCl_4$ vapour at elevated temperatures. This process was defined by three key ingredients: a) growth is not mediated by a screw dislocation, b) an impurity is required for crystal growth, and c) a solidified droplet exists at the whisker tip after growth. The Au particles were thought to form

low temperature liquid alloys with Si when the sample was heated and exposed to a supersaturated vapour. It was proposed that these alloys were formed by the preferential decomposition of the $SiCl_4$ precursors on the surface of the Au particle and the subsequent incorporation of Si. The constant supply of precursor molecules from the vapour, and the resulting excess Si in the Au particle creates a supersaturation, or driving force for nucleation under the particle resulting in a whisker.

In his seminal paper in 1975, Givargizov highlighted the fact that few papers after Wagner and Ellis omitted the VLS mechanism as responsible for whisker growth [5]. Givargizov outlined in great detail the temperature dependent kinetic aspects of the VLS mechanism. Many important aspects were addressed including the dependence of supersaturation on whisker diameter, poly-nuclear growth, the role of the liquid phase, and surface diffusion. One of the major observations made and quantified by Givargizov was the fact that whiskers below a critical diameter did not grow. This was explained by the Gibbs-Thompson effect where the supersaturation is dependent on the diameter of the Au particle. This is expressed as:

$$\Delta\mu = \Delta\mu_o - \frac{4\Omega\alpha}{d} \tag{1.1}$$

where $\Delta\mu$ is the supersaturation, $\Delta\mu_o$ is the supersaturation for the infinite plane case ($d \to \infty$), Ω is the atomic volume, α is the specific free energy of the vapour-solid interface, and d is the diameter of the particle. This was related to the growth rate V by empirical power law fits to observed data $V = b(\Delta\mu/kT)^n$, where b is independent of supersaturation. This results in an expression for growth rate by incorporating the Gibbs-Thompson effect from Equation (1.1):

$$V^{1/n} = \frac{\Delta\mu_o}{kT} b^{1/n} - \frac{4\Omega\alpha}{kT} b^{1/n} \frac{1}{d} \tag{1.2}$$

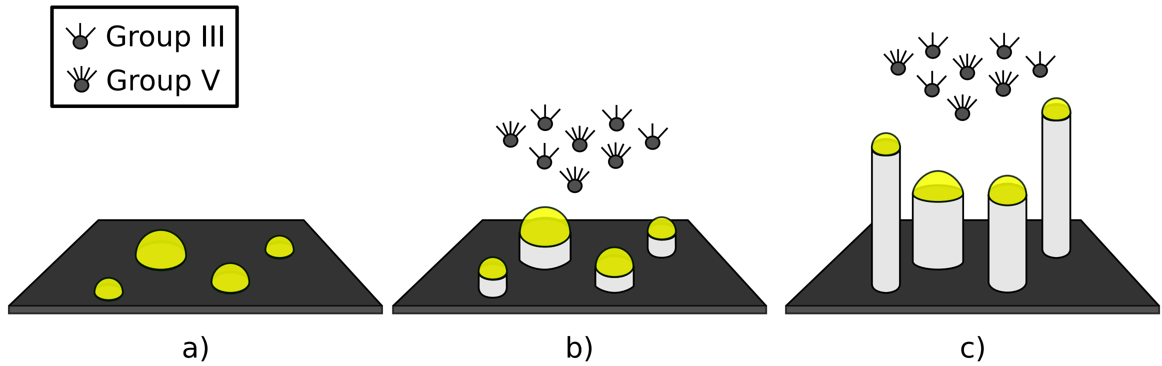

Figure 1.1: Schematic of the VLS process. a) Formation of gold nanoparticles and alloying with the substrate b) Growth initiated by supplying growth material c) Elongation of nanowires.

The data was fit to Equation (1.2) using $n = 2$. The critical diameters were obtained by estimating α and setting the growth rate equal to zero:

$$d_c = \frac{4\Omega\alpha}{\Delta\mu_o} \tag{1.3}$$

Yazawa and colleagues in 1992 extended the experimental work of Givargizov and ushered in what most would call the transition between the whisker era as described by Givargizov, Wagner and Ellis to the nanowire era [6]. They observed the growth of 20-30 nm diameter InAs nanowires on GaAs (111)B and InAs (111)B substrates [6,7]. These nanowires grew quite by accident. The researchers were using a reactive ion etching (RIE) process to fabricate mesh template structures in SiO_2 films. The same RIE tool was also used to fabricate GaAs transistors consisting of Au contacts for other work. It was believed that the Au atoms sputtered from the GaAs transistor contacts were deposited on the walls and the electrodes of the RIE tool, and were subsequently deposited on the substrates that resulted in seeds for nanowire growth. Another ground breaking discovery from this work was the discovery that III-V semiconductor nanowires could crystallize in the hexagonal wurtzite phase [8] rather than the commonly observed zincblende phase [9].

1.2 Modern Approaches

Modern interpretations of nanowire growth such as that of Dubrovskii et al. [10], built on and extended the Givargizov model describing the VLS mechanism. In this work they explored in great detail the nucleation processes that occurred on the facets at the liquid-solid interface, particularly for a mononuclear rather than a polynuclear growth process as described by Givargizov. Polynuclear processes were justified in micron size whiskers but not for nanowires having diameters two to three orders of magnitude smaller. They concluded that the driving force for the phase transition from liquid to solid is the supersaturation in the liquid droplet rather than that of the vapour as defined by Givargizov in Equation (1.1). Furthermore they showed that the limiting process is the liquid-solid boundary rather than the gas-liquid boundary. This model was able to explain the fact that thicker Si wires grew faster than thinner ones in the CVD $SiCl_4/H_2$ system. What it failed to describe was the opposite behaviour observed at the time in nanowires grown by molecular beam epitaxy (MBE) [11], chemical beam epitaxy (CBE) [12], and metalorganic vapour phase epitaxy (MOVPE) [13]. A model by Johansson in 2004 included a mass transport consideration, and an explanation that for MBE, CBE, and MOVPE, the Gibbs-Thompson effect can be neglected [14]. The Gibbs-Thompson effect can be included in the Hertz-Knudsen equation that governs the rate of attachment of atoms:

$$R(r_w) = \frac{P - P_\infty \exp(2\sigma\Omega/r_w kT)}{\sqrt{2\pi mkT}} \tag{1.4}$$

where P is the vapour pressure, P_∞ is the vapour pressure for infinite curvature, σ is the surface energy, Ω is the atomic volume, r_w is the nanowire radius, and m is the atomic mass. Johansson showed using a numerical example that at conventional MOCVD pressures and temperatures, P is four orders of magnitude larger than P_∞.

Stated differently, for a 10% decrease in $R(r_w)$ due to the Gibbs-Thompson effect, the nanowire radius would be on the order of 3 Å. This argument was also used to explain why the Gibbs-Thompson effect must be considered in Si whisker growth by $SiCl_4/H_2$ where P and P_∞ differ only by one order of magnitude. A paper by Dubrovskii in 2006 combined the diffusion induced effects with the nucleation mediated model of growth at the liquid-solid interface [15].

Since these pioneering models, there have been a number of important advances in the study of nanowire growth. It is well understood now why, and under what conditions, the wurtzite phase exists in nanowires [16, 17]. Much of the research on nanowires today involves the self-catalyzed method [18] where the Group III element plays the role of the Au particle. This method is advantageous for the integration of III-V materials with Si because it lends itself to lithography and it eliminates the need for Au. In Si, Au forms a deep level trap [19] and is typically not allowed in Si foundries [20].

1.3 Motivations of Present Work

The motivation for developing the growth and implementation of heterostructure nanowires is multifaceted, spanning from new electronic device architectures to exploring new and exotic types of condensed matter phenomena. The search for a post-Moore's law device architecture is a strong driving force for many researchers focusing on nanostructures. Moore's Law states the density of transistors on a chip will double every sixteen months [21]. There are crucial materials-, dimensional-, and processing-related challenges that are placing significant barriers to the progression of Moore's Law. At the current technology node, Si is the material of choice for the microelectronics industry and it is beginning to show some weaknesses. These issues

are outlined in great detail in the *International Technology Roadmap for Semiconductors* [21]. Until now the frequency of a CMOS device was increased from technology node to technology node by shrinking key dimensions in the device. The crucial dimension in a CMOS device is the planar Si/dielectric interface. By shrinking this dimension, the capacitance is increased and the frequency at which the channel can be modulated is increased. Traditionally this dielectric was SiO_2, which was only a couple of nanometres thick. Significant leakage via quantum mechanical tunnelling occurred in these devices causing significant heating. This challenge was briefly overcome through the use of high-κ dielectric materials, where for the same capacitance (and frequency) one could increase the thickness of the dielectric. Due to the limited electron mobility of Si, to reduce the channel transit time, the channel was simply shortened. This leads to short channel effects which reduce the performance of the device. Short channel effects can also be mitigated by abandoning the planar architecture for a wire- or fin-type gate architecture.

The shrinking of dimensions also provides a myriad of fabrication challenges. UV lithography, the mainstay of the microelectronics fabrication industry is becoming obsolete and new exotic, short wavelength sources are being developed. This requires the creation of new photoresists and developers, and other chemicals involved in the process. Nanowires are also being considered for non-CMOS device applications as well as quantum information processors [22], solar cells [23], and photodetectors [24].

The extension of Moore's law and the development of advanced fabrication techniques will always be limited by the rules of classical computation by classical physics; the manipulation of logic 1's and 0's represented by ON and OFF states of transistors to perform tasks. The candidate to replace classical computation is quantum computation. In quantum computation, logic 1's and 0's are represented by the quantum mechanical states of a quantum mechanical system. This could be the spin state

of an electron [25], the polarization of a photon [26], or states in a superconducting circuit [27]. Nanowires can play a role in all of these incarnations of quantum computation. Quantum dots can be formed artificially by gate electrodes along a nanowire and their respective spins can be manipulated using electric fields [28]. Nanowires can be used as sources of single entangled photons in optical quantum computing [29]. Finally, nanowires can form Josephson junctions with superconducting cavities [30] as potential sources of Majorana fermions [31] which can be used in topological fault tolerant quantum computing [32].

Ensemble nanowire devices are attractive as solar cells for a number of reasons. First, the light trapping ability of an ensemble of nanowires versus a planar film is increased dramatically [23]. Second, nanowire heterostructures can be grown which can serve as a basis for a multi-junction solar cell [33]. This ability to grow heterostructures is also driving interest in nanowire photodetectors [24], which can be easily integrated into traditional CMOS-Si imaging platforms.

1.4 Thesis Overview

The goal of this thesis is to study the growth, properties, and applications of InP and InAs nanowires. The large majority of nanowire research has focused on GaAs. Some of the challenges experienced with GaAs can be solved by using indium based semiconductors such as InP and InAs. InP is interesting because its electronic and optical properties are not dominated as much by surface effects as in GaAs. InP nanowires can also be grown with InAs quantum dots which have size dependent electrical and optical properties. This makes nanowire heterostructures a versatile solution for a wide range of optoelectronic device applications including photodetectors [24] and single photon sources [29]. The high electron mobility of InAs and its

strong spin orbit coupling allow fast readout and electrical manipulation of spin states making it an attractive material for spin qubit based quantum computing [25]. In all of these applications, surface effects can be damaging to device performance.

The experimental methods used in this thesis are described in Chapter 2. Here a description of sample preparation techniques are explored. The growth process is outlined and a general overview of epitaxy is provided. Finally, this chapter reviews characterization techniques including electron microscopy, micro-photoluminescence spectroscopy, and I-V characterization. Growth of axial InP/InAs heterostructure nanowires and an examination of the growth processes involved will be discussed in Chapter 3 which was published in Nanotechnology [34]. Two growth modes were observed in the growth of heterostructured wires. A purging mechanism was found to be responsible for the growth of short segments while a diffusion based model was responsible for longer segments. Understanding the growth mechanisms of short segments is important because nanowire quantum dot properties are very dimensionally sensitive. Structural passivation in the form of a core-shell nanowire will be discussed in Chapter 4 which was published in Journal of Crystal Growth [35]. The addition of Al was found to drastically increase the radial growth of the nanowire. A strain model was developed and a critical shell thickness based on material parameters and nanowire geometry will be justified. This model was compared with experiment and published on arXiv [36] (accepted for publication in Journal of Applied Physics). In the final chapter, Chapter 5, improvements in electrical transport published on arXiv [37] (accepted for publication in Applied Physics Letters) and improvements in photoluminescence published in Nanotechnology [38] will be discussed. In Chapter 4 and 5, passivation is presented as a crucial element in the implementation of nanowire devices. The low dimensionality of nanowires means that their surfaces play important roles. Dangling bonds act as non-radiative recombination centres for

carriers decreasing the performance of optoelectronic devices. Electron scatterers on the surface such as oxide trap states or surface roughness can reduce the mobility of electrons in high speed devices. Conclusions and future work will be presented in Chapter 6.

Chapter 2

Growth and Characterization Techniques

This chapter will review the methods used in this research to grow and characterize III-V semiconductor nanowires by MBE. The MBE process will be reviewed in general, and specifics will be provided for nanowire growth including sample preparation, pre-growth and growth conditions. Finally, characterization methods will be reviewed including electron microscopy, micro-photoluminescence spectroscopy, and I-V characterization.

2.1 Molecular Beam Epitaxy (MBE)

The word epitaxy can be broken into its two Greek roots: *epi* which means resting upon, and *taxis* which means arrangement. Epitaxy then is a process where a growing crystal or *epilayer* mimics the underlying crystal structure. In molecular beam epitaxy (MBE) crystals are grown in an ultra-high vacuum (UHV) environment (10^{-9} Torr) with very precise control over composition, doping and layer thickness. MBE was first created at Bell labs in the 1970's by Cho and Arthur [39] and was used to grow GaAs/AlGaAs and InGaAsP material systems for telecommunication applications. Today it is used to grow high quality crystals required for optoelectronic devices, high electron mobility transistors (HEMT) and heterojunction bipolar transistors (HBT). In this section, the growth of III-V materials by MBE will be discussed.

There are a number of variations of the MBE growth process which can be differentiated by how the adatoms are delivered to the growth substrate. The three main MBE categories are: solid source MBE (SSMBE), metalorganic source MBE (MOMBE), and gas source MBE (GSMBE). In SSMBE, vapour fluxes are generated by solid source effusion cells. The effusion cell consists of a cone shaped pryolytic boron nitride (PBN) crucible with a tantalum or molybdenum wire wrapped around it. The source material is placed in the PBN crucible and current is passed through the wire, which in turn heats and in most cases melts the source material. This creates a vapour pressure differential between the orifice of the effusion cell and the growth chamber which induces a flux of atoms towards the substrate. The impingement rate of adatoms on the substrate is determined by the source temperature. The ultra-high vacuum (UHV) environment in the MBE chamber ($\sim 10^{-9}$ Torr) ensures that the vapour flux from the effusion cell is in the molecular regime. This means that between the substrate and the lip of the effusion cell, the impinging atoms do not collide with any other atoms. Molecular beams of Group III, V, metal, and dopant species can be provided by solid source effusion cells. The major disadvantages with SSMBE exist with the P and As sources. A major logistic and safety issue is that the effusion cells must be constantly replenished which can be dangerous especially with As and P. Furthermore, the high vapour pressure of these materials causes them to be depleted rapidly requiring large effusion cells. This makes temperature control, and thus deposition rate, difficult to control. P and As solid sources also produce P_4 and As_4 tetramer beams which have low sticking coefficients requiring higher pumping capacities.

The second type of MBE system listed above is MOMBE. In MOMBE, metalorganic gas sources are used such as trimethylindium (TMI), trimethylgallium (TMG), and trimethylaluminum (TMA) for Group III and trimethylphosphine (TMP), teri-

arybutylarsine (TBA), and trimethylarsine (TMA) for Group V. These metalorganic species impinge on the growth substrate and undergo complicated pyrolysis reactions. The advantages of MOMBE are a two to three fold increase in growth rate over SSMBE, the UHV vacuum conditions are not as stringent so maintenance requirements are not as demanding, and P and As deposition is much easier [40]. The final type of MBE system is GSMBE. The MBE system at McMaster University in the Centre for Emerging Device Technologies (CEDT) is a GSMBE (SVT Associates [41]) and was used to grow all nanowires described in this thesis. In this system, Group III elements are supplied as monomers from solid source effusion cells. Group V species (P and As) are supplied as dimers (P_2 and As_2) cracked from hydrides (PH_3 and AsH_3) in a valved gas cracker. The valved gas cracker was first introduced by Panish in 1980 [42]. Compressed hydride gases are metered very accurately through mass flow controllers and sent to the gas cracker through a leak valve. Here the hydride gas is stripped of its hydrogen through thermal decomposition at 950°C to form dimers with the assistance of a Ta or Rh catalyst. The temperature and pressure of the gas cracker determines the ratio of the different possible decomposition products including D, D_2, D_4, and DH (where D refers to P or As).

2.2 Sample Preparation

Growth substrates in this thesis were single side polished, epi-ready, three inch diameter wafers, manufactured by AXT Incorporated [43]. In particular, S-doped InP (111)B (1 - 4 $\times$ 10^{18}cm^{-3}) or Zn-doped GaAs (111)B (1 - 5 $\times$ 10^{18} cm^{-3}) wafers were used. The distinction between GaAs and InP will be made in subsequent chapters. The wafers were removed from the evacuated bags and immediately treated by UV-ozone oxidation for 20 min to remove any hydrocarbon contamination and to grow a sacrificial oxide. The wafers were then dipped in buffered HF for 30 s to remove

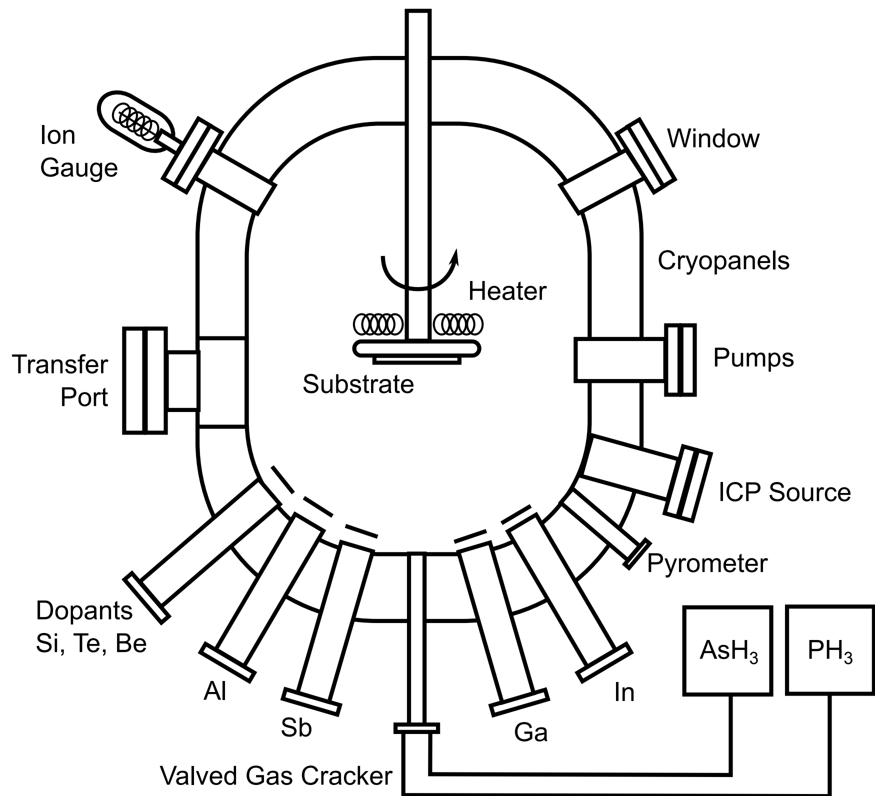

Figure 2.1: Schematic representation of the SVT Associates GSMBE system in the Centre for Emerging Device Technologies at McMaster University.

the oxide and rinsed under flowing deionized water for 10 min. The wafers were dried with N_2 and transferred to the load lock of an electron beam evaporator. The load lock was roughed with a mechanical pump to 50 mTorr and pumped further to 5×10^{-6} Torr by a turbo-molecular pump. The load lock valve was opened and the sample transferred into the deposition chamber maintained at a vacuum of 1×10^{-8} Torr. Here a 1 nm thick Au film was deposited at a rate of 0.1 nm s^{-1} as measured by a quartz crystal thickness monitor.

The three inch wafers were cleaved into six pie-shaped pieces sized to fit the custom made MBE sample holder. To begin, a small scratch was made on the polished side perpendicular to the major flat with a diamond scribe. With wafer tweezers, the wafer was placed upside down in a parabolic dish. With the long edge of the wafer tweezers, light pressure was applied to the major flat where the small scratch was made causing the wafer to cleave in half. A replica of the custom MBE sample holder was used to cleave the two half pieces into three pie-shaped pieces. Details of the MBE pre-growth and growth conditions are specific to the type of substrate and the type of nanowires being grown. These details will be provided in the subsequent chapters.

2.3 Electron Microscopy

Due to the size of the nanowires, and the level of structural information required to successfully characterize them, electron microscopy is used. The feature size accessible to a microscopic technique depends on the wavelength of the illumination source and the size of the aperture. This concept is described by the Rayleigh criterion. It states that for a diffraction limited image, two adjacent objects can be resolved if their centres are no nearer than the angular radius of the Airy disc [44]. For a circular

aperture we integrate over the entire area to determine the amplitude and square it to obtain the irradiance. We find that it is dependent on the *Bessel function of the first kind*:

$$I = I_o \left(\frac{2\mathrm{J}_1(\gamma)}{\gamma} \right)^2, \qquad \text{where } \gamma = \frac{1}{2} kD \sin\theta \tag{2.1}$$

The first minimum in this Airy pattern is at $\gamma = 3.832$. Rearranging the expression for γ we obtain the Rayliegh criterion:

$$(\Delta\theta)_{min} = \frac{1.22\lambda}{D} \tag{2.2}$$

where λ is the wavelength of light, and D is the diameter of the aperture. These sources can only be resolved if the maxima of the adjacent aperture pattern is no closer than the minimum of the pattern of the first aperture. For optical microscopy under optimum conditions, this separation is on the order of the wavelength of visible light. As a result, nanowires must be imaged with a source with a much smaller wavelength. Electrons can be used for this purpose which have a relativistic wavelength of:

$$\lambda = \frac{h}{2m_e eV \left(1 + \frac{eV}{2m_e c^2}\right)} \tag{2.3}$$

where m_e is the rest mass of the electron, e is the electron charge, V is the accelerating voltage, and h is Planck's constant. For the microscopes used in this thesis, accelerating voltages were 120 and 200kV corresponding to an electron wavelength of 0.00335 and 0.00251 nm, respectively [45]. This is five orders of magnitude smaller than optical wavelengths allowing the imaging in some cases of individual atoms. The resoltution in electron microscopes is limited in practice due to lens aberrations.

2.3.1 Scanning Electron Microscopy

To determine basic morphology, height distribution, and nanowire density, samples were examined by scanning electron microscopy (SEM). A JEOL 7000F SEM equipped with a field emission gun operating in secondary electron mode was used. Secondary electrons, generated by inelastic scattering from electrons in the sample are generated within the first few nanometres [46]. An electron beam is scanned over the sample surface and an Everhart-Thornley type secondary electron detector is used to analyze the secondary electron yield from each point in the scan. First, a positively biased wire screen ($\sim$ 100V) attracts secondary electrons emitted from the sample. The electrons are accelerated past the grid and collected into a scintillator. A scintillator consists of a cathodoluminescent material where the electrons are converted into light. The light emitted from the scintillator is passed on to the photo-cathode of a photomultiplier tube (PMT). Here the light is converted back to electrons, amplified by dynodes, and detected at the anode.

To prepare the samples for SEM, a small piece was cleaved from the growth substrate. This was performed by scribing a line parallel to the edge of the triangular wafer (i.e. [011]) using a diamond scribe. The wafer was then turned over and placed in a parabolic dish. Slight pressure was applied to the bottom of the wafer near the scribe mark. The cleaved bar was then divided up again into smaller pieces. These smaller pieces were secured on an aluminum stub using carbon tape or silver paste. The aluminum stub had a face cut at a 45° angle allowing views at normal, 45°, and 90° incidence as illustrated in Figure 2.2. Nanowire heights and spatial distributions were measured using the scale bars generated by the SEM image software.

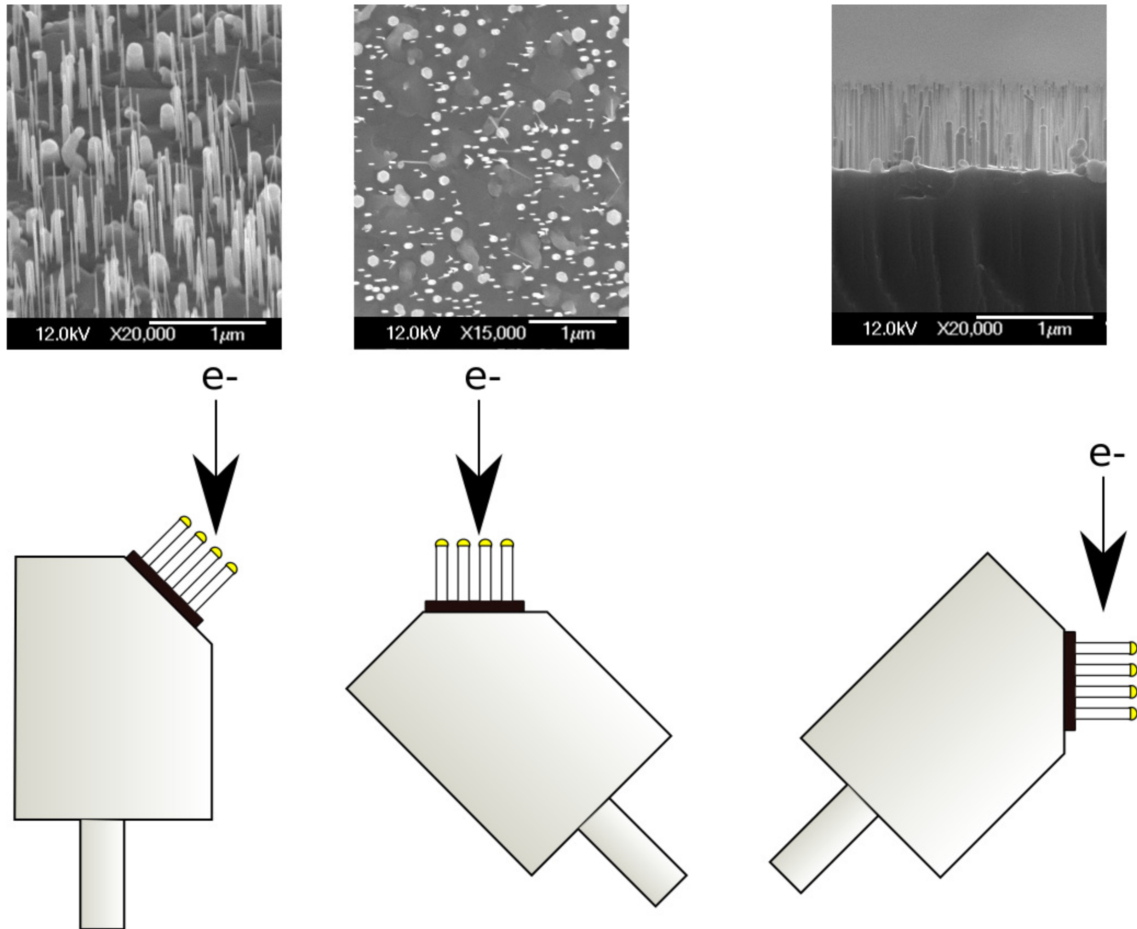

Figure 2.2: Schematic representation of SEM sample mounting geometry for obtaining 0, 45, and 90° images of nanowires.

2.3.2 Transmission Electron Microscopy

Nanowire samples were further investigated using transmission electron microscopy (TEM). The nanowires were removed from the growth substrate by sonication in a methanol solution. The solution was then transferred to a holey carbon grid for examination using a Philips CM12 conventional transmission electron microscope (TEM). The CM12 TEM was used to analyze the general morphology of individual nanowires. A JEOL 2010F high resolution scanning transmission electron microscope (HRTEM) was used for more detailed study. The microscope was used in bright field (BF), selected area diffraction (SAD), and high angle annular dark field imaging (HAADF) modes. The chemical composition was determined by energy dispersive x-ray spectroscopy (EDX).

Before imaging the nanowires, the nanowires were rotated and tilted to the $[2\bar{1}\bar{1}0]$ zone axis condition. This means that the $[2\bar{1}\bar{1}0]$ plane is perpendicular to the incident electron beam. This process increases contrast in the image because there is stronger constructive interference between the wave nature of the electron and the periodic lattice of the nanowire. Furthermore, defects known as stacking faults are only apparent when imaged along the $[2\bar{1}\bar{1}0]$ zone axis [47]. Stacking faults are variations in the stacking sequence of the monolayers, and when imaged along certain zone axes, such as $[2\bar{1}\bar{1}0]$, they appear as dark contrast stripes. When imaged along a different zone axis, such as $[\bar{1}100]$ they don't appear. All images were taken with a 70 μm condenser aperture. Brightfield images were taken with a 50 μm objective aperture using the Gatan Dualview camera. Nanowire overview images were taken at magnifications between 30000 - 60000X which were used to determine overall morphology, length, and diameter. Higher magnification images at 500000 - 1500000X were used to determine crystal structure and evaluate the presence of stacking faults. A Gatan high resolution camera was used to obtain high resolution images of nanowires where

individual stacking planes are clearly resolved. Selected area diffraction (SAD) patterns were obtained by removing the objective aperture and inserting a selected area diffraction aperture in the image plane of the objective lens. SAD patterns at 80 and 200 cm camera lengths using the Gatan Dualview camera were used to verify the type of crystal structure and evaluate the presence of strain relaxation. High angle annular dark field (HAADF) images in scanning transmission electron microscopy mode (STEM) were used to evaluate the location of different elemental compositions (i.e. core-shell or axial heterostructures). In HAADF, an annular camera is used that collects electrons scattered at high angle. This makes HAADF sensitive to atomic composition because different elements have different scattering cross sections and scatter electrons at different angles. Energy dispersive x-ray (EDX) analysis was used to verify the composition of specific segments in the nanowires. In EDX, electrons in the incident TEM beam knock out core level electrons (K, L, shells) in the atoms of the nanowire lattice. Electrons in more loosely bound energy levels transition into these vacancies and emit characteristic x-rays which are detected in the TEM. Compositional maps or linescans across areas of interest in the nanowire were generated and analyzed using INCA software.

2.4 Micro-Photoluminescence Spectroscopy

Micro-photoluminescence (μPL) spectroscopy is a direct, non-destructive way to probe the electronic structure of single nanostructures. To perform this type of measurement, a sample is excited with a continuous wave (CW) laser of chosen wavelength and intensity through a microscope objective. In the μPL configuration, the sample can be imaged, excited, and the luminescence can be extracted simultaneously (see Figure 2.3). The imaging capability allows the location and excitation of single nanowires enabling the correlation of morphological and optical properties. The

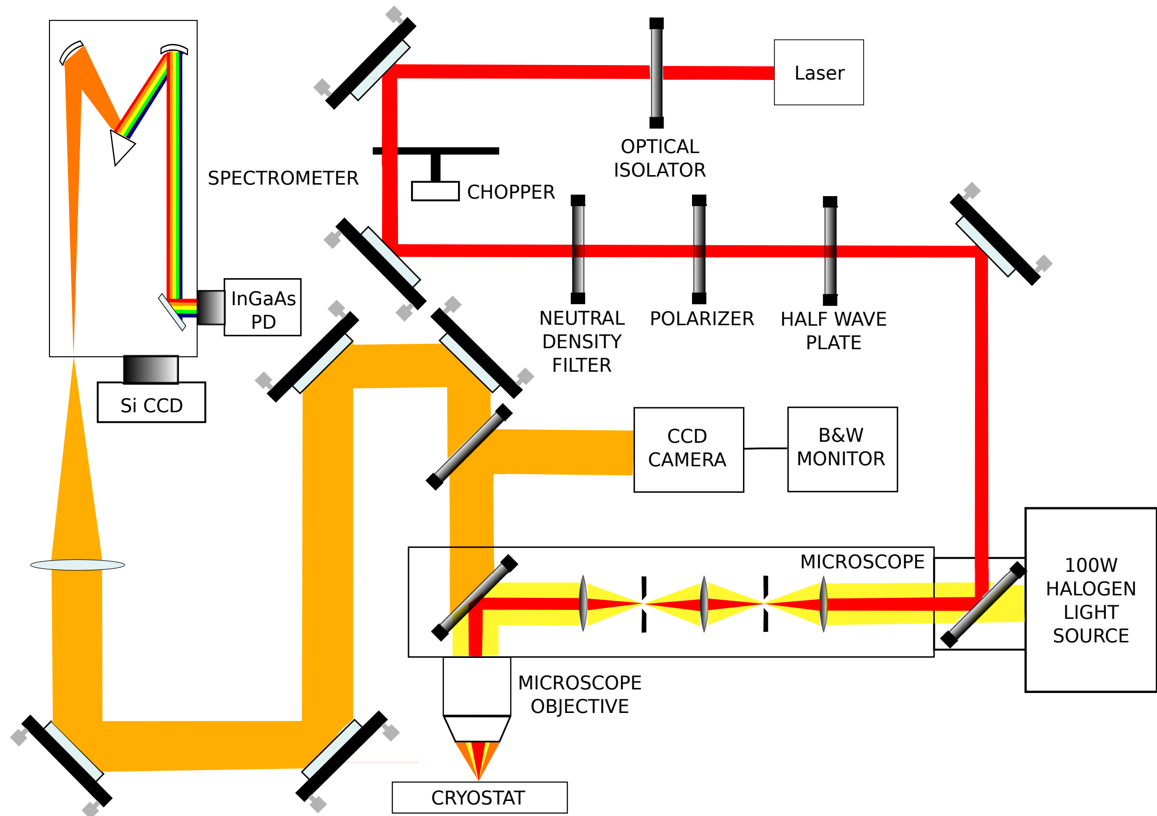

Figure 2.3: Schematic representation of the μPL system.

spontaneous emission of light resulting from the absorption is collected and analyzed spectroscopically. The PL experiment designed and fabricated by the author will be described in this section.

2.4.1 Lasers

The lasers used were a Newport Corp. R-30995 [48] HeNe and a Melles Griot 35LAP431208 [49] tunable Ar-ion laser. The HeNe has an operating wavelength of $\lambda = 632.8$nm and a power of $P = 17$mW. The laser emission is linearly polarized with an extinction ratio of 500:1. The Ar-ion laser has multiple operating wavelengths and is tuned by rotating a Littrow prism. The main operating wavelengths were $\lambda = 488$ and 514.5 nm with powers $P = 130$mW. The emission of this laser is also linearly

polarized with an extinction ratio of 500:1. The laser power was controlled by a set of absorptive neutral density filters with optical densities ranging from 0.1-4. Back reflections were eliminated through the use of an optical isolator.

2.4.2 Optics

The optics were chosen to have the highest performance over the range of operation of 488-1800 nm and the planned extension of the system to 6μm. For the reflective optics, this means that reflectivity should be high and not change appreciably over wavelength. For example, the protected silver mirrors used have a reflectance of greater than 95% over the operating range (see Figure 2.4). This wide range is typical of reflective optics. Accommodating a large range of operation with refractive optics on the other hand is more difficult. For example, the spectrometer entrance optic, which takes the collimated photoluminescence from the sample and focuses it onto the slit plane of the spectrometer has a much shorter operating range (See Figure 2.5). This lens is used for InP and GaAs PL in the 800-900nm range. The objective lens used is an Olympus UIS2 LUCPLFN60X semi-apochromat infinity corrected lens with a corrector ring for cover glass thickness.

In addition to the reflective and refractive optics used, tools for manipulating the polarization were included in the system. A Glan-Thompson linear polarizer with an extinction ratio of 100000:1 coupled with a half wave plate were used to rotate the polarization. This feature is important because absorption [51] and emission [52] of light in nanowires is enhanced when the polarization is oriented along their long axis. All optics were mounted in rigid mounts and affixed to an optical table. Mirrors were mounted in kinematic mounts allowing easy and accurate alignment of the laser and the photoluminescence beams.

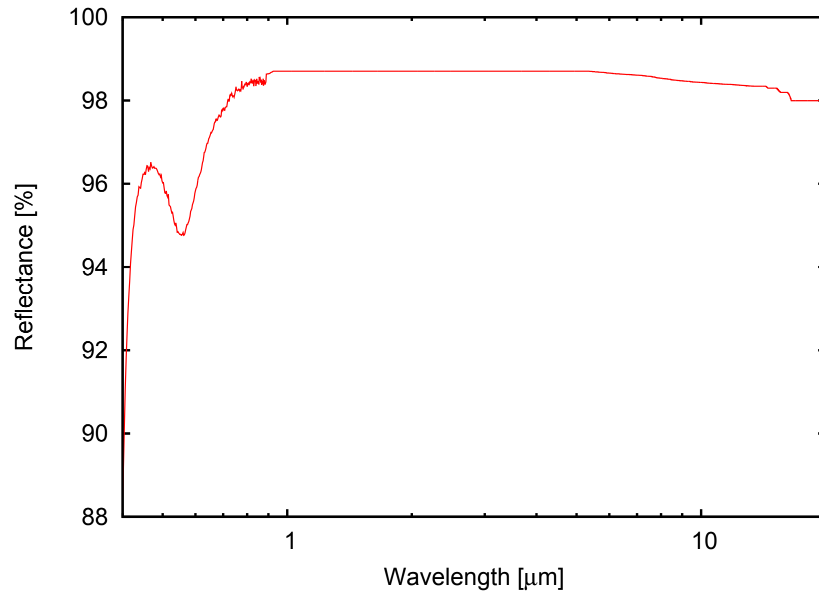

Figure 2.4: Reflectance plot of the Thorlabs PF10-03-P0 protected silver mirror [50].

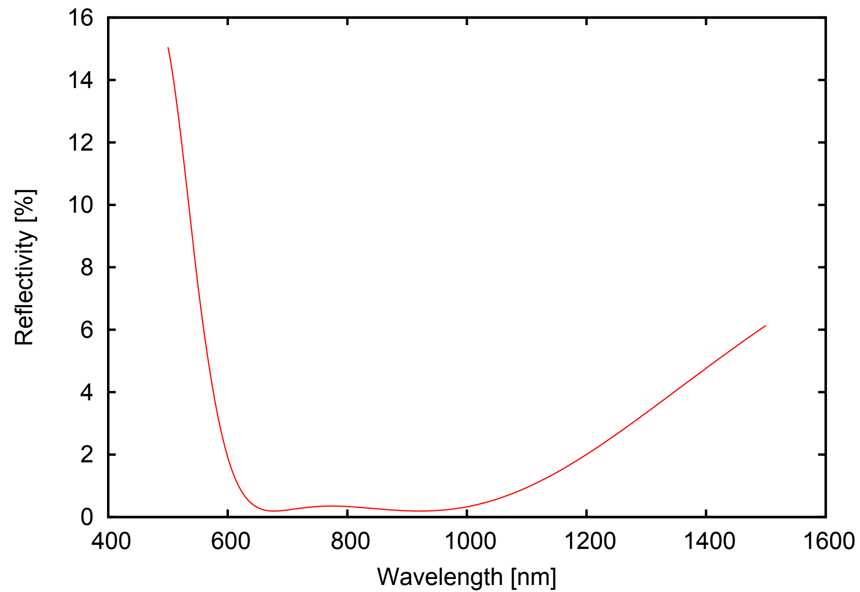

Figure 2.5: Reflectivity vs. wavelength for the Thorlabs B NIR coating [50].

Table 2.1: Specifications of the gratings installed in the spectrometer.

Grating	Groove Density [gr/mm]	Blaze Wavelength [nm]
530 28	1200	750
530 15	600	1000
530 16	600	1500

2.4.3 Spectrometer and Detectors

The spectrometer used is an asymmetric Czerny-Turner (Model iHR550) made by Horiba Jobin Yvon [53]. The fully software controlled spectrometer has motorized entrance and exit slits, automated CCD shutter control, and a motorized three grating turret. The focal length is 0.55 m, the aperture is f/6.4, and the stray light rejection is as much as 10^5. The resolution of the system using an exit slit with a PMT is 0.025 nm. This is increased slightly when using a photodiode or when using a CCD without an exit slit. The gratings selected for the spectrometer were chosen to maximize the wavelength coverage of the system. The gratings used were Horiba 530 28, 510 15, 510 16 models. Grating specifications are provided in Table 2.1

Two types of detectors were installed on the spectrometer's two exit ports: a Si CCD detector and an InGaAs photodiode. Operating wavelength ranges are shown for each detector in Figure 2.6 The Si CCD is a back illuminated, 1024x128 pixel chip with liquid nitrogen cooling made by Horiba Jobin Yvon [53]. The detector was operated at 140K to reduce dark current and has a high quantum efficiency over it's operating range of 350-900nm. The InGaAs photodiode is a liquid nitrogen cooled IGA1.9 model from Electro-Optical systems [54] and was used for infrared studies in the range of 1000-2000nm. This detector was operated using a standard lock-in-amplifier technique. A New Focus 3501 phase locked optical chopper [48] was used to modulate the incident laser and to provide a reference frequency for the Stanford

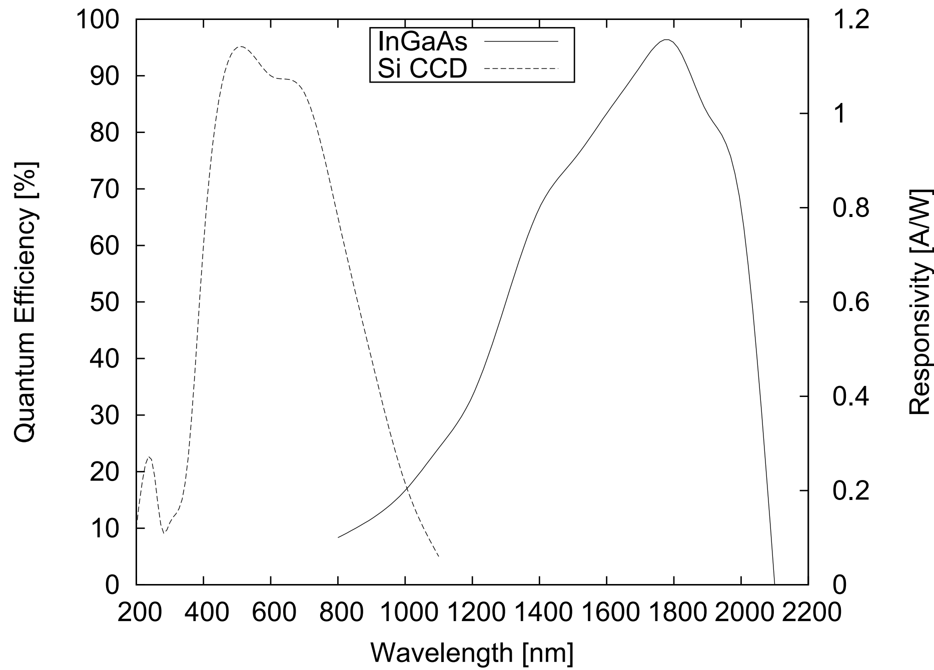

Figure 2.6: Quantum efficiency as a function of wavelength for the CCD detector [53] and responsivity as a function of wavelength for the InGaAs photodiode [54].

Research Systems SR810 lock-in-amplifier [55]. The detector photoresponse was sent to the lock-in-amplifier signal which communicated with the Synergy software via GPIB. The signal was correlated with the spectrometer grating position to provide a photoluminescence intensity in volts as a function of wavelength.

2.4.4 Cryostat

At room temperature, the recombination of electron-hole pairs created by the absorption of laser photons is predominantly non-radiative via the emission of phonons, or quantized lattice vibrations that reduce the observed luminescence. In addition, excitonic features are suppressed because the exciton binding energy is comparable in general to the thermal energy ∼kT. In order to observe more features in the PL spectrum, the sample is cooled to low temperatures using liquid helium. The cryostat

is a Janis ST-500 continuous flow cryostat [56]. To operate the cryostat, the sample space and the helium transfer line vacuum jackets were placed under a vacuum of 1-5$\times10^{-4}$ Torr. The vacuum was provided by a turbo-molecular pump backed by a mechanical pump. These spaces are placed under vacuum to eliminate any conductive and convective heat transfer between the surroundings and the helium flowing in the transfer lines. Radiative heat transfer was limited by a radiation shield that surrounded the sample stage. Once the cryostat was placed under vacuum, one end of a transfer line with a needle valve was placed in a helium dewar and the other end was inserted in the transfer leg of the cryostat. Pressure was built up slowly in the dewar which caused the transfer line to cool, and eventually cause the flow of helium into the cryostat. The helium flows through tubing that encircles the sample stage, cools it, and is subsequently recovered for reuse. The sample temperature was measured using a Lakeshore 331 temperature controller [57] with a calibrated Si diode. The diode was mounted on the side of the sample stage providing an accurate measurement of temperature at the sample surface.

2.5 I-V Characterization

Nanowires were fabricated into field effect transistor geometries to characterize their mobility. 175nm of SiO_2 was deposited thermally at 1000°C under wet O_2 conditions on n^{++} Si substrates. Nanowires were removed from the growth substrate by sonication in a methanol solution. The nanowires were dispersed onto the Si/SiO_2 wafers. Individual nanowires with diameters between 40 - 80nm were then located using SEM.

Electron beam lithography was used to form contacts to the ends of the nanowire. To begin this process, an electron sensitive resist consisting of polymethyl-methacrylate

(PMMA) dissolved in the solvent anisole was applied to the wafer. The wafer was placed on a spinner, a device consisting of a vacuum chuck capable of rotational speeds of up to 5000 RPM. Depending on the size of the substrate, three to four small drops are pipetted onto the sample starting in the centre and moving out towards the edge. Once the e-beam resist covered the entire sample, the spinner was ramped up to the manufacturers recommended speed [58]. For a given thickness, the speed depends on the dilution of the resist in the solvent. The e-beam resist was soft baked on a hotplate at 150° for 60 to 90 seconds. Here the remaining solvent that hasn't evaporated during the spinning process is removed. The heat strengthens the bonds between the resist and the substrate improving the adhesion of the resist to the substrate and removes stress built in from the spinning process [20]. The wafer is then placed on a sample stage and transferred to the electron beam lithography tool. Here the electron beam is rastered over the surface of the sample in locations defined by a pattern created by computer assisted drafting (CAD) software. For nanowire source-drain contacts, the beam was scanned over the ends of the wires exposing the resist in these areas. The exposed resist is developed in methyl-isobutyl-ketone (MIBK) dissolved in iso-propyl alcohol. The resist is then hard baked on a hot plate at 100°C for 60 to 90 seconds. This step removes the residual developer and any moisture left in the resist image. For InAs-AlInAs core-shell devices, the exposed ends of the nanowire are subjected to citric acid etching to remove the shell [59] and a sulfur passivation procedure to remove, and prevent new oxides from forming on the InAs surface to ensure Ohmic contacts [38, 60]. Electron beam evaporation is used to deposit a Ni/Au (30/50 nm) film. The wafer, fully coated in metal is placed in acetone to dissolve the resist. The metal resting on top of the unexposed resist is carried away in the solution and only the contact areas remain. The contacts were then annealed in vacuum at 120°C for 5 minutes.

The chip was wirebonded to a chip carrier and I-V measurements were carried out in He vapour in a Oxford continuous flow cryostat operating from 4K to room temperature or a dilution refrigerator allowed to warm to 1.2K. Global back gate voltage and the source-drain bias was provided by a home built voltage source. Upon applying a source-drain voltage, DC current was measured using a DL current preamplifier with a noise floor of ~ 0.5 pA/$\sqrt{\text{Hz}}$.

Chapter 3

Growth of InP and InAs Nanowires

3.1 Introduction

To date, most nanowires have been grown using the vapour-liquid-solid (VLS) method where a Au seed particle acts as a collector for the growth species impinging directly on the Au particle, on the nanowire sidewalls or on the substrate surface [61]. Nanowires have been grown by the VLS method using metalorganic vapour phase epitaxy (MOVPE), chemical beam epitaxy (CBE) or molecular beam epitaxy (MBE), among other methods. By changing the species during growth, axial or radial (core-shell) nanowire heterostructures can be fabricated. Nanowires offer the capability of fabricating highly lattice mismatched heterostructures, due to the effective strain relaxation at the nanowire sidewalls. It is usually assumed from the bulk phase diagrams that group V species (e.g., As, P) have low solubility in Au, while group III species (e.g., In, Ga) can have high concentrations in the Au [62]. Hence, group V species are easily depleted from the Au particle during the gas phase switching and abrupt interfaces are easier to achieve in heterostructures where the group III concentration remains constant while the group V species change. The latter pragmatic issue makes InAs/InP and GaAs/GaP nanowires among the most commonly studied material systems. In addition, the latter nanowire heterostructures are two of the few systems where kinking can be avoided and straight nanowires can be grown due to the kinetics and thermodynamics of growth [63]. While there have been many studies

Table 3.1: InP/InAs nanowire growth conditions.

Sample	Structure	Temperature [°C]	V/III Flux Ratio[a]	Growth Rate[a] [nm s^{-1}]
A	InP/InAs/InP	370	2.8(5.6)	0.28 (0.14)
B	InP/InAs/InP	400	2.8(5.6)	0.28 (0.14)
C	InP/InAs/InP	440	2.8(5.6)	0.28 (0.14)
D	InP/InAs/InP	400	1.8(3.6)	0.28 (0.14)
E	InP/InAs/InP	400	3.7(7.4)	0.28 (0.14)
F	Multiple InAs segments	400	1.8(3.6)	0.28 (0.14)

[a]Quantities in brackets indicate growth conditions for the InAs segment and surrounding InP barrier segments, while quantities outside brackets refer to the base InP segment

on the growth of InP and InAs nanowires by MOVPE or CBE [64–71], there are only a few studies on such nanowires grown by MBE [72–74]. In this section we present a systematic study of InP nanowire growth, as well as the growth of short segments of InAs within InP nanowires. It was determined that the V/III flux ratio increased the growth rate suggesting that the growth is Group V limited. Secondly, it was observed that there was a very narrow temperature window in which InP nanowires were able to be grown. Finally, a new growth mechanism was characterized in which short segments of InAs were formed by depletion of In from the Au particle rather than adatom diffusion from the nanowire sidewalls or substrate. This purging mechanism was reported by us in the journal Nanotechnology [34].

3.2 Experimental Details

S-doped InP (111)B (1 - 4 × 10 ^{18} cm^{-3}) wafers were treated by UV-ozone oxidation for 20 min to remove any hydrocarbon contamination and to grow a sacrificial oxide. The wafers were then dipped in buffered HF for 30 s and rinsed under flowing deionized water for 10 min. The wafers were dried with N_2 and transferred to an electron beam evaporator where a 1 nm thick Au film was deposited at a rate of 0.1

nm s^{-1} as measured by a quartz crystal thickness monitor. The wafers were then transferred to a gas source molecular beam epitaxy (GSMBE) system (SVT Associates). In GSMBE, group III species are supplied as monomers from an effusion cell, and group V species are supplied as P_2 and As_2 dimers that are cracked from PH_3 and AsH_3 in a gas cracker operating at 950°C. Prior to growth, the wafers were placed in a pre-deposition chamber where they were degassed for 15 min at 250°C. After transferring the wafers to the growth chamber, an oxide desorption step was performed where they were heated to 485°C under inductively coupled hydrogen plasma and P_2 overpressure for 10 min, leading to the formation of Au nanoparticles. Nanowires were grown with InP/InAs/InP heterostructures. The sample was cooled to the growth temperature (see Table 3.1) and nanowire growth was initiated by opening the In shutter. In the first series of growths (Samples A, B and C in Table 3.1) the growth temperature was varied (370, 400 and 440°C) leaving the V/III flux ratio constant (2.8). In the second series of growths (Samples D, B, E in Table 3.1), the V/III flux ratio was varied (1.8, 2.8 and 3.7) under constant growth temperature (400°C). The first InP segment was grown for 15 min at a 2D equivalent growth rate of 0.28 nm s^{-1} (1 μm h^{-1}). Following this initial InP segment growth, the growth rate was reduced to 0.14 nm s^{-1} (0.5 μm h^{-1}) for the remainder of the growth where the V/III flux ratio was twice that of the initial InP segment growth. An additional 2 min of InP was grown, followed by an InAs segment. The InAs segment was grown by terminating the In supply, exchanging P_2 with As_2 over a period of nominally 25 s, and then reopening the In shutter for 7.5 s. After growing the InAs segment, the previous operation was reversed; i.e., the In shutter was closed, As_2 was replaced by P_2 over 25 s, and a final InP segment was grown by reopening the In shutter for 2 min. The growth was terminated by cooling the sample under a P_2 overpressure.

Another sample (Sample F in Table 3.1) comprised of multiple InAs segments was grown. This sample will be described further in Section 3.3.

The nanowire morphology and density were determined using a JEOL 7000F field emission scanning electron microscope (SEM). The nanowires were removed from the growth substrate for structural investigation by sonication in a methanol solution. The solution was then transferred to a holey carbon grid for examination using a Philips CM12 conventional transmission electron microscope (TEM) and a JEOL 2010F high resolution scanning transmission electron microscope (HRTEM) in bright field (BF) and high angle annular dark field imaging (HAADF) modes, respectively. The chemical composition was determined by energy dispersive x-ray spectroscopy (EDX) in the JEOL 2010F.

3.3 Results and Discussion

The effect of the growth temperature was investigated by examining nanowires grown at 370, 400 and 440°C with a V/III flux ratio of 2.8 (Samples A, B and C, respectively, in Table 3.1). The SEM analysis shown in Figure 3.1 indicates that the majority of nanowires in all samples grew orthogonally to the substrate surface, i.e., along the (111)B direction, which is generally the preferred growth direction for nanowires [75]. However, some of the nanowires grown at 370°C (Figure 3.1(a)) exhibited deleterious kinking or a growth direction different from the (111)B substrate surface normal. This aspect and the general nanowire morphology will be discussed in more detail later in the TEM analysis. The typical diameter, height and density of the nanowires at the growth temperature of 400°C (Sample B, Figures 3.1(b) and (e)) were 50 nm, 1.1 μm and 5×10^{9} cm^{-2} , respectively. The nanowire density was reduced significantly at the lower (370°C) or higher (440°C) growth temperature as

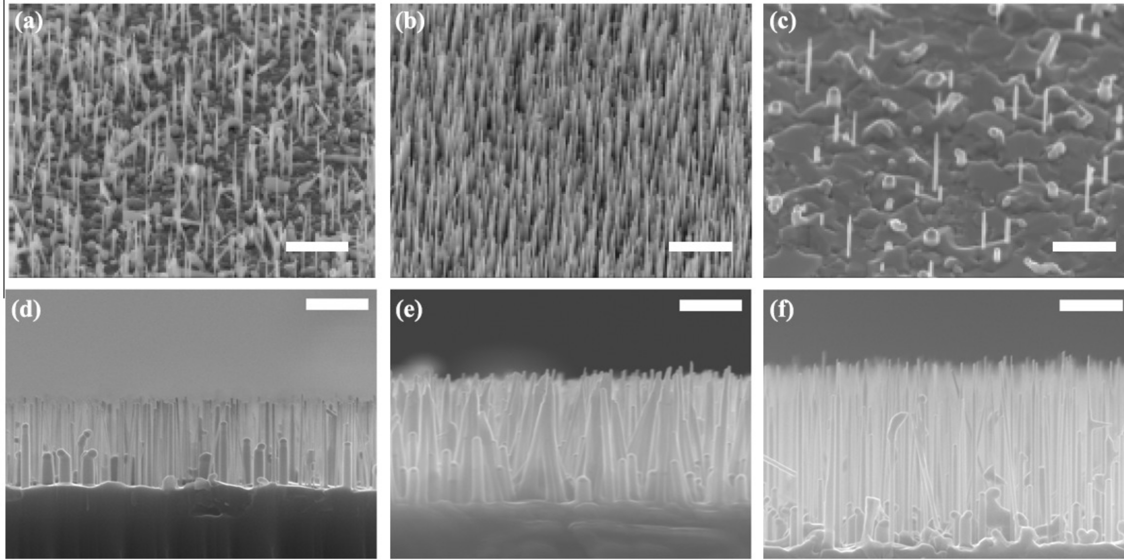

Figure 3.1: 45° tilted (a)-(c) and cross-sectional (d)-(f) SEM images of: (a) Sample A (T = 370°C, V/III = 2.8); (b) Sample B (T = 400°C, V/III = 2.8); (c) Sample C (T = 440°C, V/III = 2.8); (d) Sample D (T = 400°C, V/III = 1.8); (e) Sample B (T = 400°C, V/III = 2.8); and (f) Sample E (T = 400°C, V/III = 3.7). Scale bars are 1 μm in (a)-(c) and 500 nm in (d)-(f).

seen in Figures 3.1(a) and (c), respectively. The latter observation can be explained by examining the nanowire growth process. Nanowires grow by feeding the Au seed particle at the top of the nanowire by the diffusion of adatoms from the substrate surface or the nanowire sidewalls. Presumably, the adatom diffusivity is reduced at the lowest growth temperature such that the film growth between the nanowires is enhanced at the expense of nanowire growth. Similarly, the low nanowire density and rough surface in Sample C at high growth temperatures (440°C) may indicate a change in chemical potential between the film, nanowire, and seed particle or a Au particle phase transition [72] that favours film rather than nanowire growth. Hence, a narrow temperature window around 400°C was observed, similar to that reported previously for InAs nanowires grown by solid source MBE [72].

The influence of the V/III flux ratio was examined in Samples D, B and E which were grown at the optimum temperature of 400°C and with a V/III flux ratio of 1.8,

2.8 and 3.7, respectively. The SEM images in Figures 3.1(d)-(f) showed an increase in the average NW height with increasing V/III flux ratio. The nanowire heights, measured directly from the SEM images and plotted in the histogram of Figure 3.2, showed typical values of 0.75, 1.1 and 1.6 μm with the V/III flux ratios of 1.8, 2.8 and 3.7, respectively. Hence, the nanowire height increased in direct proportion to the V/III flux ratio. A similar dependence of the growth rate on the V/III flux ratio was previously observed in Au-assisted MBE-grown GaAs nanowires [76], Ga-assisted MBE-grown GaAs nanowires [77] and GaN nanowires [78] where it was speculated that the growth may be limited by group V species; i.e., due to the large concentration of group III species in the Au particle, an effective V/III ratio <1 may prevail at the Au/nanowire interface.

Next, the morphology and structure of the nanowires was examined by TEM as shown in Figure 3.3. TEM confirmed that all nanowires were capped with a Au seed particle consistent with the VLS mechanism. Nanowires from Sample A, that were grown at the lowest temperature of 370°C, frequently exhibited kinks or an irregular morphology as shown in Figure 3.3(a). The kinking did not coincide with the InAs/InP heterostructure. Similar kinking has been reported in MOVPE-grown InP [71] and GaAs nanowires [79] where it was speculated that the enhanced radial growth of the nanowire at low temperatures causes group III depletion and solidification of the Au particle.

At the higher growth temperature of 400°C, Sample B exhibited straight nanowires that were either rod-shaped or pencil-shaped, in roughly equal proportions. The pencil-shaped morphology, illustrated in Figure 3.3(b), is frequently observed in nanowires grown by MBE [76]. This morphology is due to vapour-solid deposition on the nanowire sidewalls resulting in radial growth in addition to the Au seeded axial growth. The Sample C nanowires, which were grown at the highest temperature,

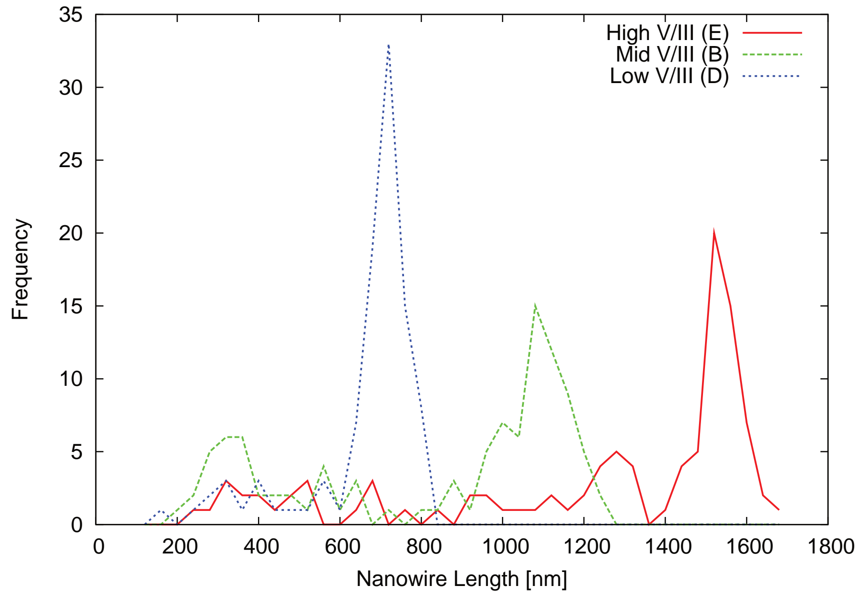

Figure 3.2: Histogram of nanowire lengths for samples grown at 400 °C and a V/III flux ratio of 1.8 (Sample D), 2.8 (Sample B) and 3.7 (Sample E).

showed predominantly a rod-shaped morphology with very little tapering as shown in Figure 3.3(c). This morphology is presumably due to enhanced adatom diffusivity from the nanowire sidewalls and/or substrate surface to the Au particle at the higher growth temperature. As a result, adatoms have a diffusion length greater than the nanowire length such that axial growth is preferred as compared to radial growth. Hence, the proportion of rod-shaped nanowires increased with growth temperature. Conversely, TEM analysis of nanowires from Samples D and E (not shown) indicated that the proportion of pencil-shaped nanowires increased with V/III flux ratio presumably because the In adatom diffusivity was reduced due to reactivity with the increasing group V flux, similar to that observed for GaAs nanowires [76].

Contrast stripes were visible in all of the TEM images of the nanowires as illustrated in Figure 3.3. These stripes are due to the presence of stacking faults, commonly observed in nanowires, where the crystal structure alternates between wurtzite and zincblende [76]. The average density of stacking faults was roughly

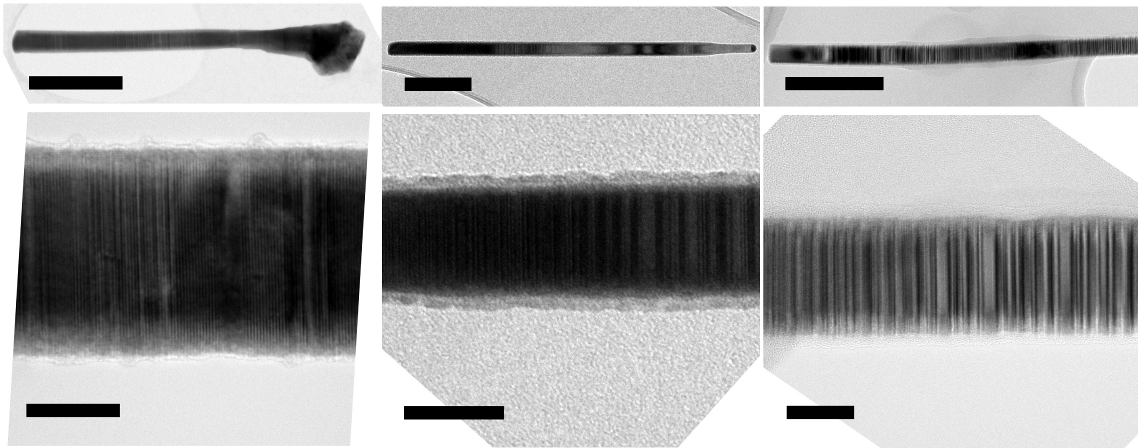

Figure 3.3: Bright field TEM images of a nanowire from (a) Sample A, T = 370°C, V/III = 2.8, (b) Sample B,T = 400°C, V/III = 2.8, and (c) Sample C, T = 440°C, V/III = 2.8. The upper image shows the entire nanowire while the lower image shows a magnified view of the stacking faults. Scale bars are 200 nm in the upper images and 20 nm in the lower images

0.3 nm^{-1} , without any clear trend with temperature, V/III flux ratio, or nanowire diameter. However, the top third of the nanowire was typically fault-free with the wurtzite structure. In our previous study of GaAs nanowires [76], we found that the growth rate of the nanowires had a major impact on the stacking fault density. GaAs nanowires grown at a 2D equivalent growth rate of 0.5 μm h^{-1} exhibited a wurtzite structure with a much lower fault density compared to those grown at 1 μm h^{-1} . Similarly, in the present study, the InAs segments and the surrounding InP segments were grown at 0.5 μm h^{-1}, coincident with the fault-free region typically found near the top of the nanowires.

The top of the nanowires including the InAs segment was examined by HAADF TEM as illustrated in Figure 3.4 for a representative nanowire from Sample C (similar results were obtained from the other samples). The bright contrast near the middle of the nanowire indicates the location of the InAs segment as verified by the superimposed EDX linescans, while the bright contrast at the end of the nanowire indicates the Au seed particle. The InAs segment was located near the top of the

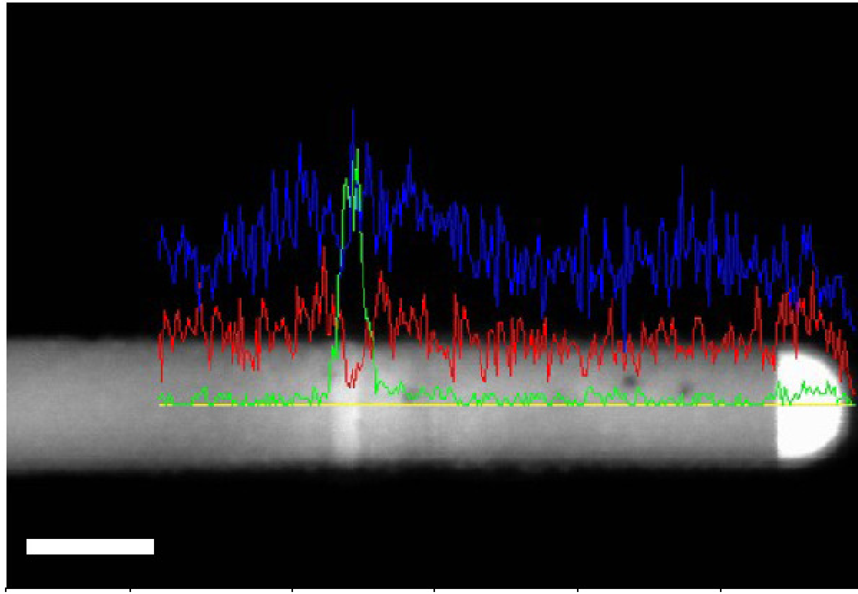

Figure 3.4: HAADF image and superimposed EDX linescan along the nanowire axis showing the As (green, lower line), P (red, middle line) and In (blue, upper line) contents. The scale bar is 30 nm.

nanowires where little radial growth occurred; therefore, the diameters of the InAs and terminating InP segments were equal to the Au particle diameter.

Using the InAs segment as a marker layer, the length of the final InP segment that was grown for a duration of 2 min was measured directly from the TEM images. The InP segment length is plotted in Figure 3.5 as a function of the Au seed particle diameter (equal to the nanowire diameter) for Samples D (squares) and E (diamonds) grown with the lowest (1.8) and highest (3.7) V/III flux ratios, respectively, at the optimum temperature of 400 °C. The trend in nanowire length with V/III flux ratio observed previously in Figure 3.2 is not as obvious in Figure 3.5 due to the relatively short segment lengths as compared to the dispersion in nanowire growth rates.

The most obvious and important observation was the decline in segment length with diameter which is usually taken as a signature of adatom diffusion from the substrate or nanowire sidewalls [15,80]. A previous study of InAs nanowires grown by MBE indicated that the dominant diffusion mechanism is from the nanowire sidewalls

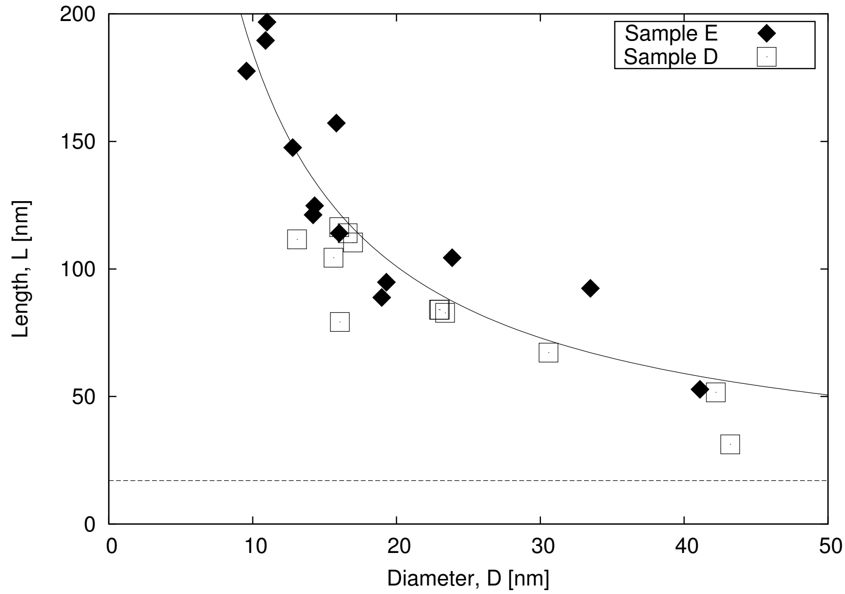

Figure 3.5: Plot showing the length of the terminating InP segment. The solid line is a fit to the data using Equation (3.2). The dotted line shows the equivalent 2D deposition.

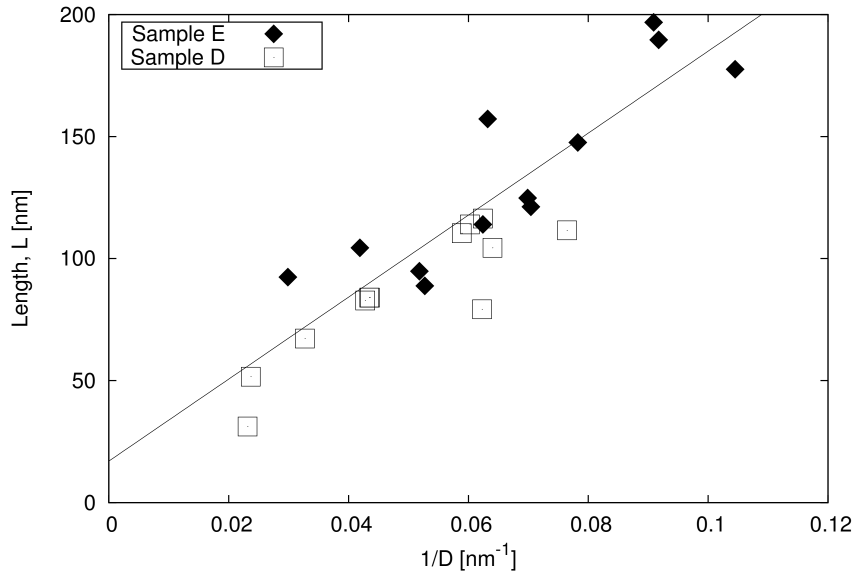

Figure 3.6: Plot showing the length of the terminating InP segment plotted as a function of inverse diameter.

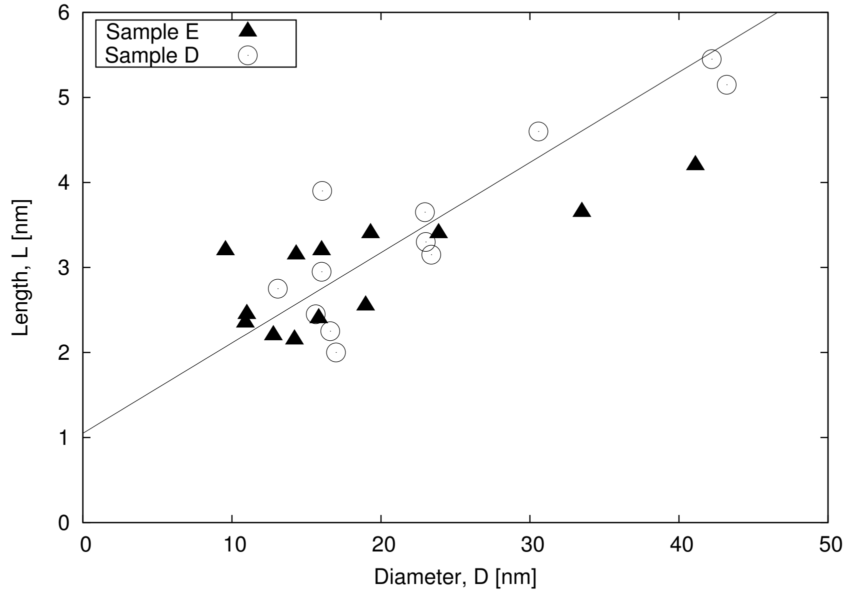

Figure 3.7: Plot showing the length of the InAs segment versus diameter. The solid line is a fit to the data using Equation (3.6).

as opposed to the substrate surface [74]. The nanowire growth rate may then be simply expressed as:

$$\frac{\pi D^2}{4}\frac{dL}{dt} = \gamma \pi D \tag{3.1}$$

where D is the catalyst (or nanowire) diameter, L is the nanowire length, and γ is a constant primarily dependent on the adatom impingement rate and diffusion to the Au seed particle. The expression on the left in Equation (3.1) is the volume rate of change of the nanowire, while the right-hand side expresses the adatom collection from the nanowire sidewalls (proportional to the sidewall area). Integration of Equation (3.1) gives:

$$L = L_0 + \frac{4\gamma t}{D} \tag{3.2}$$

where L_0 is the nanowire height due to direct impingement on the Au particle (equal to the nominal 2D equivalent thickness). Accordingly, one would expect a nanowire length, L, which varies inversely with D (Equation (3.2)). The InP segment length, L, is plotted versus diameter, D, in Figure 3.5 for Samples D (squares) and E (diamonds). Also, the same data are plotted as L versus $1/D$ in Figure 3.6 where the solid line is a least squares fit to the data indicating the D^{-1} dependence of the InP segment length in accordance with Equation (3.2). Alternatively, a plot (not shown) of $\log(L - L_0)$ versus $\log(D)$ clearly indicated a slope of -1 consistent with the $1/D$ dependence of the nanowire length in Equation (3.2). As expected, as the nanowire diameter increased (or $1/D$ decreased), the segment length approached the nominal 2D equivalent thickness of $L_0 = 17$ nm (= 0.14 nm $s^{-1} \times$ 120 s) indicated as the dashed line in Figure 3.5 or by the intercept of the solid line in Figure 3.6. The slope of the solid line Figure 3.6 indicated a value of $\gamma = 3.5$ nm^2 s^{-1} , using Equation (3.2). The solid line in Figures 3.5 and 3.6 therefore indicate the fit to the data using Equation (3.2) with $L_0 = 17$ nm and $\gamma = 3.5$ nm^2 s^{-1} . A similar $1/D$ dependence of the nanowire height was previously observed in MBE-grown GaAs nanowires [81].

Like in the previous analysis, the InAs segment length was plotted versus the Au particle diameter for Samples D (circles) and E (triangles) in Figure 3.7. Unlike the InP segment considered earlier, the InAs segment length plotted in Figure 3.7 showed a dependence on the diameter that was clearly linear, indicative of a different growth mechanism. The InAs segment was grown with an In impingement duration of 7.5 s, contributing a length of $L_0 = 1.05$ nm (= 0.14 nm $s^{-1} \times$ 7.5 s) due to direct impingement on the Au particle. The solid line in Figure 3.7 shows the least squares fit to the data with an intercept of 1.05 nm.

To explain the linear D dependence of the InAs segment length, another contribution to the nanowire growth must be considered. In addition to the contribution from

direct impingement, there is also a contribution to the InAs growth due to purging or depletion of In from the Au droplet during the gas switching sequence. Growth of the InAs segment was initiated by terminating the In supply (to cease growth of the preceding InP segment), exchanging P_2 with As_2 over a period of 25 s, and then reopening the In shutter for 7.5 s. The Au droplet is expected to act as a reservoir for In. Hence, In may react with As_2 (or residual P_2) to form InAs (InAsP) during the gas switching sequence. Assuming a hemispherical droplet, the number of In atoms depleted from the droplet may be expressed as:

$$N_{droplet} = \frac{1}{12}\pi D^3 \Delta X_{In} \left[X^0_{In}\rho_{In} + \left(1 - X^0_{In}\right)\rho_{Au}\right] \tag{3.3}$$

where D is the Au droplet diameter (equal to the nanowire diameter), ΔX_{In} is the fractional change in atomic concentration of In atoms in the droplet due to depletion, ρ_{In} is the density of In, and ρ_{Au} is the density of Au. The term in brackets is the weighted density of the Au-In droplet using the initial atomic fraction of indium in the droplet, X_{In}. We estimated $X_{In} = 0.6$ based on cool down experiments described below. The number of In atoms in the resulting InAs segment is:

$$N_{InAs} = \frac{1}{4}\pi D^2 L \rho_{In-InAs} \tag{3.4}$$

where L is the InAs segment length and $\rho_{In-InAs}$ is the density of In in InAs. Equating Eqs. (3.3) and (3.4) and using $\rho_{In} = 7.31$ g cm^{-3} , $\rho_{Au} = 19.3$ g cm^{-3} and $\rho_{In-InAs} =$ 3.43 g cm^{-3} gives:

$$L = 1.18\Delta X_{In} D \tag{3.5}$$

Adding the contribution due to direct impingement yields:

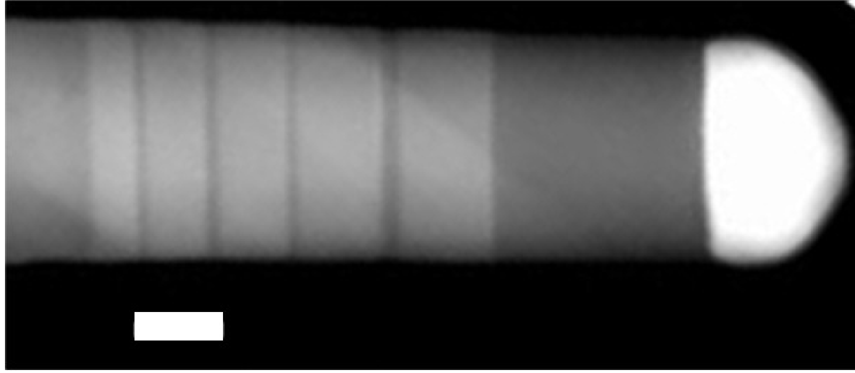

Figure 3.8: HAADF image of Sample F. The scale bar is 20 nm.

$$L = L_0 + 1.18\Delta X_{In} D \tag{3.6}$$

Accordingly, the InAs segment length L is proportional to the diameter D , and the data of Figure 3.7 can be explained by Equation (3.6) using $\Delta X_{In} \sim 9\%$ and $L_0 =$ 1.05 nm (the solid line in Figure 3.7). In the case of the InP segment, the nanowire growth followed Equation (3.2) with a $1/D$ dependence of the length since the In impingement duration (120 s) was significantly longer than the gas switching time (25 s) at the InAs/InP interface. On the other hand, the InAs segment is expected to follow Equation (3.6) with a linear D dependence of the length because the gas switching time (25 s) at the InP/InAs interface was appreciable compared to the In impingement duration (7.5 s).

To further demonstrate the growth behaviour of short InAs segments, a nanowire sample was grown (Sample F in Table 3.1, also shown in Figure 3.8) with multiple InAs segment lengths, each of different In impingement duration. The sample was grown using a gas switching sequence similar to that described earlier but with increasing In impingement duration in each consecutive InAs segment (0, 5, 7.5, 12.5 and 17.5 s). The first InAs segment (labelled 0 s) was grown by implementing the gas switching sequence to change from P_2 to As_2 , then switching in reverse from As_2 to P_2 without

opening the In shutter. Hence, the first segment is expected to grow only from In depletion of the Au droplet and not from direct impingement of In from the effusion cell. The InP barriers between the InAs segments were fixed at 20 s duration.

The growth sequence and representative HAADF TEM image of a nanowire from Sample F are shown in Figure 3.8. A significant observation is the presence of the 0 s InAs segment, which provides direct evidence of In depletion from the Au droplet (the In shutter was closed during this first segment). The InAs segment lengths were measured directly from TEM images, and plotted versus the Au particle (or nanowire) diameter in Figure 3.9, similar to what was done previously in Figure 3.5. The total InAs segment length may be expressed as the sum of the direct impingement on the Au droplet (2D equivalent thickness, L_0) and diffusive flux (Equation (3.2)) as well as the Au droplet depletion (Equation (3.5)):

$$L = L_0 + \frac{4\gamma t}{D} + 1.18\Delta X_{In} D \tag{3.7}$$

The solid lines in Figure 3.9 correspond to the best fit using Equation (3.7) with $\gamma = 4$ nm^2 s^{-1} and $X_{In} = 14\%$, similar to the values used in the earlier analysis. A transition from droplet depletion to diffusive behaviour can be observed as In impingement duration increased. The very large nanowire lengths predicted by the model for small diameters (< 20 nm) are probably not realized in practice as the Gibbs-Thomson effect will limit the growth rate for such small diameters [69].

To conclude our studies, we performed two different cool down experiments to directly measure the change in In concentration, ΔX_{In}, due to depletion of the Au seed particle. In the first experiment, InP nanowires were grown and cooled without any incident In or P_2 flux. In this instance, the In concentration in the Au particle was measured by means of EDX to be in the range of 55-60 at.% for nanowire diameters in

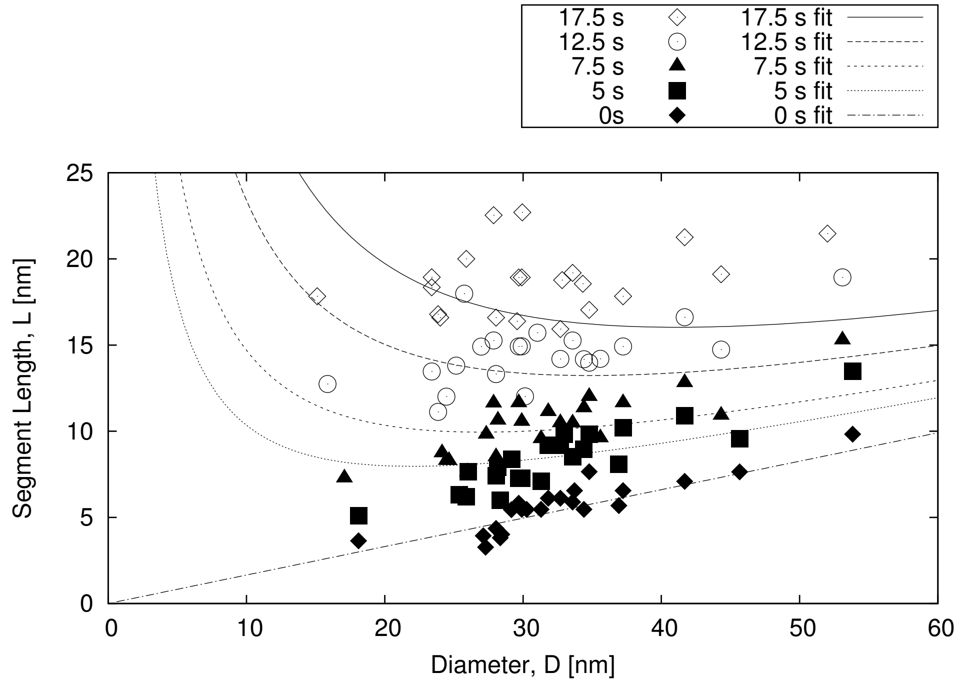

Figure 3.9: InAs segment length versus diameter for Sample F for In impingement durations of 0 s, 5 s, 7.5 s, 12.5 s, and 17.5 s. Lines are corresponding fits to the data using Equation (3.7).

the range of 40-60 nm. In the second experiment, identical InP nanowires were grown and terminated by closing the In shutter; this was followed by a gas switching sequence in which the P_2 flux was terminated and an As_2 flux was initiated as described earlier. Subsequently, the nanowire sample was cooled without any flux. In this case, the In concentration in the Au particle was measured to be 45-50 at.% and an InAs segment was observed by TEM (not shown) at the end of the nanowire. Hence, a change in In concentration of $\Delta X_{In} \sim$ 5-15% was observed between the two experiments similar to that inferred in the earlier samples, and this was consistent with the creation of a terminating InAs segment due to droplet depletion.

As mentioned in Section 3.1, the solubility of the group III material (e.g., In, Ga, Al) in the Au particle can influence the abruptness of heterostructure interfaces due to purging from the Au particle. For example, the storage of Al in the Au particle

can produce a graded interface in GaAs/AlGaAs nanowires [82]. On the other hand, abrupt interfaces are sometimes found in special circumstances, as in the growth of InGaAs/InAs nanowires where the solubility of one element (e.g., In) may influence the solubility of another (e.g., Ga) [83]. In the present study, we demonstrated a further limitation in the control of short nanowire segment lengths due to instability in the solubility of group III material in the Au particle during a gas phase switching procedure for growth of InAs/InP heterostructures. Similar limitations may be expected in other nanowire systems (e.g., GaAs/GaP). These results provide new knowledge required to control the length of short nanowire segments grown by MBE and possibly other growth techniques.

3.4 Conclusions

InAs/InP nanowires were grown by gas source molecular beam epitaxy using the Au-assisted VLS mechanism. A narrow operating temperature window near 400°C was found to optimize the nanowire density. A linear increase in InP nanowire length with V/III flux ratio suggested a group V limited mechanism. Low growth rates minimized the presence of stacking faults in the InAs segment and the surrounding InP barriers. Short InAs segments were found to grow predominantly by depletion of In from the Au droplet during the gas switching sequence at the InP/InAs interface with a transition to growth driven by adatom diffusion for sufficiently long segments.

Chapter 4

InAs/AlInAs(P) Core-Shell Nanowires

4.1 Introduction

In this chapter, experiments and theoretical calculations will be presented regarding InAs/$Al_xIn_{1-x}As(P)$ core-shell nanowires. The experimental work was published in the Journal of Crystal Growth [35]. Passivation of the InAs nanowires using InP shells proved difficult via GSMBE due to the tendency for the formation of axial rather than core-shell structures. To circumvent this issue, $Al_xIn_{1-x}As$ or $Al_xIn_{1-x}P$ shells with nominal Al composition fraction of x = 0.20, 0.36, or 0.53 were grown by direct vapour-solid deposition on the sidewalls of the InAs nanowires. Characterization by transmission electron microscopy revealed that the addition of Al in the shell resulted in a remarkable transition from the VLS to the vapour-solid growth mode with uniform shell thickness along the nanowire length. Possible mechanisms for this transition include reduced adatom diffusion, a phase change of the Au seed particle and surfactant effects. The InAs-AlInP core-shell nanowires exhibited misfit dislocations, while the InAs-AlInAs nanowires with lower strain appeared to be free of defects. A theoretical study of the critical thickness of Al_xIn_{1-x} of $Al_xIn_{1-x}P$ shells on InAs cores was accepted for publication in the Journal of Applied Physics and currently is hosted on arXiv [36].

InAs nanowires are of interest for the continued down-scaling of MOSFET devices due to the high electron mobility of InAs and the possible integration with Si. The

small bandgap of InAs makes this material of interest in infrared photodetectors [24], and the large spin-orbit coupling makes InAs a viable candidate for quantum computing devices [22] and novel probes of exotic condensed matter phenomena [31]. In all of these applications, optimal device performance depends on the removal of surface states. The elimination of surface states reduces unwanted ionized impurity scattering, scattering from rough oxidized surfaces, electron-hole recombination, and carrier depletion due to surface traps. There are two methods generally used to passivate nanowire surfaces: chemical and structural. Chemical passivation of III-V nanowires is typically accomplished with ammonium polysulfide $(NH_4)_2S_x$ [38,60] or organic sulfide octadecylthiol (ODT) [84]. The effectiveness of chemical passivation declines with time so while chemical passivation is a good method to improve ohmic contact formation, it is not the best choice for long term passivation of the entire nanowire surface. The alternative to chemical passivation is structural passivation where a material with a higher band gap is grown around the nanowire core. Improved performance of InAs-InP core-shell nanowire field effect transistors (NWFET) has been shown over unpassivated InAs NWFETs [85]. One disadvantage of structural passivation is that the shell must be etched selectively to form contacts to the core. Fortunately, selective etching is a common practice in III-V device processing so etching the shell is generally possible [86].

Core-shell InAs-InP nanowire heterostructures have demonstrated improved performance in MOSFET devices compared to their unpassivated counterparts [85, 87–89]. InAs-InP core-shell structures also provide quantum confinement of carriers [90], which is useful for efficient radiative recombination in single photon sources, for example [91]. InAs-InP core-shell heterostructures can be achieved via the vapour-liquid-solid (VLS) method [3]. The VLS method uses metal nanoparticles (usually Au) to collect vapour deposited materials. Once the metal nanoparticle is supersat-

urated, precipitation of the vapour-deposited material occurs, resulting in growth of the nanowire with the Au particle remaining at the tip of the nanowire. The VLS process is typically implemented using molecular beam epitaxy (MBE) [92] or metalorganic vapour phase epitaxy (MOVPE) [93–96]. In MOVPE, InP shell growth can be promoted compared to axial growth by increasing the growth temperature. At elevated temperatures, pyrolysis of the metalorganic precursors occurs on the nanowire sidewalls, resulting in lateral vapour-solid deposition [93–96]. An alternative technique for nanowire growth is MBE where growth is dominated by diffusive transport of adatoms from the substrate surface or nanowire sidewalls to the Au nanoparticle at the tip of the nanowire. Thus, radial (shell) growth of nanowires in MBE can occur by kinetically limiting adatom diffusion, resulting in vapour-solid deposition on the nanowire sidewalls. However, InAs-InP core-shell structures can be difficult to achieve in GS- MBE because the diffusion length of indium is typically greater than the nanowire length (on the order of several microns) [97]; hence, axial rather than core-shell structures are typically achieved, particularly in gas source MBE (GSMBE) as will be shown in the present study. To overcome the difficulty of achieving passivation of InAs nanowires by GSMBE, an alternative passivation scheme is examined consisting of AlInAs or AlInP shells. In this Chapter, we show that shell growth can be significantly increased in GSMBE simply by the addition of Al in the shell composition

The main challenge in realizing core-shell structures is the strain (and dislocations) that result from the lattice mismatch. It has been shown that field effect mobility is reduced in core-shell structures that have undergone strain relaxation through the formation of dislocations [98]. To reduce the likelihood of strain relaxation, a suitable shell material must be chosen. In some cases the core and the shell can be lattice matched as in the case of GaAs-$Al_{0.52}In_{0.48}P$ core-shell nanowires, eliminating the

possibility of strain relaxation [99]. In the case of InAs cores however, there are no III-V materials available (excluding ternary antimonides) for lattice matching. As a result, care must be taken not to exceed the thickness beyond which the formation of dislocations becomes favourable. The traditional way of computing the critical thickness of two dimensional epilayers is by the Matthews model [100]. In recent years there have been a number of models that have addressed the issue of dislocations in the cylindrical core-shell geometry. These models typically have considered an isotropic material and calculated the energy required to form a dislocation [101–107]. Some models have included the interactions between dislocations and strain fields. [105] More specific critical thickness models have been developed for a variety of systems including Si-Ge [108] and Al(In)GaN [109]. In this Chapter, the growth and characterization of InAs-AlInAs(P) core-shell nanowires is reviewed and a model to determine the critical shell thickness is developed.

4.2 Growth of InAs-AlInAs(P) Nanowires

4.2.1 Experimental Details

Zn-doped GaAs (111)B (1 - 5 $\times$ 10^{18} cm^{-3}) wafers were treated by UV-ozone oxidation for 20 min to remove any hydrocarbon contamination and to grow a sacrificial oxide. The wafers were then dipped in buffered HF for 30 s and rinsed under flowing deionized water for 10 min. The wafers were dried with N_2 and transferred to an electron beam evaporator where a 1 nm thick Au film was deposited at room temperature at a rate of 0.1 nm/s as measured by a quartz crystal thickness monitor. The wafers were then transferred to a gas source molecular beam epitaxy (GSMBE) system (SVT Associates). In GSMBE, group III species (In, Al) are supplied as

Table 4.1: Description of InAs/AlInAs(P) nanowire samples.

Segments Grown	Lattice Mismatch Strain (%)
InAs - InP	3.1
InAs - $Al_{0.20}In_{0.80}As$	1.3
InAs - $Al_{0.36}In_{0.64}As$	2.4
InAs - $Al_{0.53}In_{0.47}As$	3.5
InAs - $Al_{0.36}In_{0.64}P$	5.5
InAs - $Al_{0.53}In_{0.47}P$	6.6

monomers from an effusion cell, and group V species (P, As) are supplied as P_2 and As_2 dimers that are cracked from PH_3 and AsH_3 in a gas cracker operating at 950°C. Prior to growth, the wafers were placed in a pre-deposition chamber where they were degassed for 15 min at 300°C. After transferring the wafers to the growth chamber, an oxide desorption step was performed where they were heated to 540°C under inductively coupled hydrogen plasma and As_2 overpressure for 10 min, leading to the formation of Au nanoparticles. The sample was cooled to the growth temperature of 420 °C and nanowire growth was initiated by opening the In shutter. InAs was grown for 15 min at an equivalent 2D growth rate of 0.14 nm/s. After growth of the InAs, the growth was switched to $Al_xIn_{1-x}As$ or $Al_xIn_{1-x}P$ with different Al alloy fractions x, calibrated by prior 2-D depositions (see Table 4.1). The shells were grown for a duration of 7.5 min at a 2-D equivalent rate of 0.14 nm/s.

The nanowire morphology was determined using a JEOL 7000F field emission scanning electron microscope (SEM). The nanowires were removed from the growth substrate by sonication in methanol solution for structural investigation. The solution was then drop cast onto a holey carbon grid for examination using a JEOL 2010F high resolution scanning transmission electron microscope (HRTEM) using high angle

annular dark field (HAADF) and selected area diffraction (SAD) modes. The chemical composition was determined by energy dispersive x-ray spectroscopy (EDX).

4.2.2 Results and Discussion

A representative SEM image of the nanowires is shown in Figure 4.1 for the InAs-$Al_{0.20}In_{0.80}As$ sample. Similar results were obtained for the other samples in Table 4.1. Based on the SEM analysis, the nanowires were roughly 1 μm in length and 40 nm in diameter on average with a rod-shaped morphology. Many of the nanowires grew orthogonal to the substrate surface, although tilted growth directions were also observed. The reason for the low wire density and non-orthogonal growth behaviour is not clear at present, although it may have occurred due to the lattice mismatch strain of the InAs nanowires relative to the GaAs substrate [75]. Cirlin et al. [110] demonstrated that when InAs nanowires with diameter above 44 nm, similar to the diameters in Figure 4.1, are grown on GaAs (111)B substrates, the nanowires are either dislocated or do not grow at all. Furthermore, although InAs nanowires of GaAs have been achieved by SSMBE [110], few studies have been performed by GSMBE as in the present work. Hence, subtleties in the GSMBE growth conditions and/or substrate preparation conditions may have resulted in our non-optimal nanowire morphology. Further work is required to optimize the GSMBE growth conditions to achieve a high density of vertical nanowires with monodisperse diameter.

Bare InAs nanowires, grown without any InP, AlInAs or AlInP segments, exhibited a constant diameter, negligible tapering, and a Au particle diameter roughly equal to the nanowire diameter as shown in the representative TEM image of Figure 4.2(a). These observations indicate that InAs nanowires grew in the axial direction by the VLS process with negligible vapour-solid growth on the nanowire sidewalls.

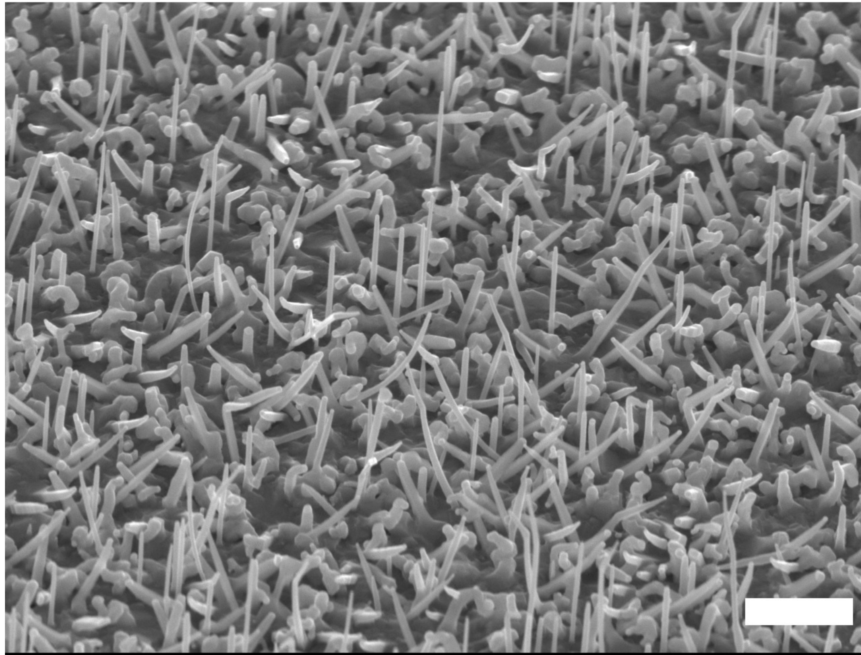

Figure 4.1: 45° tilted SEM image of InAs-$Al_{0.20}In_{0.80}As$ sample. Scale bar is 1 μm.

Growth of an InP segment following the InAs segment also resulted in a purely axial heterostructure with negligible radial (shell) growth as shown in Chapter 3 where a detailed analysis of the axial InAs-InP heterostructures has been reported [34].

The purely axial growth of InAs or InAs-InP nanowires can be explained by the diffusion length of In adatoms exceeding the length of the nanowires [34,97]. In such a case, In adatoms can diffuse from the substrate or nanowire sidewalls to reach the Au particle at the top of the nanowire, contributing to axial VLS growth and negligible radial growth. While such axial InAs-InP heterostructures are interesting in their own right, they do not permit the core-shell structure that is required for passivation. To achieve a shell surrounding an InAs core, the alternative shell material consisting of AlInAs or AlInP was examined.

The structure of the InAs-AlInAs and InAs-AlInP nanowires was examined by HAADF images where larger atomic mass appears as brighter contrast. Figure 4.2(b-d) shows representative HAADF images for the InAs-$Al_{0.20}In_{0.80}As$ and InAs-$Al_{0.53}In_{0.47}P$

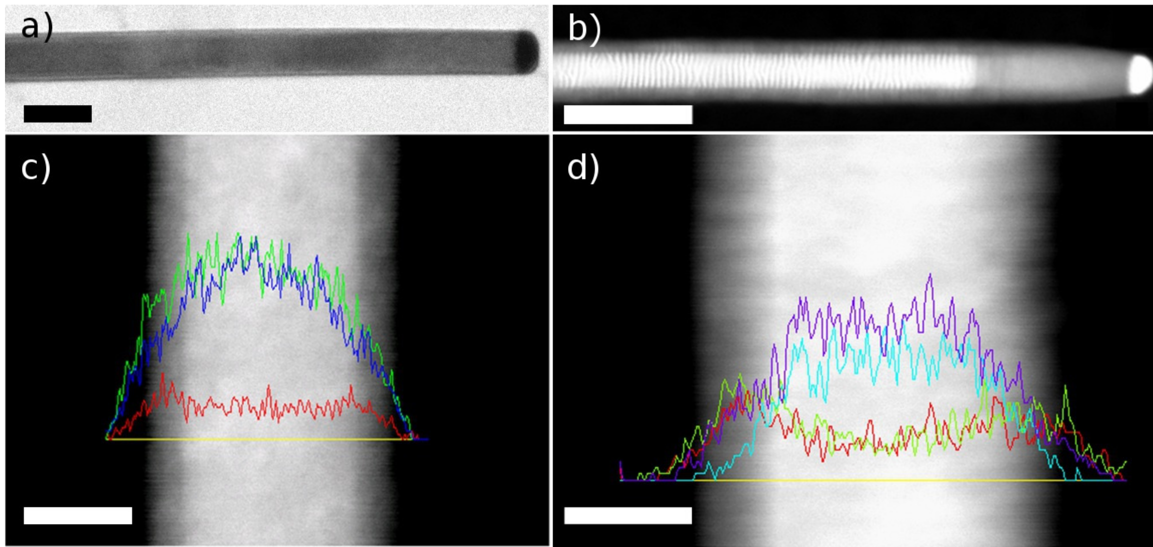

Figure 4.2: (a) BF-TEM image of InAs nanowire without a shell. Scale bar is 100 nm. (b) HAADF image of InAs-$Al_{0.53}In_{0.47}P$ core-shell nanowire. Scale bar is 100 nm. (c) HAADF image of InAs-$Al_{0.20}In_{0.80}As$ core-shell nanowire with superimposed EDX linescan (Al: red, In: blue, As: green). Scale bar is 20 nm. (d) HAADF image of InAs-$Al_{0.53}In_{0.47}P$ core-shell nanowire with superimposed EDX linescan (Al: red, In: purple, As: turquoise, P: green). Scale bar is 20 nm.

nanowires. Similar results were obtained for the other samples in Table 4.1. The lighter contrast near the nanowire axis indicates the InAs core, while the darker contrast along the nanowire edge indicates the presence of an AlInAs (Figure 4.2(c)) or AlInP (Figure 4.2(b, d)) shell. This core-shell geometry was verified by EDX linescans across the nanowire diameter superimposed on the HAADF images. Al content peaked at the edges of the nanowire in Figure 4.2(c) consistent with an AlInAs shell, while Al and P content peaked at the edges of the nanowire in Figure 4.2(d) consistent with an AlInP shell. As observed in Figure 4.2(b), the shell thickness was remarkably uniform along the entire nanowire length.

In contrast to bare InAs nanowires or InAs-InP nanowires that had a nanowire diameter equal to the Au particle diameter, the core-shell InAs-AlInAs and InAs-AlInP nanowires exhibited a slight tapering of the diameter near the top of the nanowire as observed in Figure 4.2(b). This tapering indicates that the AlInAs and

AlInP depositions occurred as vapour-solid deposition on the nanowire sidewalls over the InAs core, slightly increasing the nanowire diameter compared to the Au particle. A certain degree of axial growth of the AlInAs or AlInP material was also observed vertically above the InAs core as seen by the darker image contrast below the Au particle in Figure 4.2(b). Measurement of these axial segments indicated lengths between 65 and 70 nm for all nanowires, which is near the expected contribution due to direct impingement on the Au particle (0.14 nm/s $\times$ 7.5 min = 63 nm). As the nanowire grows axially by direct impingement on the Au particle, radial growth can occur simultaneously on the newly formed core by direct impingement (vapour-solid growth) on the core sidewalls. The tapering near the tip of the nanowire has been explained by a step-flow growth mechanism [111, 112]. Hence, during deposition of the AlInAs or AlInP, there appeared to be negligible contribution to the axial growth due to adatom diffusion from the nanowire sidewalls or substrate surface. Comparing the latter results to the bare InAs or InAs-InP axial structures considered earlier, it is clear that the presence of Al in the shell results in a transition of the growth mode from axial to radial growth.

The nominal shell thickness can be calculated as follows. Although the substrate is rotated during growth to ensure a uniform flux distribution on the surface, the flux sees a rectangle of height $L \sin\theta$ (equal to the nanowire height) and width D, where $\theta = 35°$ is the angle of the molecular beam relative to the substrate surface, and D is the nanowire core diameter. The number of atoms per unit time contributing to the axial growth is simply $JDL\sin\theta$ where J is the impinging group III flux ($\mathrm{nm^{-2}s^{-1}}$), which translates to a volume growth rate of $dV/dt = FDL\sin\theta$ where F is the 2-D equivalent growth rate ($\mathrm{nm\,s^{-1}}$). The shell thickness δR can be estimated by equating the latter volume to that of a shell wrapped around a cylindrical core of diameter D [111]:

$$tFDL\sin\theta = L\left[\pi\left(\frac{D}{2}+\delta R\right)^2 - \frac{\pi D^2}{4}\right] \tag{4.1}$$

where t is the deposition time. The left-hand expression of Equation (4.1) is the total volume of material collected by the nanowire sidewalls due to direct impingement while the right-hand expression is the volume of the resulting shell. Rearranging Equation (4.1), the thickness of the shell can be determined as:

$$\delta R = \frac{D}{2}\left(\sqrt{\frac{4\delta R_o}{D}+1} - 1\right) \tag{4.2}$$

where $\delta R_o = Ft\sin\theta/\pi$ is the shell thickness for large core diameters ($D >> \delta R_o$). The independence of δR_o with regard to nanowire length and diameter can be understood by the fact that the adatom collection area is proportional to the nanowire surface area ($L\pi D$), while the thickness of the shell is inversely proportional to surface area. Using the shell growth conditions of $t = 7.5$ min, $F = 0.14$ nm/s, and $\theta = 35°$ gives $\delta R_o = 11.5$ nm. Measurements by HRTEM in over 20 nanowires among the samples in Table 4.1 indicated an average core diameter and standard deviation of 34 ± 7 nm. According to Equation (4.2), this average core diameter corresponds to a shell thickness of 9 nm. The average shell thickness and standard deviation measured directly by HRTEM, such as that shown in Figure 4.2, was 10 ± 1 nm, consistent with the above estimate.

As the Al content x in the shells increased, the lattice mismatch between the InAs core and the $Al_xIn_{1-x}As$ or $Al_xIn_{1-x}P$ shell increased (see Table 4.1). This increases the strain between the two materials and, if a critical thickness is exceeded, the shell will relax and misfit dislocations will be introduced [107–109, 113, 114]. This strain relaxation can be seen in the periodic Moiré fringes along the nanowire length such as

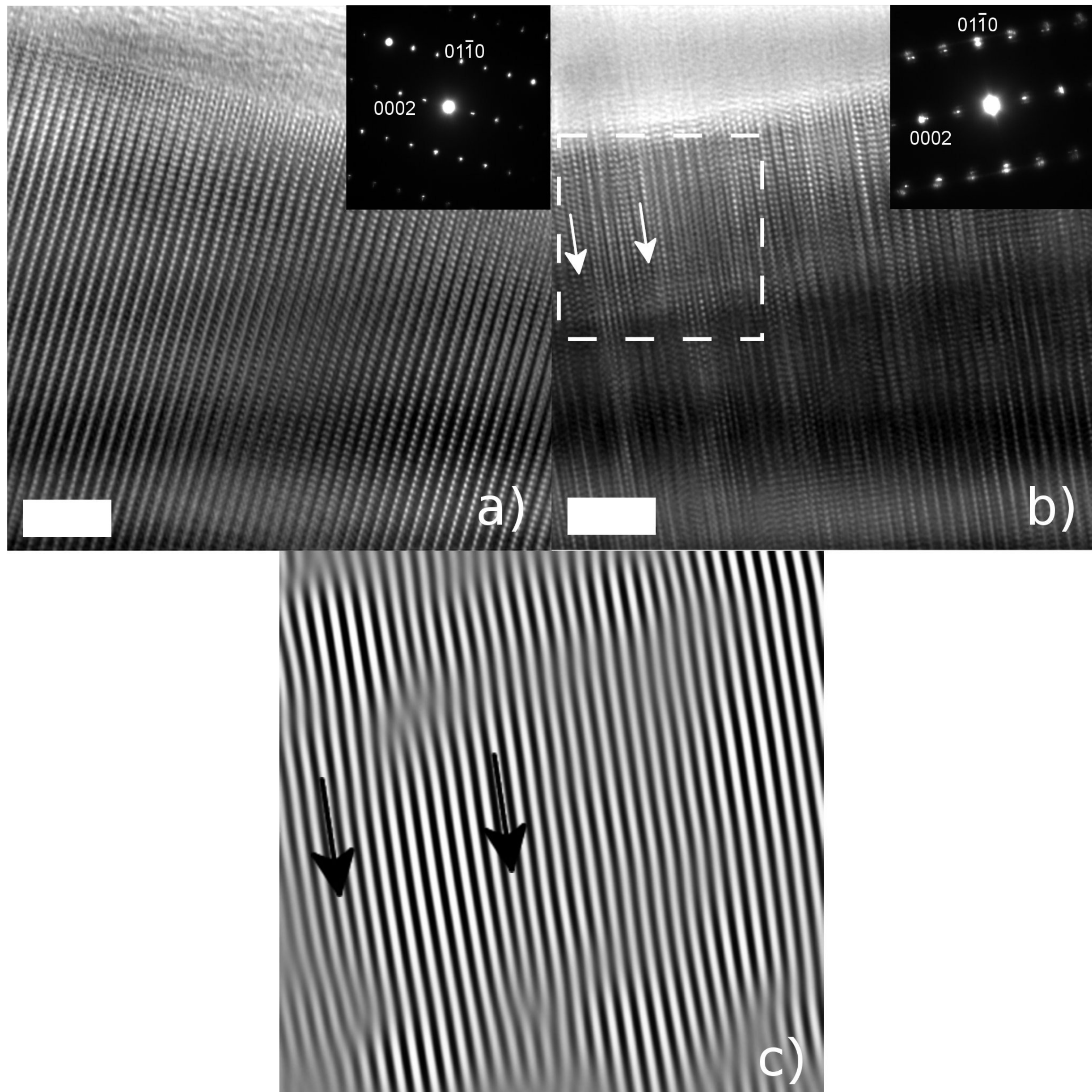

Figure 4.3: HRTEM along the $(2\bar{1}\bar{1}0)$ zone axis for (a) InAs-$Al_{0.20}In_{0.80}As$ and (b) InAs-$Al_{0.53}In_{0.47}P$ core-shell nanowire. Scale bars are 5 nm. Insets in (a) and (b) show SAD patterns. Arrows in (b) indicate the positions of dislocations in the shell c) Resulting IFFT of masked (0002) FFT from boxed area in (b).

that shown in Figure 4.2(b). Assuming complete relaxation of the shell, the spacing between Moiré fringes can be predicted according to $L = a_1a_2/(a_2 - a_1)$ where a_1 and a_2 are the (111) lattice spacing of the shell and core, respectively. For example, using $a_2 = 6.0583/\sqrt{3}$ Å for the InAs core and $a_1 = 5.6564/\sqrt{3}$ Å for the $Al_{0.53}In_{0.47}P$ shell [9] gives $L = 4.9$ nm, which is close to the measured value of $L = 4.7$ nm. Similar Moiré fringes were observed in InAs-GaAs core-shell nanowires [98, 115, 116]. Moiré fringes were observed in all the AlInP samples indicating strain relaxation. Moiré fringes were not evident in the AlInAs samples, which have lower strain compared to the AlInP samples (see Table 4.1), suggesting only partial relaxation or pseudomorphic growth.

Keplinger et. al. [117] used grazing incidence x-ray diffraction to map a "phase diagram" of the transition from pseudomorphic to plastically relaxed shell growth for InAs-InAsP core-shell nanowires. These results indicated that a pseudomorphic shell of 1.3% strain (similar to $Al_{0.20}In_{0.80}As$) can have a thickness no greater than ~20 nm, while a strain of 2.4% (similar to $Al_{0.36}In_{0.64}As$) is expected to be plastically relaxed for all shell thicknesses. Raychaudhuri et al. [109] showed that an InAs nanowire core with InGaAs shell of 1.3% strain (similar to $Al_{0.20}In_{0.80}As$) and 10 nm thickness will be dislocation-free for nanowire diameters less than 30 nm. 7 - 10 nm thick InP shells on InAs cores of 20 nm diameter (3.1% strain) have shown no dislocations [95]. Considering the above results, the $Al_{0.20}In_{0.80}As$ shells are expected to be pseudomorphic, while the other AlInAs samples (Table 4.1) may be pseudomorphic or partially relaxed. The AlInP shells are expected to be completely relaxed.

HRTEM, such as the representative images in Figure 4.3(a,b), indicated that all nanowires exhibited the wurtzite crystal structure as commonly found in III-V nanowires [118]. The wurtzite crystal structure of the nanowires was confirmed by SAD as represented in the inset of Figure 4.3(a) and (b). A common occurrence

in III-V nanowires is the existence of stacking faults whereby the crystal structure alternates between zincblende and wurtzite, or exhibits twinning, along the nanowire length [118]. Stacking faults in our core-shell nanowires occurred rarely (a few per nanowire) due to the low growth rate employed (0.14 nm/s), similar to the stacking-fault free GaAs nanowires described previously [76, 119].

Misfit dislocations were evident in the HRTEM images of the AlInP nanowires such as Figure 4.3(b) for the InAs-$Al_{0.47}In_{0.53}P$ nanowire. Some representative dislocations are indicated by white arrows in Figure 4.3(b). Spot splitting in the SAD pattern of InAs-AlInP nanowires, such as that shown in the inset of Figure 4.3(b), indicated strain relaxation, similar to previous reports for InAs-GaAs core-shell nanowires [98, 120]. On the other hand, no misfit dislocations were evident in the HRTEM images of any AlInAs shells (for all samples in Table 4.1, such as that in Figure 4.3(a) for an InAs-$Al_{0.20}In_{0.80}As$ nanowire, consistent with the lack of spot splitting in the SAD patterns (e.g., inset of Figure 4.3(a)). The lattice-matching in Figure 4.3(a) makes the InAs-AlInAs interface difficult to discern, although a core-shell structure was confirmed by HAADF imaging as in Figure 4.2.

To make the dislocations more visible, a Fast Fourier Transform (FFT) was performed on the area enclosed by the dotted lines in Fig 4.3(b). A mask was applied to the FFT to show only the (0002) reflections and an inverse FFT was then performed. This procedure highlights the representative dislocations shown as black arrows in Figure 4.3(c), which correspond to the same dislocations shown as white arrows in Figure 4.3(b). The dislocations are particularly evident below the black arrows in Figure 4.3(c).

In the absence of Al, the adatom diffusion length of In evidently exceeds the nanowire length, resulting in purely axial growth of InAs and InP. In contrast, AlInAs or AlInP deposition resulted predominantly in radial growth. The addition of

even a small amount of Al (x = 0.20) had a remarkable effect in reducing the VLS growth and, instead, promoted vapour-solid growth on the nanowire sidewalls. Although the growth mechanisms responsible for this effect are not fully understood, the adatom diffusion appeared to be significantly reduced during shell growth. Based on prior studies [52, 121], the adatom diffusion length of In, Ga and Al are believed to consecutively decrease. Al adatoms, in particular, are known to have a relatively short diffusion length, which has been used to create AlGaAs shells on GaAs cores [52, 122]. In addition, the effect of Al on the phase of the Au seed particle is not currently known. Based on the bulk phase diagrams [123, 124], the growth temperature of 420°C is close to the Au-In eutectic temperature of 450°C but well below the Au-Al eutectic temperature of 525°C. Hence, solidification of the Au particle and significant slowing of the axial growth due to changes in bulk solubility or diffusion may occur with the addition of Al. However, it should be noted that any Al content in the Au particle was below the detection limit of EDX. Finally, the addition of Al may have surfactant effects which reduces the In adatom surface diffusivity on the nanowire sidewalls [125, 126].

4.2.3 Summary

The present results are expected to extend MBE-grown nanowires into new device applications, for example InAs-AlInAs nanowires for MOSFET devices, similar to planar HEMTs [127]. Work is currently in progress to demonstrate the passivating properties of AlInAs for carrier transport in channels comprised of InAs nanowires. Note that the InAs-AlInAs and InAs-AlInP material system are type I heterostructures suitable for carrier confinement [128]. While the InAs-AlInP system exhibited misfit dislocations, the InAs-AlInAs system with low Al content appeared defect-free. Our results are generally applicable to other nanowire systems such as the passiva-

tion of InP nanowires using lattice-matched $Al_{0.48}In_{0.52}As$, or the passivation of GaAs using lattice-matched $Al_{0.52}In_{0.48}P$.

4.3 Strain Model

The strain model presented here was developed using the method of Trammell et al. where Si-Ge core-shell nanowires were studied [108]. This model was extended to describe the wurtzite structures observed in our InAs-AlInAs(P) nanowires as verified by TEM. In bulk form, all of the alloys considered here adopt the cubic zincblende crystal structure. As a result, we must convert the relevant parameters for the model from the tabulated zincblende values to their wurtzite counterparts. The in-plane equilibrium lattice constant is given by $a_o^r = a_{ZB}/\sqrt{2}$ and the c-axis equilibrium lattice constant is given by $a_o^z = \sqrt{8/3}\ a_o^r$ where a_{ZB} is the bulk zincblende lattice constant [129] The well known Martin transformation was used to obtain the stiffness tensor and is described in the next section.

4.3.1 Martin Transformation

In 1972, R. M. Martin laid out a method to relate the elastic stiffness tensor of zincblende crystals to that of wurtzite crystals [130]. This method is based on the fact that both the cubic zincblende and hexagonal wurtzite structures are tetrahedrally coordinated. The difference is simply the way the tetrahedra are connected, in particular the second nearest neighbours are rotated but otherwise identical. This allows the combination of a rotation and an internal strain compensation to estimate the wurtzite stiffness constants given the zincblende values. Martin cited previous work [131–135] that justified the assumption that long range third nearest neighbour interactions do not play a role in determining the elastic properties. The validity of

the transformation has been verified by experiment in semiconductors that readily crystallize in both the zincblende and wurtzite structures such as ZnS [136]. In our study the nanowire cores were InAs, while the shell material was a ternary alloy of $Al_xIn_{1-x}As$ or $Al_xIn_{1-x}P$. The lattice parameters and the stiffness constants for these materials were calculated using Vegard's law [9].

To describe the transformation, we will begin by defining the concepts of stress and strain. These concepts are related by Hooke's law, which states that [137]:

$$\epsilon_{ij} = s_{ijkl}\sigma_{kl}, \quad \sigma_{ij} = c_{ijkl}\epsilon_{kl} \tag{4.3}$$

where ϵ is the strain, s is the compliance, σ is the stress, and c is the stiffness. Homogeneous stress and strain are second rank tensors which are represented by symmetric matrices. In general, if a homogeneous stress is applied to a crystal, a homogeneous strain will be generated. The resulting strain in one particular direction is related to all of the stress components, for example [137]:

$$\begin{aligned} \epsilon_{11} = & s_{1111}\sigma_{11} + s_{1112}\sigma_{12} + s_{1113}\sigma_{13} \\ & + s_{1121}\sigma_{21} + s_{1122}\sigma_{22} + s_{1123}\sigma_{23} \\ & + s_{1131}\sigma_{31} + s_{1132}\sigma_{32} + s_{1133}\sigma_{33} \end{aligned} \tag{4.4}$$

We can reduce the number of compliance elements by considering simple symmetry arguments. For example, $s_{ijkl} = s_{ijlk}$. This reduces the 81 compliance elements to 36. Similar arguments can be made for c making $c_{ijkl} = c_{ijlk}$. The stiffness and compliance relate two second rank tensors, namely the stress and strain, making

them fourth rank tensors. The concept of a fourth rank tensor can be identified by their transformation [137]:

$$T_{ijkl} = a_{im}a_{jn}a_{ko}a_{lp}T_{mnop} \tag{4.5}$$

We can convert to the matrix notation by applying the following index abbreviations to the first two and last two sets of indicies:

Tensor notation	11	22	33	23,32	31,13	12,21
Matrix notation	1	2	3	4	5	6

Now we have $c_{ijkl} = c_{mn} \quad (i,j,k,l = 1,2,3; m,n = 1,...,6)$ resulting in a square symmetric matrix (note that for transformations, we must go back to the tensor notation). Applying the effects of crystal symmetry, the resultant matrices for the cubic and hexagonal classes, respectively are:

$$C_{mn}^{ZB} = \begin{pmatrix} c_{11} & c_{12} & c_{12} & 0 & 0 & 0 \\ & c_{11} & c_{12} & 0 & 0 & 0 \\ & & c_{11} & 0 & 0 & 0 \\ & & & c_{44} & 0 & 0 \\ & & & & c_{44} & 0 \\ & & & & & c_{44} \end{pmatrix} \tag{4.6}$$

$$C_{mn}^{WZ} = \begin{pmatrix} c_{11} & c_{12} & c_{13} & 0 & 0 & 0 \\ & c_{11} & c_{13} & 0 & 0 & 0 \\ & & c_{33} & 0 & 0 & 0 \\ & & & c_{44} & 0 & 0 \\ & & & & c_{44} & 0 \\ & & & & & \frac{1}{2}(c_{11}+c_{12}) \end{pmatrix} \tag{4.7}$$

We only need to find a transformation for the tetrahedra. In zincblende we have four equivalent tetrahedra along the [111],[$1\bar{1}\bar{1}$], [$\bar{1}1\bar{1}$], [$\bar{1}\bar{1}1$] directions. In wurtzite with the x_3 axis along the c direction there are two inequivalent tetrahedra. These can be generated by taking the zincblende tetrahedra and performing the following transformations:

$$R^{(1)} = \frac{1}{\sqrt{6}} \begin{pmatrix} \sqrt{3} & 0 & \sqrt{3} \\ -1 & 2 & 1 \\ -\sqrt{2} & -\sqrt{2} & \sqrt{2} \end{pmatrix} \text{ and } R^{(2)} = \begin{pmatrix} -1 & 0 & 0 \\ 0 & -1 & 0 \\ 0 & 0 & 1 \end{pmatrix} R^{(1)} \tag{4.8}$$

These transformations generate two trigonal orientations that when combined give the proper hexagonal symmetry. This can be applied in general to any tensorial transformation using Einstein summation:

$$T_{ijkl}^{(n)} = R_{im}^{(n)} R_{jn}^{(n)} R_{ko}^{(n)} R_{lp}^{(n)} T_{mnop}^{ZB} \tag{4.9}$$

Because we ignored the interactions between tetrahedra, the wurtzite tensor is represented by the average of the two trigonal tensors obtained from Equation (4.9):

$$\bar{T}_{ijkl}^{WZ} = \frac{1}{2}(T_{ijkl}^{(1)} + T_{ijkl}^{(2)}) \tag{4.10}$$

The averaging procedure in Equation (4.10) has constraints placed upon it due to the fact that the tetrahedra are connected to other tetrahedra. We must allow the tetrahedra to vary individually subject to:

(i) The average of the strains in the two inequivalent tetrahedra are equal to the macroscopic strain

$$\epsilon_{ij} = \frac{1}{2}(\epsilon_{ij}^{(1)} + \epsilon_{ij}^{(2)}) \tag{4.11}$$

(ii) The difference in the strains are not fixed by ϵ_{ij} but subject to energy minimization of the crystal

$$\delta_{ij} = \frac{1}{2}(\epsilon_{ij}^{(1)} - \epsilon_{ij}^{(2)}) \tag{4.12}$$

Now we replace the general tensor $T_{ijkl}^{(n)}$ with the elastic stiffness tensors $C_{ijkl}^{(n)}$. Similar to the strain for the two trigonal representations we define an average elastic tensor $\bar{C}_{ijkl}^{WZ}$ and the difference Δ_{ijkl}. The strain energy of each tetrahedra can be written as:

$$\begin{aligned} U &= \frac{1}{4}\left(\epsilon_{ij}^{(1)} C_{ijkl}^{(1)} \epsilon_{kl}^{(1)} + \epsilon_{ij}^{(2)} C_{ijkl}^{(2)} \epsilon_{kl}^{(2)}\right) \\ &= \frac{1}{2}\left(2\epsilon_{ij}\bar{C}_{ijkl}^{WZ}\epsilon_{kl} + 2\delta_{ij}\bar{C}_{ijkl}^{WZ}\delta_{kl} + 2\epsilon_{ij}\Delta_{ijkl}\delta_{kl} + 2\delta_{ij}\Delta_{ijkl}\epsilon_{kl}\right) \end{aligned} \tag{4.13}$$

where $\Delta_{ijkl} = 1/2(C_{ijkl}^{(1)} + C_{ijkl}^{(2)})$. The internal strain δ_{ij} above is obtained by minimizing U giving:

$$\begin{aligned} U &= \frac{1}{2}\epsilon_{ij} C_{ijkl}^{WZ} \epsilon_{kl} \\ U &= \frac{1}{2}\epsilon_{ij}\left(\bar{C}_{ijkl}^{WZ} - \Delta_{iji'j'}(\bar{C}^{WZ})_{i'j'k'l'}^{-1}\Delta_{k'l'kl}\right)\epsilon_{kl} \end{aligned} \tag{4.14}$$

This is the final transformation from ZB to WZ involving the average elastic tensor and the internal strain correction term. Using the reduced index notation described above, we can write a column vector containing the relevant zincblende and wurtzite elastic constants:

$$C^{ZB} = \begin{pmatrix} C_{11}^{ZB} \\ C_{12}^{ZB} \\ C_{44}^{ZB} \end{pmatrix} \text{ and } C^{WZ} = \begin{pmatrix} C_{11}^{WZ} \\ C_{33}^{WZ} \\ C_{12}^{WZ} \\ C_{13}^{WZ} \\ C_{44}^{WZ} \\ C_{66}^{WZ} \end{pmatrix}$$

The wurtzite column vector is also valid for $\bar{C}^{WZ}$. The transformations described in Equation (4.9) can be summarized in compact form:

$$\bar{C}_i^{WZ} = \sum_{j=1}^{3} P_{ij} C_j^{ZB} \tag{4.15}$$

$$\Delta = \sum_{j=1}^{3} Q_j C_j^{ZB} \tag{4.16}$$

where P and Q are [137]:

Table 4.2: Non-zero components of the stiffness tensor c_{ij}. Shown are the tabulated zincblende [9,138] and calculated wurtzite values. Components of the stiffness tensor for ternary alloys $Al_xIn_{1-x}P$ and $Al_xIn_{1-x}As$ were computed using Vegard's law [9].

	Zincblende [GPa]			Wurtzite [GPa]						
	c_{11}	c_{12}	c_{44}	c_{11}	c_{33}	c_{12}	c_{13}	c_{44}	c_{66}
InP	101.1	56.1	45.6	120.3	131.90	52.33	40.70	29.25	33.88
AlP	188.3	67.1	36.9	162.2	156.70	77.37	82.90	51.94	42.43
InAs	83.29	45.26	39.59	100.23	110.72	42.04	31.54	24.97	29.1
AlAs	119.9	57.5	56.6	141.69	153.77	52.65	40.57	38.68	44.52

$$P = \frac{1}{6}\begin{pmatrix} 3 & 3 & 6 \\ 2 & 4 & 8 \\ 1 & 5 & -2 \\ 2 & 4 & -4 \\ 2 & -2 & 2 \\ 1 & -1 & 4 \end{pmatrix} \quad \text{and} \quad Q = \frac{1}{3\sqrt{2}}\begin{pmatrix} 1 & -1 & -2 \end{pmatrix} \tag{4.17}$$

The internal strain term in Equation (4.14) can be accounted for by considering $\bar{C}_i^{WZ}$, and Δ resulting in:

$$C_i^{WZ} = \bar{C}_i^{WZ} - D_i \quad , \; i = 1 \dots 6 \tag{4.18}$$

where $D_1 = -D_3 = D_6 = \Delta^2/\bar{C}_5^{WZ}$, $D_2 = D_4 = 0$, and $D_5 = \Delta^2/\bar{C}_1^{WZ}$

4.3.2 Core-Shell Nanowire Model

The nanowire geometry for this model consists of two coaxial cylinders (referred hereafter as core and shell) of different lattice constant and stiffness tensor. The strain was calculated through a two-step equilibration process. In Step 1, the core

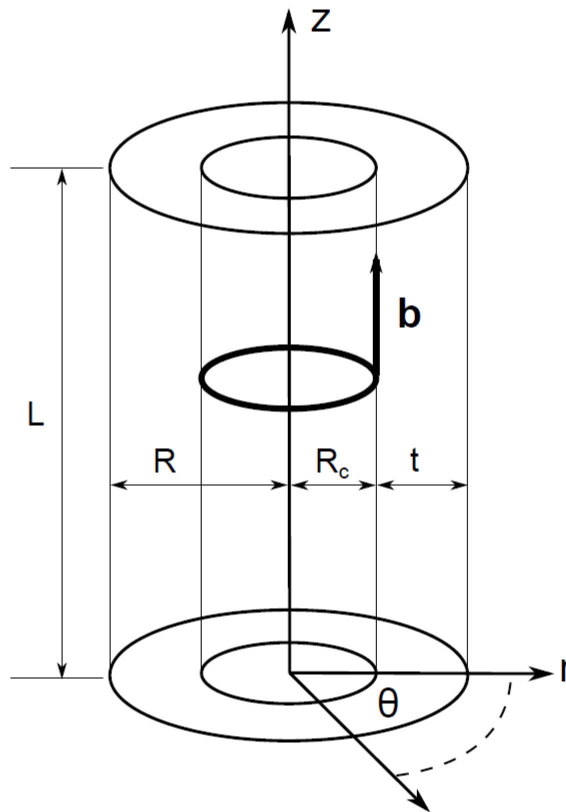

Figure 4.4: Geometry of the InAs-$Al_xIn_{1-x}As$ core-shell nanowire of length L, radius R, core radius R_c, and shell thickness t in the (r, θ, z) coordinate system. Also shown is the location of a dislocation with Burgers vector $\boldsymbol{b}$.

and shell were considered in their initial un-strained state and to be incoherent with each other. The reference state was then defined by establishing the condition of epitaxy where a single lattice constant is maintained throughout the system. For this model, the reference in-plane and z-axis lattice constants were chosen to be those of the core, $a^{\mathrm{ref}} = a_r^c$ and $a^{\mathrm{ref}} = a_z^c$. In Step 2 the system was allowed to elastically relax to the final state. This results in an expression for the total strain for $k = r, \theta, z$:

$$\mathrm{e}_k^i = \frac{a_k^c}{a_k^i}\left(\epsilon_k^i + m_k^i\right) \tag{4.19}$$

where $m_k^i = (a_k^i - a_k^c)/a_k^c$ is the misfit strain from the reference state in Step 1, $\epsilon_k^i = (a_f^i - a_k^c)/a_k^c$ is the displacement strain resulting from Step 2 where a_f^i is the final lattice constant, and i refers to the core or shell.

The displacement strains from Equation (4.19) can be written in terms of the actual displacement $u_{r,\theta,z}$ in cylindrical coordinates: [139]

$$\epsilon_{rr} = \frac{\partial u_r}{\partial r} \tag{4.20}$$

$$\epsilon_{\theta\theta} = \frac{1}{r}\frac{\partial u_\theta}{\partial \theta} + \frac{u_r}{r} \tag{4.21}$$

$$\epsilon_{zz} = \frac{\partial u_z}{\partial z} \tag{4.22}$$

$$\epsilon_{rz} = \frac{1}{2}\left(\frac{\partial u_z}{\partial r} + \frac{\partial u_r}{\partial z}\right) \tag{4.23}$$

$$\epsilon_{\theta z} = \frac{1}{2}\left(\frac{\partial u_\theta}{\partial z} + \frac{1}{r}\frac{\partial u_z}{\partial \theta}\right) \tag{4.24}$$

$$\epsilon_{r\theta} = \frac{1}{2}\left(\frac{1}{r}\frac{\partial u_r}{\partial \theta} + \frac{\partial u_\theta}{\partial r} - \frac{u_\theta}{r}\right) \tag{4.25}$$

Taking into account the cylindrical symmetry of the system as depicted in Figure 4.4, we conclude that there are no displacements in the tangential direction,

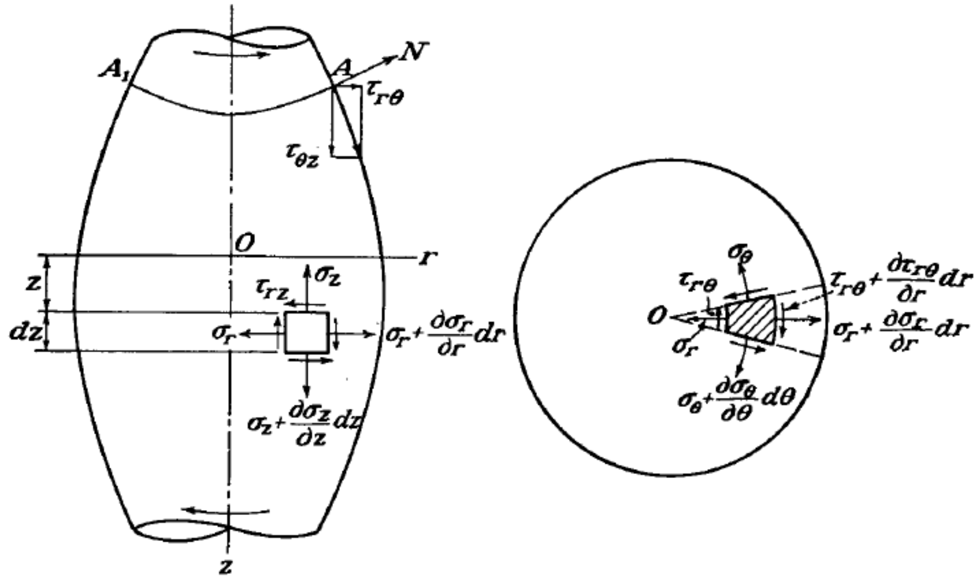

Figure 4.5: Body element for a system described in cylindrical coordinates [139].

$u_\theta = 0$. This results in the elimination of any θ-dependent terms in Equations (4.20) - (4.25) resulting in the following simplified equations:

$$\epsilon_{rr} = \frac{\partial u_r}{\partial r} \tag{4.26}$$

$$\epsilon_{\theta\theta} = \frac{u_r}{r} \tag{4.27}$$

$$\epsilon_{zz} = \frac{\partial u_z}{\partial z} \tag{4.28}$$

These displacements were solved by applying a series of boundary conditions appropriate to the core-shell nanowire geometry. The first boundary condition is a statement of mechanical equilibrium due to the absence of external loading. This boundary condition is determined by considering the body element of the system shown in Figure 4.5 and resolving all of the stresses σ and torques τ on the element [140].

The resulting equations from this process are:

$$\frac{1}{r}\frac{\partial \sigma_r r}{\partial r} + \frac{1}{r}\frac{\partial \tau_{r\theta}}{\partial \theta} + \frac{\partial \tau_{rz}}{\partial z} - \frac{\sigma_\theta}{r} = 0 \tag{4.29}$$

$$\frac{1}{r}\frac{\partial \tau_{\theta r} r}{\partial r} + \frac{1}{r}\frac{\partial \sigma_\theta}{\partial \theta} + \frac{\partial \tau_{\theta z}}{\partial z} = 0 \tag{4.30}$$

$$\frac{1}{r}\frac{\partial \tau_{rz} r}{\partial r} + \frac{1}{r}\frac{\partial \tau_{\theta z}}{\partial \theta} + \frac{\partial \sigma_z}{\partial z} \tag{4.31}$$

All torques τ can be eliminated from the above equations, as well as derivatives with respect to θ due to cylindrical symmetry. The core-shell nanowire is not under torsion because there are no physical sources of rotation. This results in a set of simplified equations:

$$\frac{1}{r}\frac{\partial \sigma_r r}{\partial r} - \frac{\sigma_\theta}{r} = 0 \tag{4.32}$$

$$\frac{\partial \sigma_z}{\partial z} = 0 \tag{4.33}$$

where the σ_k are given by Hooke's law (see Reference [141]):

$$\sigma_r = c_{11}\mathrm{e}_r + c_{12}\mathrm{e}_\theta + c_{13}\mathrm{e}_z \tag{4.34}$$

$$\sigma_\theta = c_{12}\mathrm{e}_r + c_{11}\mathrm{e}_\theta + c_{13}\mathrm{e}_z \tag{4.35}$$

$$\sigma_z = c_{13}\mathrm{e}_r + c_{13}\mathrm{e}_\theta + c_{33}\mathrm{e}_z \tag{4.36}$$

where c_{ij} are the stiffness tensor elements from Table 4.2. Substituting Equations (4.34) - (4.36) into Equations (4.32) - (4.33) we obtain the system of four displacement equations; u_r and u_z in the core and shell:

$$\frac{\partial^2 u_r}{\partial r^2} + \frac{1}{r}\frac{\partial u_r}{\partial r} - \frac{u_r}{r^2} = 0 \tag{4.37}$$

$$\frac{\partial^2 u_z}{\partial z^2} = 0 \tag{4.38}$$

Solutions to the displacement equations for the core and shell are:

$$u_r = \alpha r + \frac{\beta}{r} \tag{4.39}$$

$$u_z = \gamma z + \phi \tag{4.40}$$

To obtain the eight coefficients $\alpha, \beta, \gamma, \phi$ for both core and shell in the above solution we apply boundary conditions arising from geometrical and physical constraints. In the nanowire core, as $r \to 0$, $u_r^c \to \infty$ so $\beta^c = 0$. Continuity at the interfaces was maintained by requiring that the lattice constants were continuous across the interface. In the z-direction, this eliminates ϕ and requires $\gamma^c = \gamma^s$. The interface continuity is further specified by maintaining continuity in displacement and stress across the interface:

$$u_r^c(r = R_c) - u_r^s(r = R_c) = 0 \tag{4.41}$$

$$\sigma_r^c(r = R_c) - \sigma_r^s(r = R_c) = 0 \tag{4.42}$$

Since the nanowire is in mechanical equilibrium, the net force on the surfaces must be zero which is expressed as:

$$\int_0^{R_c}\int_0^{2\pi} \sigma_z^c r\, drd\theta + \int_{R_c}^{R}\int_0^{2\pi} \sigma_z^s r\, drd\theta = 0 \tag{4.43}$$

$$\sigma_r^s(r = R) = 0 \tag{4.44}$$

The resulting expressions for displacement are obtained through a lengthy solution to the system of four algebraic equations, Equations (4.41) - (4.44), to determine the four remaining coefficients $\alpha^c, \gamma^c, \alpha^s, \beta^s$. These coefficients are derived in Appendix A.

The limits of coherency were obtained by comparing the strain energy and the energy required to form a dislocation. To determine the strain energy, the displacement solutions were substituted back into the expressions for stress in Equations (4.34) - (4.36) and in the expressions for strain in Equations (4.26) - (4.28). These expressions were combined to compute the strain energy as follows:

$$U^c = \frac{1}{2}\int_0^L dz \int_0^{R_c} dr \int_0^{2\pi} d\theta\ \sigma_k^c \mathrm{e}_k^c r \tag{4.45}$$

$$U^s = \frac{1}{2}\int_0^L dz \int_{R_c}^{R} dr \int_0^{2\pi} d\theta\ \sigma_k^s \mathrm{e}_k^s r \tag{4.46}$$

where summation over $k = r, \theta, z$ is implied. In this model we only consider an edge dislocation where an extra plane of atoms is inserted in the shell in the [0001] direction. This is the only dislocation we observed experimentally [35]. The formation energy for such a dislocation is: [142]

$$W = \frac{1}{2}K\boldsymbol{b}^2 a \left(\ln\frac{8a}{r_o} - 2\right) \tag{4.47}$$

where $\boldsymbol{b}$ is the burgers vector of the dislocation, which in this case is equal to the z-axis lattice constant of the shell. a is the radius of the dislocation set equal to the core radius R_c, and r_o is the cutoff radius that eliminates a mathematical singularity at the core of the dislocation. Equation (4.47) takes into account the core energy of the dislocation. The cutoff radius is set to $\boldsymbol{b}/4$ for semiconductors [143]. K is the energy factor and is determined from the elastic constants:

$$K = (\bar{c}_{13} + c_{13})\left[\frac{c_{44}(\bar{c}_{13} - c_{13})}{c_{11}(\bar{c}_{13} + c_{13} + 2c_{44})}\right]^{1/2} \tag{4.48}$$

where $\bar{c}_{13} = \sqrt{(c_{11}c_{33})}$. To determine the point at which a dislocation is formed, we determine the geometry (core radius R_c and shell thickness t) at which the inequality $U^c + U^s > W$ occurs.

4.3.3 Results and Discussion

Figure 4.6 shows the calculated critical thickness for InAs-$Al_xIn_{1-x}As$ core-shell nanowires. As the core radius increases to infinity, the critical thickness becomes constant, meaning the model reduces to the thin film case as expected. The results in Figure 4.6 were compared with experimental data. The experimental data points in Figure 4.7 indicate the shell thickness and core diameter measured by HRTEM for a number of InAs-$Al_xIn_{1-x}As$ core-shell nanowires with nominal composition $x =$ 0.53 (sample A), 0.36 (sample B) and 0.20 (sample C) as reported previously [35]. The measured shell thickness and core diameter was in the range of 8-14 nm and 25-40 nm, respectively. In Figure 4.7, SAD images are shown from InAs-$Al_xIn_{1-x}As$

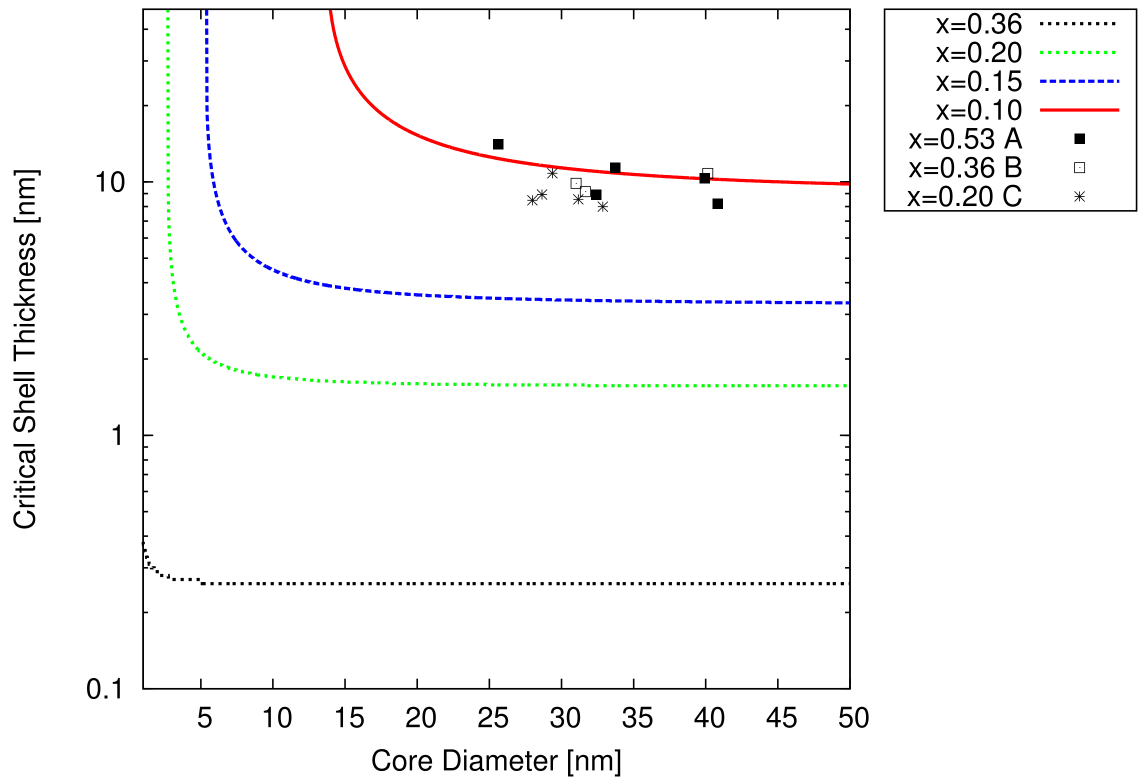

Figure 4.6: Plot of the critical $Al_xIn_{1-x}As$ shell thickness as a function of InAs core diameter for different alloy parameters, x. Also shown are data points from nanowires grown previously denoted A, B, and C.

core-shell nanowires [35]. Moving from a) - c) we show a decrease in alloy fraction and a subsequent decrease in spot splitting. Spot splitting and spot broadening are associated with strain relaxation, which in this case is due to the epitaxial mismatch between the InAs core and the $Al_xIn_{1-x}As$ shell. Similarly, in Figure 4.8 we show SAD patterns of nanowires with $Al_xIn_{1-x}P$ shells on InAs cores where larger relaxation is evident by further spot splitting. For all combinations of shell thickness and core diameter, nanowires in Figure 4.8 well exceeded the calculated critical thickness and will not be discussed further. Instead, we focus on the InAs-$Al_xIn_{1-x}As$ core-shell nanowires.

The shell thickness (8 - 14 nm) for samples A and B well exceeded the corresponding theoretical critical thickness curves for $x = 0.53$ and $x = 0.36$ nm. The critical thickness in these cases is below 1 nm in the diameter range of 25 - 40 nm. Hence, the shells in these samples are expected to relax as observed in Figure 4.7. Dislocations were also observed directly in HRTEM as described previously [35].

Experimentally, no dislocations were observed in nanowires with $x = 0.20$ (sample C) consistent with the sharp spots in Figure 4.7c). We concede however that finding a single dislocation in a nanowire that is 1 μm in length is not an easy task by HRTEM. Energy dispersive x-ray analysis (EDX) on these nanowires found that the actual composition of the shell in sample C nanowires varied from $x = 0.10$ to 0.15, somewhat below the nominal value of $x = 0.20$. Due to the proximity of the experimental data for sample C to the $x = 0.10$ theoretical curve in Figure 4.6, we might expect the shells of these samples to be coherent as observed in Figure 4.7. Overall, these data suggest that $Al_xIn_{1-x}As$ shells with $x < 0.15$ and thickness below 15 nm on InAs cores (25 - 40 nm diameter) are coherent and free of misfit dislocations.

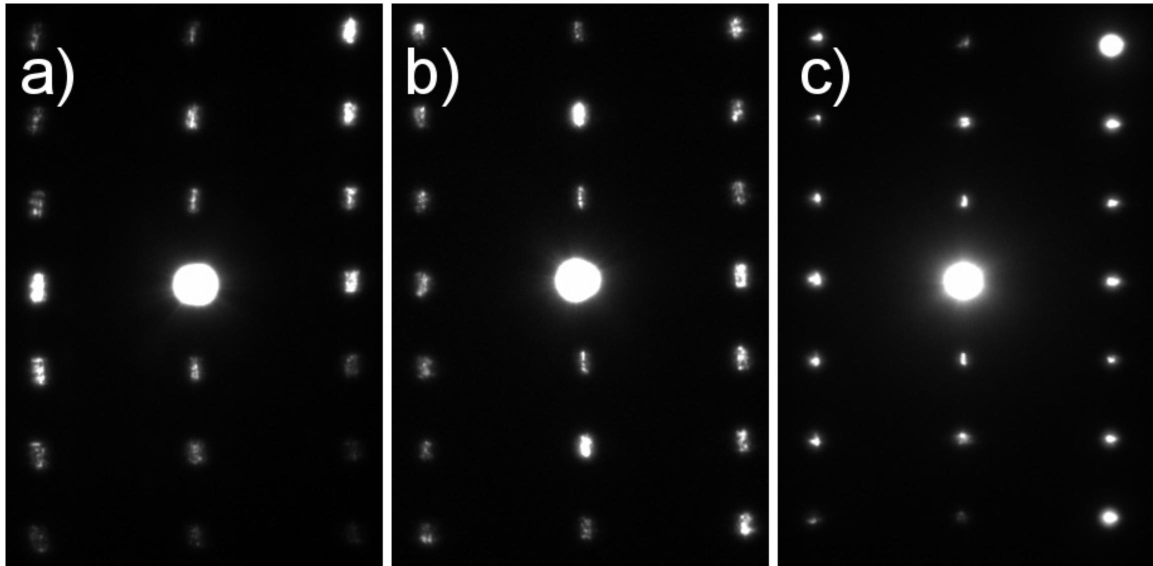

Figure 4.7: SAD pattern of InAs-Al_xIn_{1-x}As core-shell nanowires along the $[2\bar{1}\bar{1}0]$ zone axis for a) $x = 0.53$, 3.6% mismatch, b) $x = 0.36$, 2.5% mismatch, and c) $x = 0.20$, 1.3% mismatch. A, B, C from Figure 4.6 correspond to a), b) and c) in this figure.

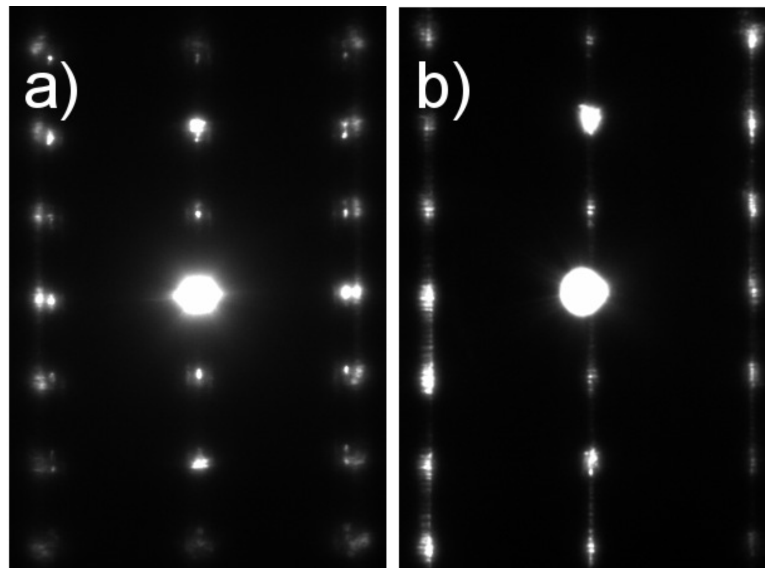

Figure 4.8: SAD pattern of InAs-Al_xIn_{1-x}P core-shell nanowires along the $[2\bar{1}\bar{1}0]$ zone axis for a) $x = 0.53$, 7.1% mismatch, b) $x = 0.36$, 5.8% mismatch

4.3.4 Summary

We have outlined a model to calculate the critical thickness for core-shell InAs-AlInAs(P) nanowires. Comparing the strain energy and the dislocation formation energy, we were able to determine the point at which the system underwent strain relaxation via the insertion of a misfit dislocation. Extending the model by Trammell [108], and using the transform by Martin [130] we have taken into account the wurtzite crystal structure of our nanowires. Comparisons with SAD patterns of InAs-AlInAs(P) core-shell nanowires with varying Al alloy parameter showed different degrees of strain accommodation due to lattice mismatch. The model predicted strain relaxation in all samples that showed SAD spot splitting. The $Al_{0.20}In_{0.80}As$ shell showed no SAD spot splitting, consistent with the model predictions when the actual Al alloy fraction measured by EDX is considered.

Chapter 5

Nanowire Passivation

5.1 Introduction

The downscaling of electronic device dimensions is accompanied by an increase in the importance of the surface due to the large surface area to volume ratio. Most III-V semiconductors have a high density of surface states that pin the Fermi level, detrimentally affecting the performance of devices. In this chapter, experimental evidence for the effectiveness of the passivation of nanowire surfaces will be presented. Two experiments were conducted. One experiment compared the electron mobility of InAs-AlInAs core-shell nanowires and unpassivated InAs nanowires in a field effect transistor (FET) device structure. A monotonic increase in mobility was observed in the core-shell nanowires while a turnover in mobility was observed for unpassivated InAs nanowires as temperature was lowered. It will be argued that the shell passivation reduces the low temperature ionized impurity scattering, indicating a reduction in surface states. This work was published by us, and our collaborators in Jonathan Baugh's group at the Institute for Quantum Computing on arXiv [37] and has recently been accepted for publication in Applied Physics Letters. A second experiment compared the photoluminescence intensity from InP nanowires passivated with ammonium polysulfide, $(NH_4)_2S_x$, and unpassivated InP nanowires. The passivation procedure produced an average 24 X increase in photoluminescence intensity which

was correlated to a two order of magnitude decrease in surface trap density [38] This work was in collaboration with Nooshin Tajik in the LaPierre group at McMaster.

5.2 Electron Transport

5.2.1 Introduction

The surface states of InAs are donor-like and cause downward band bending at the surface resulting in an accumulation layer [144]. By contributing electrons to the conduction band, these donor states become positively charged. This attracts electrons from the bulk of the nanowire and resulting in the downward band bending. In InAs this band bending is so severe that the Fermi energy is pinned above the conduction band energy. This condition is similar to that of a Si n-channel MOSFET, where a positive gate voltage is applied to the channel resulting in the attraction of electrons. Once the intrinsic Fermi energy bends below the Fermi energy, the p-type channel is converted to n-type permitting the flow of electrons. In Si MOSFETs however the band bending is rarely as severe. The major difference between Si MOSFETs and III-V nanowire field effect transistors (NWFET) is the nature of the surface. In Si MOSFETs the accumulation layer occurs at the interface betweem Si and SiO_2 which can be made to be very defect free. The electrons move along the channel with minimal scattering from the SiO_2 layer. For the InAs NWFET on the other hand, the charged surface states are a major source of ionized impurity scattering. These charged surface states also produce a random electrostatic potential along the surface and can localize and trap carriers [145]. Scanning probe microscopy at low temperature has been performed on InAs NWFET channels by Bleszynski [146]. They found signatures of localized quantum dots along the channel. While this could be

attributed to other sources such as zincblende twinning or stacking faults, it could also be attributed to randomly located states on the surface. Dramatic decreases in perfomance can also be expected for optoelectronic devices as observed by Sun et al. where a dramatic increase in μPL intensity was achieved through surface passivation of InAs nanowires [84].

5.2.2 Experimental Details

Methods for characterizing properties of traditional devices such as capacitance-voltage (C-V) and Hall effect are difficult to apply to nanowires due to their unique geometry [85]. The nanowire FET gate capacitance is too low for C-V trap state analysis and Hall effect measurements for characterizing mobility would be impossible due to the small lateral dimensions of typical nanowires. The preferred solution for characterizing nanowire transport properties is the FET device structure from which the field effect mobility can be determined. InAs-$Al_{0.2}In_{0.8}As$ core-shell nanowires and bare InAs nanowires from Chapter 4 were fabricated into FET devices using standard electron beam lithography (EBL) techniques described in Chapter 2. Transport measurements were carried out in a continuous flow He cryostat operating from 4 K to 200 K or a dilution refrigerator allowed to warm to 1.2 K. A DC voltage V_{sd} was applied between the source and drain, and the device current was measured using a current-voltage preamplifier at a 3 Hz bandwidth. A backgate voltage, V_{g} was applied to the back contact. A device schematic is shown in Figure 5.1.

5.2.3 Results and Discussion

Figure 5.3 shows the conductance $G = I_{sd}/V_{sd}$ versus V_g for Device 1. As temperature is lowered from 80K to 7K the conductance at which the device turns ON

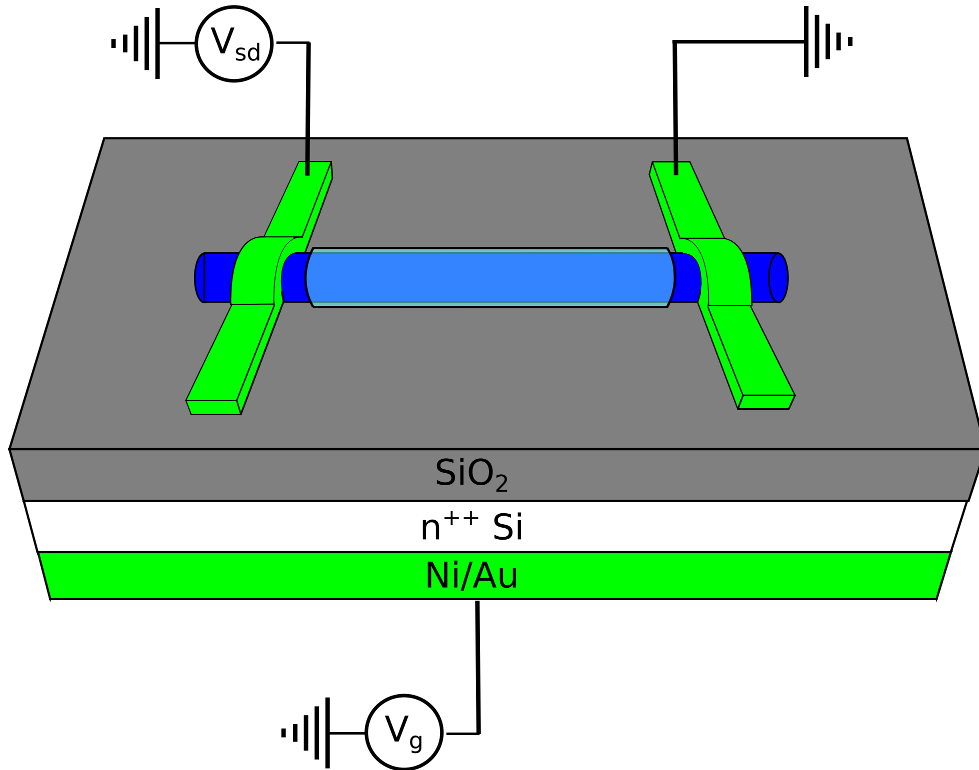

Figure 5.1: Schematic representation of an InAs-AlInAs nanowire field effect transistor (NWFET).

Table 5.1: Description of InAs-AlInAs and InAs nanowire FET devices.

Type	Device	Channel Length [nm]	Diameter [nm]
Core-Shell	1	465	80
Core-Shell	2	465	75
Core-Shell	3	940	51
Bare	4	2950	71
Bare	5	970	50
Bare	6	770	35

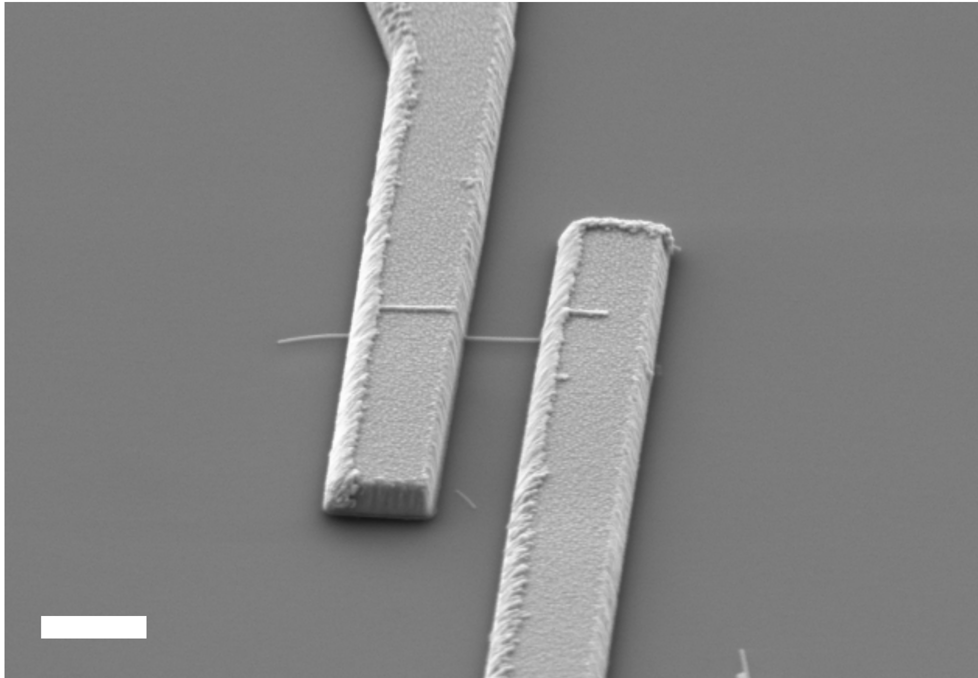

Figure 5.2: SEM image of InAs-AlInAs nanowire field effect transistor (NWFET). Scale bar is 1μm

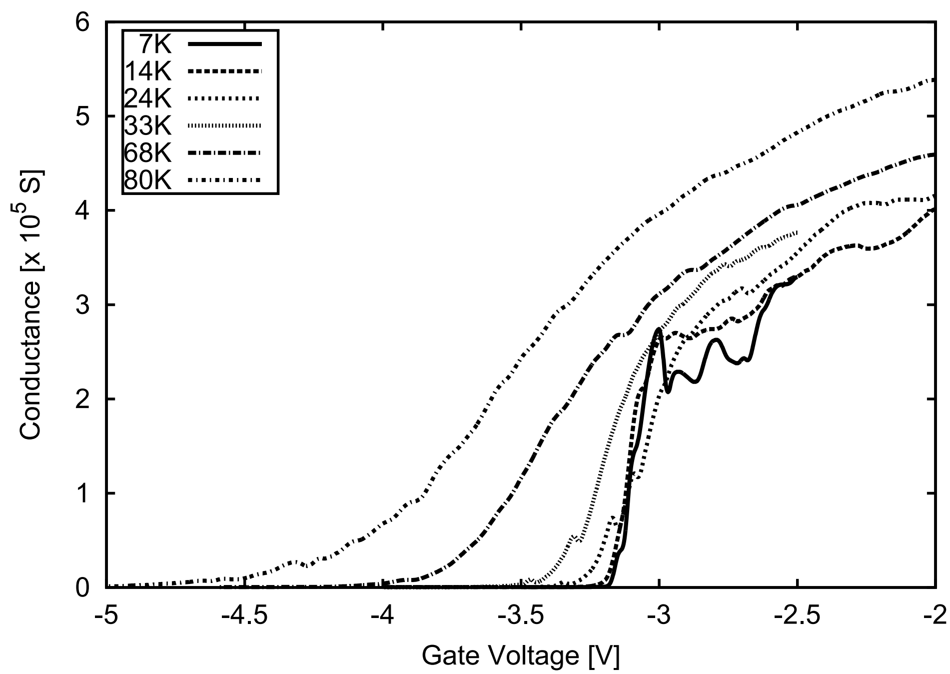

Figure 5.3: Conductance versus backgate voltage for core-shell nanowire FET Device 1 at various temperatures.

becomes less negative. This is due to the decreasing carrier concentration at low temperature as more carriers become frozen out. The field effect mobility increases indicated by the increasing slope at low temperature. The field effect and effective mobilities are defined as:

$$\mu_{\text{fe}} = \frac{L}{C_g}\frac{dG}{dV_g} \tag{5.1}$$

$$\mu_{\text{eff}} = \frac{L}{C_g}\frac{G}{V_g - V_T} \tag{5.2}$$

where L is the channel length and C_g is the gate capacitance. C_g is estimated as the capacitance of a wire above an infinite conducting plane in series with the capacitance between the core and shell [147]. The pinchoff threshold voltage V_T for Device 1 is shown in Figure 5.4. As the voltage becomes more negative, the nanowire becomes depleted of carriers and eventually the channel between the source and drain contacts is pinched off. V_T is determined by taking the $G = 0$ intercept of the maximum slope $(dG/dV_g)_{max}$ of the conductance. V_T becomes more negative with increasing temperature as a result of the thermal activity of the surface donor states. As more donor states become activated, the downward band bending is increased leading to a stronger accumulation at the surface, requiring more negative voltages to pinch off the device.

The field effect mobility and the effective mobility are shown in Figure 5.5 for Device 1. The difference between μ_{fe} and μ_{eff} is that μ_{fe} is only valid at the peak mobility when the FET is operating in the linear regime. This is evident from Equation (5.1) because the transconductance dG/dV_g is defined in the linear regime only. μ_{eff} is a smoother function and μ_{fe} is considered a lower bound on μ_{eff}, so μ_{eff} will be used as a measure of mobility in the following.

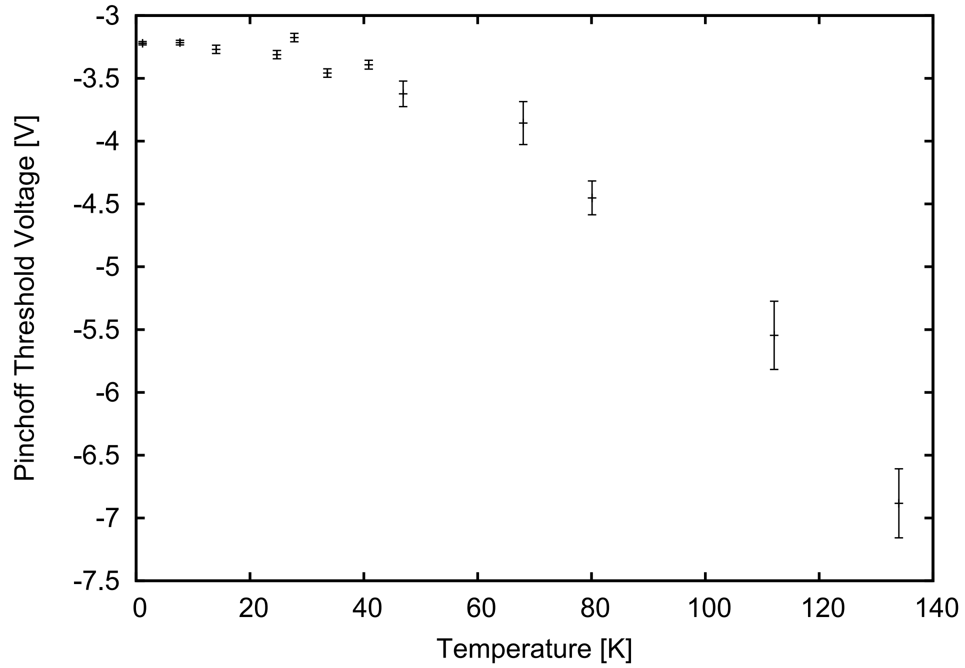

Figure 5.4: Pinchoff threshold voltage as a function of temperature for Device 1.

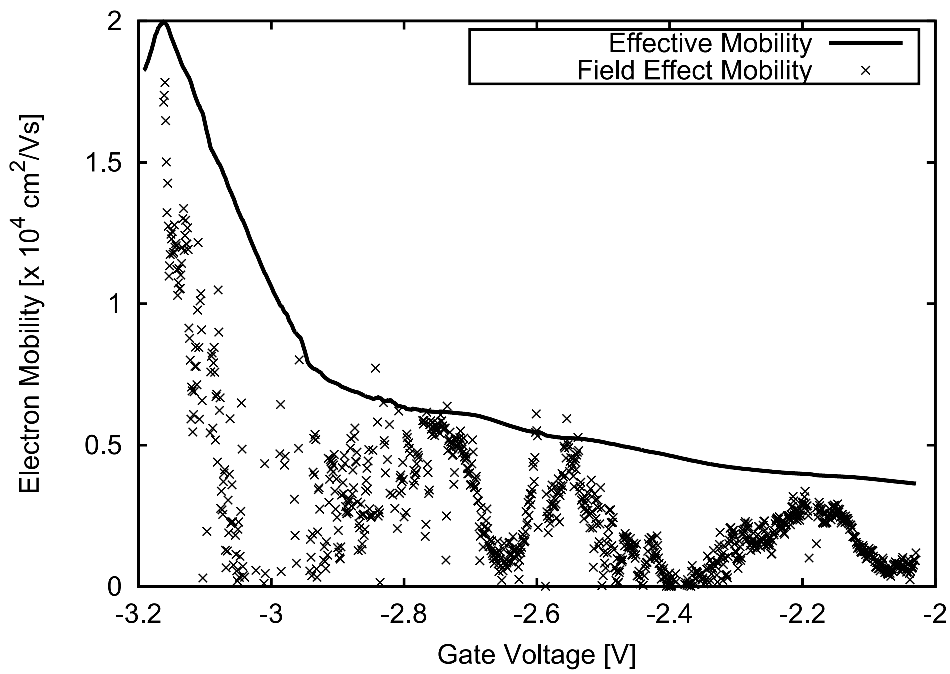

Figure 5.5: Field effect and effective mobility versus backgate voltage for Device 1 at T = 14 K.

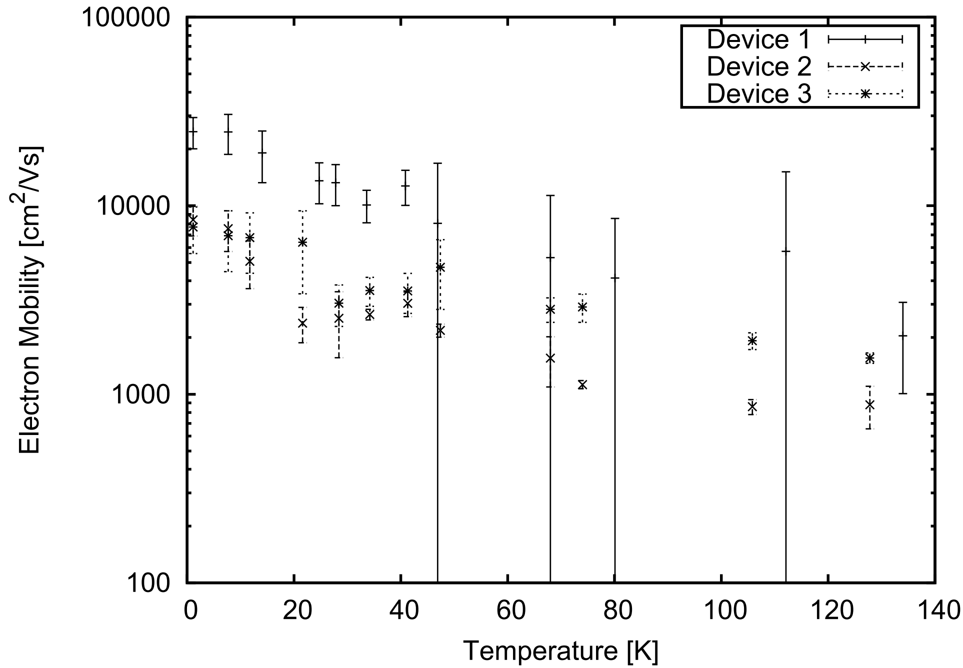

Figure 5.6: Peak effective electron mobility versus temperature for core-shell Devices 1-3.

In Figure 5.5 we see an increase in mobility near pinchoff versus a slower change at more positive voltages. The decrease in mobility is due to two factors: filling of higher subbands and increase in surface carrier density. At low temperatures, electrons occupy the lowest lying states, or subbands. As the temperature is increased, the electrons gain enough thermal energy to transition into higher bands. Inter-subband scattering as a result of this causes a reduction in mobility [148]. The cause for the reduction in mobility is the increase of scattering from surface states as a result of the increase in the temperature dependent carrier density near the surface.

μ_{eff} for core-shell and bare nanowires are shown in Figures 5.6 - 5.7. The unpassivated devices show a clear turndown at lower temperatures while the mobilities of core-shell nanowires increase monotonically. To analyze these results we must consider the types of scattering mechanisms present. Typically, mobility is dominated by two mechanisms in semiconductors: ionized impurity scattering where $\mu \propto T^{3/2}$ and

phonon scattering where $\mu \propto T^{-3/2}$. Phonon scattering is ruled out as the limiting mechanism in this case. Acoustic phonon scattering would permit higher mobilities (10^6 cm^{2}V$^{-1}s^{-1}$) at room temperature because acoustic phonon scattering is essentially elastic. In the long wavelength limit (small k) when $ka << 1$ the phonon velocity is $v = \omega/k$ (or $v = \omega a$) which is true for phonons near the zone centre. The longitudnal acoustic phonon angular frequency in InAs is 1.63×10^{13} rad/s (or 2.6GHz) [149], and the lattice constant is $a = 0.6058$ nm corresponding to a phonon velocity on the order of 10^4 m/s. Comparing this to the thermal electron velocity which is on the order of $10^5 - 10^6$ m/s at room temperature we can propose that any scattering that does occur, occurs elastically. If any reduction in mobility occurs from optical phonons which have higher frequencies, it will occur at higher temperatures [150]. Surface roughness and ionized impurity scattering are the most probable candidates for the turndown in mobility based on the large surface state density and high surface to volume ratio of the nanowire. But in Figure 5.7 we see what looks like the characteristic $\mu \propto T^{3/2} \rightarrow T^{-3/2}$ curve. We suggest that this effect has to do with the fact that higher radial subbands are occupied at higher temperatures, causing the electron wavefunctions to overlap with the surface states more strongly thereby increasing the scattering rate and lowering the mobility. Added to this is the effect discussed earlier where inter-subband scattering increases with temperature. The increased carrier concentration as a function of temperature is consistent with V_T data shown in Figure 5.4.

5.2.4 Conclusion

The absence of a turnover in mobility in core-shell nanowires is attributed to the fact that the density of ionized surface states are reduced by the shell. Photoluminescence studies on these nanowire devices will be carried out in the future. The range

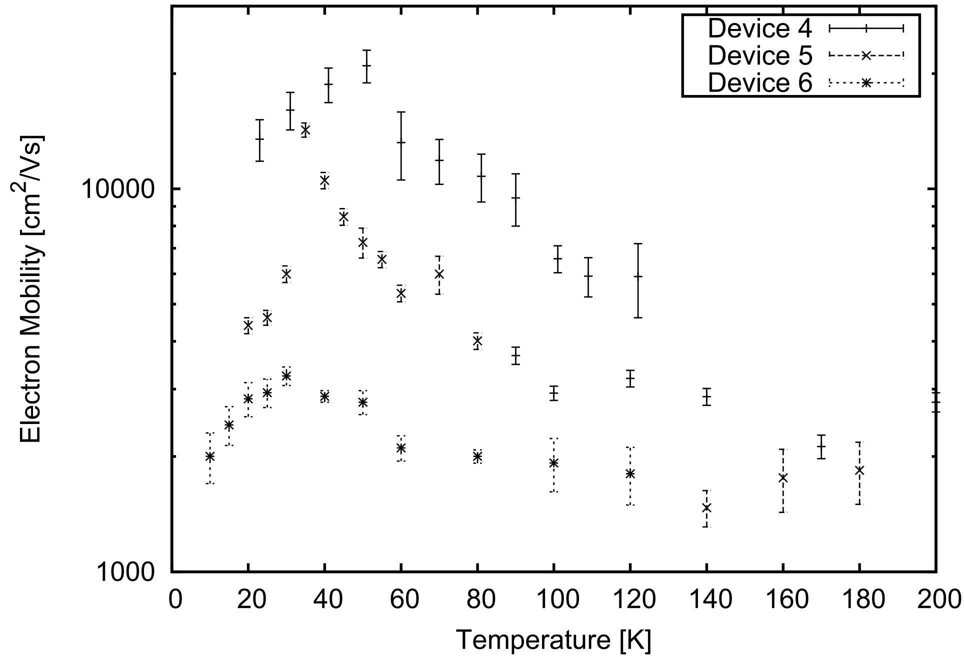

Figure 5.7: Peak effective electron mobility versus temperature for unpassivated Devices 4-6.

of the μPL system described in Chapter 2 is being extended to handle wavelengths up to 5μm allowing the study of InAs.

5.3 Ammonium Sulfide Passivation

5.3.1 Introduction

InP suffers from a different surface problem than InAs. The surface states pin the Fermi level near the middle of the band gap, severely bending the bands upward in n-type material or downward in p-type material. These states act as non-radiative recombination centres. A very common method for reducing this trap density is sulfur passivation with ammonium polysulfide. This process removes the native oxide layer and forms In-S bonds on the surface [151].

5.3.2 Experimental Details

The method used to grow InP nanowires in Chapter 3 was used in this work. However, the nanowires in this study were p-doped with Be. A Be effusion cell in the MBE was calibrated on 2D InP epilayers grown on InP (100) substrates. The nominal doping level was set at 5×10^{18} cm^{-3}. The nanowires were then characterized by SEM. Diameters varied from 60 to 100 nm with lengths ranging from 1.3 - 1.8 μm. The nanowires were removed from the growth substrate by sonication in acetone and dispersed onto a silicon substrate with a 300 nm thick thermally grown SiO_2 layer. μPL measurements were taken on the system described in Chapter 2. The polarization of the incident laser (HeNe, $\lambda = 632.8$ nm, $P = 320$ W cm^{-2}) was aligned with the long axis of the nanowire using two linear polarizers, a half waveplate, and a power meter. The first polarizer was a high extinction ratio Glan-Thompson polarizer which was used to generate a 100000:1 linear polarization. A second polarizer was placed at the sample surface, which was aligned along the long axis of the nanowire (the orientation of the nanowire was obtained relative to the silicon substrate by SEM). The power meter was placed under the second polarizer and the half wave plate was then placed between the two polarizers and the polarization was rotated until a maximum was observed on the power meter. This ensured that the polarization was aligned to the transmission axis of the second polarizer, and thus the nanowire.

The 0.55 m asymmetric Czerny-Turner spectrometer had a slit width of 0.018 mm and a holographic 1200 line/mm grating blazed at 750 nm. The detector used was the 1024x128 Si CCD cooled to 140K with liquid nitrogen. The 200 nm spectral range was divided up in to 7 segments, stitched together by the Synergy software [53] and integrated for 10 s each.

The passivation procedure was carried out by soaking the Si substrate with the dispersed nanowires in 5 ml of $(NH_4)_2S_x$ solution on a hotplate at 62°C. The passi-

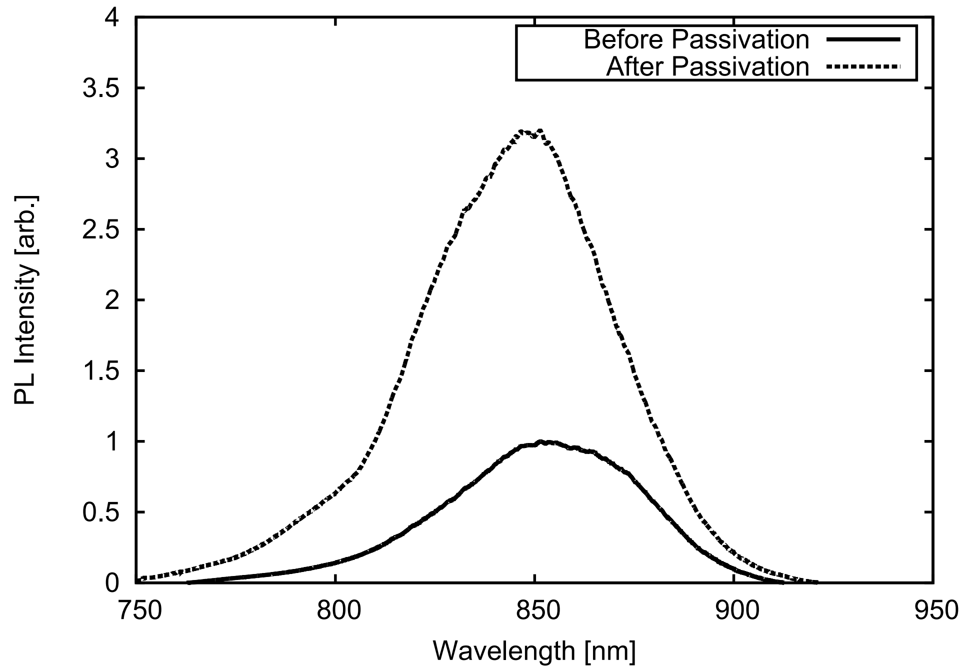

Figure 5.8: Representative room temperature μPL spectra showing pre- and post-passivation results on a single nanowire.

vation time was varied between 5 - 60 min. The starting chemical was a 20 wt % $(NH_4)_2S$ in H_2O obtained from Sigma-Aldrich. To this solution, elemental sulfur was added followed by dilution in either DI-H_2O, methanol, or iso-propyl alcohol. The procedure was carried out in a glove box with less than 1 ppm of O_2 and H_2O under illumination from a 30 W fibre optic illuminator. After the passivation procedure was complete, the samples were taken immediately to the PL system and measurements were taken immediately. By knowing the nanowire locations from SEM mapping, and by orienting the sample in the same way as it was for the pre-passivation measurements, the pre- and post-passivation PL measurements could be compared.

5.3.3 Results and Discussion

In Figure 5.8 representative PL spectra are shown highlighting the increase in PL intensity after passivation. The PL is dominated by a broad peak at 1.46 eV (850 nm). This is different from the bulk zincblende band-to-band emission at 1.35 eV. Quantum confinement effects are ruled out as the cause of the blue shift because the diameter of the nanowires is too large. This band-to-band emission is characteristic of wurtzite InP emission known to exist in the 1.4 - 1.5 eV range [70, 152–159]. The wurtzite structure was confirmed by TEM measurements. A small blue shift of approximately 30 meV is observed in Figure 5.8. This is attributed to the Franz-Keldysh effect, due to a reduction in the build in electric field imposed by the surface band bending [160].

The passivation procedure was optimized by combining different solvents with different concentrations of sulfur. The specifics of this process is beyond the scope of this work and can be found in Reference [38]. In summary, iso-propyl alcohol, 0.5M sulfur concentration, and 5 minutes were the optimal recipe resulting in an average of 24 X, and up to 40X improvement in PL intensity. One downfall of this very simple and effective process is that the stability of the passivation is reduced after a number of days when exposed to ambient air. The stability of the passivation can be preserved if the process is being used for Ohmic contact formation, where the passivation step is performed right before metal deposition [60] or if the nanowire is encapsulated in a polymer or dielectric film [161–163].

5.3.4 Conclusion

An optimized iso-propyl alcohol diluted, 0.5M $(NH_4)_2S_x$ solution was used to passivate p-InP nanowires for 5 minutes under broadband light illumination. This work combined with the model described in Tajik et al. [38] can be used in further studies to improve the performance of nanowire based optoelectronic devices.

Chapter 6

Conclusion and Future work

6.1 Thesis Summary

The VLS growth of InP and InAs nanowires by MBE in radial and axial geometries was examined. Axial segments of InAs were found to grow under two regimes. One dominated by diffusion from the nanowire sidewalls resulting in a growth rate that was inversely proportional to nanowire diameter. The other regime was observed when growing short segments of InAs, or quantum dots. The growth rate was linear in the nanowire diameter. By examining the adatom collection areas relative to the vapour-liquid-solid interface collection area, it was concluded that the growth species were provided by a purging of In from the Au particle. When segments were grown for intermediate times, a transition was seen between the two growth regimes. A method of core-shell nanowire passivation was developed and optimized to minimize strain relaxation. Theoretical calculations of strain and dislocation formation were carried out and compared to experiment. It was found that only AlInAs shells with Al alloy fractions of less than 0.20 were pseudomorphic with the InAs core. The effects of core-shell passivation on electron transport was examined by fabricating devices into FETs and determining their mobility as a function of temperature. It was found that mobility increases monotonically as temperature is reduced in core-shell devices while exhibiting a drastic decrease in unpassivated InAs nanwowires. This effect was

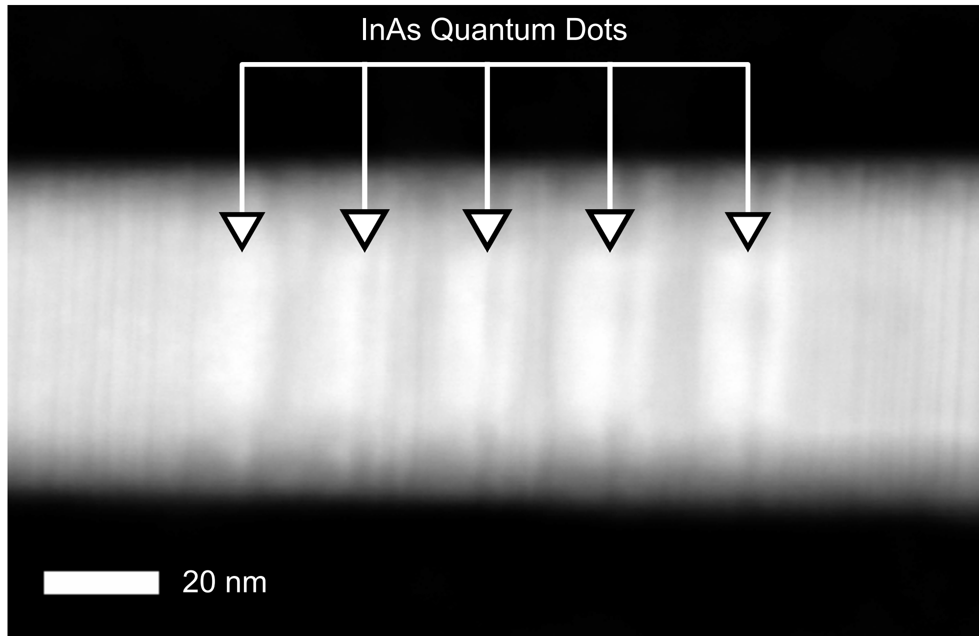

Figure 6.1: HAADF image showing 5 InAs quantum dots grown axially in an InP nanowire, surrounded by a AlInAs shell lattice matched to InP.

determined to be a result of the reduced ionized impurity scattering from surface states in the nanowire.

6.2 Future Work

The prime motivator for developing the core-shell growth method described in Chapter 4 was the lack of PL from InAs quantum dots, expected in the IR region between 1 and 2 μm. No PL was observed in our system using a diffraction grating optimized for the operating range of the InGaAs detector. It was hypothesized that the surface effects described in Chapter 5 were responsible for this so the core-shell method was proposed. The concepts investigated in Chapter 3 and 4 have been combined to grow InP/InAs quantum dot axial heterostructures with a AlInAs shell lattice matched to InP. A representative image of this structure is shown in Figure 6.1

This nanowire sample was grown at 0.5 μm/hr, a temperature of 420°C, and a V/III flux ratio of ~ 4. First an InP segment was grown, followed by a series of five InAs segments grown for 5 s each, separated by InP segments grown for 10 s. In this region, going from InP to InAs, the In supply was terminated, P_2 was switched for As_2 over a period of 25 s, and the In supply was reestablished. This sequence was reversed when going from InAs to InP. After the alternating InP/InAs section, another InP segment was grown axially. This was followed by a shell growth of $Al_{0.52}In_{0.48}As$ which is lattice matched to InP. This means that the strain issues encountered in the InAs-AlInAs(P) core-shell nanowires studied in Chapter 4 are mitigated along the majority of the nanowire. Some strain will occur at the interface between the AlInAs-InAs interface in the quantum dot region but the area is very small and the strain will likely be efficiently accommodated.

PL from these structures is still being sought. The present lack of PL could be attributed to a number of sources. The first issue is that the emission of the quantum dots is outside the detectable range of the PL system. This is currently any energy lower than 0.62 eV ($\lambda = 2\mu$m). The band gap of InAs is 0.418 eV at $T = 4.2$ K [138], so any quantized states in quantum dots are expected to be at an energy higher than 0.418 eV. Typically InAs nanowire quantum dots emit around 1 - 0.8 eV ($\lambda = 1200 - 1550$ nm) [164]. Efforts are currently underway to grow very short InAs segments. This will enable us to determine whether or not the dimensions of the current dots are too large, and thus not providing adequate confinement. Another contributor to the lack of PL could be a Type II band alignment between the core and shell. In this arrangement, rather than having the carriers localized in one layer, the electron and hole minima are located in different layers. This charge separation leads to reduced wavefunction overlap and thus a reduced radiative recombination rate. Calculations of single particle wavefunctions and energy levels taking into account

the strain developed in Chapter 4 to determine in which energy range the emission should lie are currently being carried out. This will provide information in choosing which mechanism is responsible for the lack of PL. Other shell materials are also being studied such as InGaAs. Al based materials often undergo significant oxidation when exposed to air, and the existence of traps in surface oxides in the AlInAs shell could be causing a reduction in PL. The first proposed growth is to start with the lattice matched AlInAs/InP structure described above and slowly transition Al for Ga over a period of 7.5 min. This will have the effect of maintaining the structural passivation but limiting the presence of Al on the outer surface of the nanowire.

Future work involves further characterization of the presence of charge noise on the surface of unpassivated InAs and core-shell InAs-AlInAs nanowire FETs. A preliminary study of this effect has been published on arXiv with our collaborators at IQC [165] and has been accepted for publication in the Journal of Applied Physics. Further study of the optical properties of InAs nanowires will be enabled by upgrades designed by the author to the μPL system described in this thesis. An InSb detector, capable of detecting wavelengths up to 5.5 μm is being integrated into the current spectrometer. An infinity corrected reflective microscope objective will provide 36X magnification and will have a wavelength operating range from 200 nm to 20 μ. The spectrometer is being outfitted with new CaF_2 entrance optics and a diffraction grating with high efficiency in the InAs region of interest (2 - 4.5 μm [84]). The system is also being outfitted with a photocurrent capability. Electrical feedthroughs carrying cabling to a custom designed printed circuit board have been designed and fabricated. A DC sweep is applied to the nanowire source-drain contacts. A mechanical chopper modulates the laser beam and provides a reference frequency to a lock-in-amplifier which measures the photocurrent. This capability will allow the characterization of nanowires as photoconductors.

References

[1] J. D. Eshelby, Journal of Applied Physics **24**, 176 (1953).

[2] F. C. Frank, Discussions of the Faraday Society **5**, 48 (1949).

[3] R. S. Wagner and W. C. Ellis, Applied Physics Letters **4**, 89 (1964).

[4] R. S. Wagner, W. C. Ellis, K. A. Jackson, and S. M. Arnold, Journal of Applied Physics **35**, 2993 (1964).

[5] E. Givargizov, Journal of Crystal Growth **31**, 20 (1975).

[6] M. Yazawa, M. Koguchi, A. Muto, M. Ozawa, and K. Hiruma, Applied Physics Letters **61**, 2051 (1992).

[7] M. Yazawa, M. Koguchi, and K. Hiruma, Applied Physics Letters **58**, 1080 (1991).

[8] M. Koguchi, H. Kakibayashi, M. Yazawa, K. Hiruma, and T. Katsuyama, Japanese Journal of Applied Physics **31**, 2061 (1992).

[9] I. Vurgaftman, J. R. Meyer, and L. R. Ram-Mohan, Journal of Applied Physics **89**, 5815 (2001).

[10] V. G. Dubrovskii and N. V. Sibirev, Physical Review E **70**, 031604 (2004).

[11] L. Schubert, P. Werner, N. D. Zakharov, G. Gerth, F. M. Kolb, L. Long, U. Gösele, and T. Y. Tan, Applied Physics Letters **84**, 4968 (2004).

[12] L. E. Jensen, M. T. Björk, S. Jeppesen, A. I. Persson, B. J. Ohlsson, and L. Samuelson, Nano Letters **4**, 1961 (2004).

[13] W. Seifert, M. Borgström, K. Deppert, K. A. Dick, J. Johansson, M. W. Larsson, T. Mårtensson, N. Sköld, C. P. T. Svensson, B. A. Wacaser, L. R. Wallenberg, and L. Samuelson, Journal of Crystal Growth **272**, 211 (2004), The Twelfth International Conference on Metalorganic Vapor Phase Epitaxy.

[14] J. Johansson, C. P. T. Svensson, T. Mårtensson, L. Samuelson, and W. Seifert, The Journal of Physical Chemistry B **109**, 13567 (2005).

[15] V. G. Dubrovskii, N. V. Sibirev, G. E. Cirlin, J. C. Harmand, and V. M. Ustinov, Physical Review E **73**, 021603 (2006).

[16] F. Glas, J.-C. Harmand, and G. Patriarche, Physical Review Letters **99**, 146101 (2007).

[17] P. Krogstrup, S. Curiotto, E. Johnson, M. Aagesen, J. Nygård, and D. Chatain, Physical Review Letters **106**, 125505 (2011).

[18] B. Mandl, J. Stangl, T. Mårtensson, A. Mikkelsen, J. Eriksson, L. S. Karlsson, G. Bauer, L. Samuelson, and W. Seifert, Nano Letters **6**, 1817 (2006).

[19] C. B. Collins, R. O. Carlson, and C. J. Gallagher, Phys. Rev. **105**, 1168 (1957).

[20] J. D. Plummer, M. D. Deal, and P. B. Griffin, *Silicon VLSI Technology - Fundamentals, Practice and Modeling*, Prentice Hall Inc. (2000).

[21] ITRS, *International technology roadmap for semiconductors*, Technical report, Sematech (2011).

[22] J. Baugh, J. S. Fung, J. Mracek, and R. R. LaPierre, Nanotechnology **21**, 134018 (2010).

[23] J. A. Czaban, D. A. Thompson, and R. R. LaPierre, Nano Letters **9**, 148 (2009).

[24] W. Wei, X.-Y. Bao, C. Soci, Y. Ding, Z.-L. Wang, and D. Wang, Nano Letters **9**, 2926 (2009).

[25] D. Loss and D. P. DiVincenzo, Phys. Rev. A **57**, 120 (1998).

[26] P. Kok, W. J. Munro, K. Nemoto, T. C. Ralph, J. P. Dowling, and G. J. Milburn, Rev. Mod. Phys. **79**, 135 (2007).

[27] A. J. Berkley, H. Xu, R. C. Ramos, M. A. Gubrud, F. W. Strauch, P. R. Johnson, J. R. Anderson, A. J. Dragt, C. J. Lobb, and F. C. Wellstood, Science **300**, 1548 (2003).

[28] S. Nadj-Perge, S. M. Frolov, E. P. A. M. Bakkers, and L. P. Kouwenhoven, Nature **468**, 1084 (2010).

[29] J. Claudon, J. Bleuse, N. S. Malik, M. Bazin, P. Jaffrennou, N. Gregersen, C. Sauvan, P. Lalanne, and J.-M. Gerard, Nature Photonics **4**, 174 (2010).

[30] H. A. Nilsson, P. Samuelsson, P. Caroff, and H. Q. Xu, Nano Letters **12**, 228 (2012).

[31] V. Mourik, K. Zuo, S. M. Frolov, S. R. Plissard, E. P. A. M. Bakkers, and L. P. Kouwenhoven, Science **336**, 1003 (2012).

[32] C. Nayak, S. H. Simon, A. Stern, M. Freedman, and S. Das Sarma, Rev. Mod. Phys. **80**, 1083 (2008).

[33] A. Kandala, T. Betti, and A. Fontcuberta i Morral, Physica Status Solidi A **206**, 173 (2009).

[34] C. M. Haapamaki and R. R. LaPierre, Nanotechnology **22**, 335602 (2011).

[35] C. M. Haapamaki, J. Baugh, and R. R. LaPierre, Journal of Crystal Growth **345**, 11 (2012).

[36] C. M. Haapamaki, J. Baugh, and R. R. LaPierre, *Critical shell thickness for InAs-Al_xIn_{1-x}As(P) core-shell nanowires* (2012), arXiv:1209.4321 [cond-mat.mtrl-sci].

[37] G. W. Holloway, Y. Song, C. M. Haapamaki, R. R. LaPierre, and J. Baugh, *Electron Transport in InAs-InAlAs Core-Shell Nanowires* (2012), arXiv:1209.2767 [cond-mat.mes-hall].

[38] N. Tajik, C. M. Haapamaki, and R. R. LaPierre, Nanotechnology **23**, 315703 (2012).

[39] A. Cho and J. Arthur, Progress in Solid State Chemistry **10**, 157 (1975).

[40] M. Ohring, *Materials Science of Thin Films - Deposition and Structure 2nd Ed.*, Academic Press (2002).

[41] *SVT Associates Inc.*, `http://www.svta.com/`.

[42] M. B. Panish, Journal of the Electrochemical Society **127**, 2729 (1980).

[43] *AXT Inc.*, `http://www.axt.com`.

[44] F. L. Pedrotti and L. S. Pedrotti, *Introduction to Optics - Second Editions*, Prentice Hall Inc. (1993).

[45] D. B. Williams and C. B. Carter, *Transmission Electron Microscopy - A Textbook for Materials Science*, Springer (2009).

[46] R. F. Egerton, *Physical Principles of Electron Microscopy*, Springer (2005).

[47] J. Johansson, L. S. Karlsson, C. Patrik T. Svensson, T. Mårtensson, B. A. Wacaser, K. Deppert, L. Samuelson, and W. Seifert, Nature Materials **5**, 574 (2006).

[48] *Newport Corporation*, `www.newport.com`.

[49] *CVI Melles Griot*, `https://www.cvimellesgriot.com/`.

[50] *Thorlabs Inc.*, `www.thorlabs.com`.

[51] J. Wang, M. S. Gudiksen, X. Duan, Y. Cui, and C. M. Lieber, Science **293**, 1455 (2001).

[52] C. Chen, S. Shehata, C. Fradin, R. R. LaPierre, C. Couteau, and G. Weihs, Nano Letters **7**, 2584 (2007).

[53] *Horiba Jobin Yvon*, http://www.horiba.com/scientific/.

[54] *Electro-Optical Systems*, http://www.eosystems.com/.

[55] *Stanford Research Systems*, www.thinksrs.com.

[56] *Janis Research Company LLC*, www.janis.com.

[57] *Lakeshore Cryotronics Inc.*, www.lakeshore.com.

[58] *Microchem Corporation*, http://microchem.com/Prod-PMMA.htm.

[59] M. Tong, K. Nummila, A. A. Ketterson, I. Adesida, L. Aina, and M. Mattingly, Journal of the Electrochemical Society **139**, L91 (1992).

[60] D. B. Suyatin, C. Thelander, M. T. Björk, I. Maximov, and L. Samuelson, Nanotechnology **18**, 105307 (2007).

[61] V. Dubrovskii, G. Cirlin, and V. Ustinov, Semiconductors **43**, 1539 (2009).

[62] K. Dick, K. Deppert, L. Karlsson, L. Wallenberg, L. Samuelson, and W. Seifert, Advanced Functional Materials **15**, 1603 (2005).

[63] K. A. Dick, S. Kodambaka, M. C. Reuter, K. Deppert, L. Samuelson, W. Seifert, L. R. Wallenberg, and F. M. Ross, Nano Letters **7**, 1817 (2007).

[64] S. Bhunia, T. Kawamura, S. Fujikawa, and Y. Watanabe, Physica E **24**, 138 (2004).

[65] S. Bhunia, T. Kawamura, S. Fujikawa, H. Nakashima, K. Furukawa, K. Torimitsu, and Y. Watanabe, Thin Solid Films **464-465**, 244 (2004).

[66] S. Bhunia, T. Kawamura, S. Fujikawa, K. Tokushima, and Y. Watanabe, Physica E **21**, 583 (2004).

[67] L. E. Fröberg, W. Seifert, and J. Johansson, Physical Review B **76**, 153401 (2007).

[68] L. E. Fröberg, B. A. Wacaser, J. B. Wagner, S. Jeppesen, B. J. Ohlsson, K. Deppert, and L. Samuelson, Nano Letters **8**, 3815 (2008).

[69] V. G. Dubrovskii, N. V. Sibirev, G. E. Cirlin, I. P. Soshnikov, W. H. Chen, R. Larde, E. Cadel, P. Pareige, T. Xu, B. Grandidier, J.-P. Nys, D. Stievenard, M. Moewe, L. C. Chuang, and C. Chang-Hasnain, Physical Review B **79**, 205316 (2009).

[70] S. Paiman, Q. Gao, H. H. Tan, C. Jagadish, K. Pemasiri, M. Montazeri, H. E. Jackson, L. M. Smith, J. M. Yarrison-Rice, X. Zhang, and J. Zou, Nanotechnology **20**, 225606 (2009).

[71] S. Paiman, Q. Gao, H. J. Joyce, Y. Kim, H. H. Tan, C. Jagadish, X. Zhang, Y. Guo, and J. Zou, Journal of Physics D: Applied Physics **43**, 445402 (2010).

[72] M. Tchernycheva, L. Travers, G. Patriarche, F. Glas, J.-C. Harmand, G. E. Cirlin, and V. G. Dubrovskii, Journal of Applied Physics **102**, 094313 (2007).

[73] F. Glas, J.-C. Harmand, and G. Patriarche, Physical Review Letters **104**, 135501 (2010).

[74] J.-C. Harmand, F. Glas, and G. Patriarche, Physical Review B **81**, 235436 (2010).

[75] S. A. Fortuna and X. Li, Semiconductor Science and Technology **25**, 024005 (2010).

[76] M. C. Plante and R. R. LaPierre, Nanotechnology **19**, 495603 (2008).

[77] C. Colombo, D. Spirkoska, M. Frimmer, G. Abstreiter, and A. Fontcuberta i Morral, Physical Review B **77**, 155326 (2008).

[78] L. Geelhaar, C. Chèze, W. M. Weber, R. Averbeck, H. Riechert, T. Kehagias, P. Komninou, G. P. Dimitrakopulos, and T. Karakostas, Applied Physics Letters **91**, 093113 (2007).

[79] H. J. Joyce, Q. Gao, H. H. Tan, C. Jagadish, Y. Kim, M. A. Fickenscher, S. Perera, T. B. Hoang, L. M. Smith, H. E. Jackson, J. M. Yarrison-Rice, X. Zhang, and J. Zou, Advanced Functional Materials **18**, 3794 (2008).

[80] V. G. Dubrovskii, G. E. Cirlin, I. P. Soshnikov, A. A. Tonkikh, N. V. Sibirev, Y. B. Samsonenko, and V. M. Ustinov, Physical Review B **71**, 205325 (2005).

[81] M. Plante and R. LaPierre, Journal of Crystal Growth **286**, 394 (2006).

[82] L. Ouattara, A. Mikkelsen, N. Sköld, J. Eriksson, T. Knaapen, E. Ćavar, W. Seifert, L. Samuelson, and E. Lundgren, Nano Letters **7**, 2859 (2007).

[83] P. Krogstrup, J. Yamasaki, C. B. Sørensen, E. Johnson, J. B. Wagner, R. Pennington, M. Aagesen, N. Tanaka, and J. Nygård, Nano Letters **9**, 3689 (2009).

[84] M. H. Sun, H. J. Joyce, Q. Gao, H. H. Tan, C. Jagadish, and C. Z. Ning, Nano Letters **12**, 3378 (2012).

[85] S. A. Dayeh, C. Soci, P. K. L. Yu, E. T. Yu, and D. Wang, Journal of Vacuum Science and Technology B **25**, 1432 (2007).

[86] A. R. Clawson, Materials Science and Engineering: R: Reports **31**, 1 (2001).

[87] X. Jiang, Q. Xiong, S. Nam, F. Qian, Y. Li, and C. M. Lieber, Nano Letters **7**, 3214 (2007).

[88] A. C. Ford, J. C. Ho, Y.-L. Chueh, Y.-C. Tseng, Z. Fan, J. Guo, J. Bokor, and A. Javey, Nano Letters **9**, 360 (2009).

[89] J. W. W. van Tilburg, R. E. Algra, W. G. G. Immink, M. Verheijen, E. P. A. M. Bakkers, and L. P. Kouwenhoven, Semiconductor Science and Technology **25**, 024011 (2010).

[90] Z. Zanolli, M.-E. Pistol, L. E. Fröberg, and L. Samuelson, Journal of Physics: Condensed Matter **19**, 295219 (2007).

[91] M. T. Borgstrom, V. Zwiller, E. Mller, and A. Imamoglu, Nano Letters **5**, 1439 (2005).

[92] J.-C. Harmand, F. Glas, G. Patriarche, L. Largeau, M. Tchernycheva, C. Sartel, L. Liu, and F. Jabeen, in *Advances in III-V Semiconductor Nanowires and Nanodevices*, Bentham Science (2011).

[93] P. Mohan, J. Motohisa, and T. Fukui, Applied Physics Letters **88**, 133105 (2006).

[94] Y. Masumoto, Y. Hirata, P. Mohan, J. Motohisa, and T. Fukui, Applied Physics Letters **98**, 211902 (2011).

[95] H.-Y. Li, O. Wunnicke, M. T. Borgström, W. G. G. Immink, M. H. M. van Weert, M. A. Verheijen, and E. P. A. M. Bakkers, Nano Letters **7**, 1144 (2007).

[96] M. Tchernycheva, G. E. Cirlin, G. Patriarche, L. Travers, V. Zwiller, U. Perinetti, and J.-C. Harmand, Nano Letters **7**, 1500 (2007).

[97] Y. Kim, H. J. Joyce, Q. Gao, H. H. Tan, C. Jagadish, M. Paladugu, J. Zou, and A. A. Suvorova, Nano Letters **6**, 599 (2006).

[98] K. L. Kavanagh, J. Salfi, I. Savelyev, M. Blumin, and H. E. Ruda, Applied Physics Letters **98**, 152103 (2011).

[99] A. C. E. Chia, M. Tirado, Y. Li, S. Zhao, Z. Mi, D. Comedi, and R. R. LaPierre, Journal of Applied Physics **111**, 094319 (2012).

[100] J. W. Matthews, Journal of Vacuum Science and Technology **12**, 126 (1975).

[101] M. Y. Gutkin, I. A. Ovid'ko, and A. G. Sheinerman, Journal of Physics: Condensed Matter **12**, 5391 (2000).

[102] J. Colin and J. Grilh, Philosophical Magazine Letters **82**, 125 (2002).

[103] A. L. Kolesnikova and A. E. Romanov, Philosophical Magazine Letters **84**, 501 (2004).

[104] I. A. Ovid'ko and A. G. Sheinerman, Philosophical Magazine **84**, 2103 (2004).

[105] E. Ertekin, P. A. Greaney, D. C. Chrzan, and T. D. Sands, Journal of Applied Physics **97**, 114325 (2005).

[106] K. E. Aifantis, A. L. Kolesnikova, and A. E. Romanov, Philosophical Magazine **87**, 4731 (2007).

[107] Q. Fang, H. Song, and Y. Liu, Physica B: Condensed Matter **404**, 1897 (2009).

[108] T. E. Trammell, X. Zhang, Y. Li, L.-Q. Chen, and E. C. Dickey, Journal of Crystal Growth **310**, 3084 (2008).

[109] S. Raychaudhuri and E. T. Yu, Journal of Applied Physics **99**, 114308 (2006).

[110] G. E. Cirlin, V. G. Dubrovskii, I. P. Soshnikov, N. V. Sibirev, Y. B. Samsonenko, A. D. Bouravleuv, J. C. Harmand, and F. Glas, Physica Status Solidi Rapid Research Letters **3**, 112 (2009).

[111] M. C. Plante and R. R. LaPierre, Applied Physics Letters **105**, 114304 (2009).

[112] C. Chen, M. Plante, C. Fradin, and R. R. LaPierre, Journal of Materials Research **21**, 2801 (2006).

[113] G. Kästner and U. Gösele, Philosophical Magazine **84**, 3803 (2004).

[114] M. Y. Gutkin, K. V. Kuzmin, and A. G. Sheinerman, Physica Status Solidi B **248**, 1651 (2011).

[115] M. Paladugu, J. Zou, Y.-N. Guo, X. Zhang, H. J. Joyce, Q. Gao, H. H. Tan, C. Jagadish, and Y. Kim, Applied Physics Letters **93**, 201908 (2008).

[116] M. Paladugu, J. Zou, Y. Guo, X. Zhang, H. Joyce, Q. Gao, H. Tan, C. Jagadish, and Y. Kim, Nanoscale Research Letters **4**, 846 (2009).

[117] M. Keplinger, T. Mrtensson, J. Stangl, E. Wintersberger, B. Mandl, D. Kriegner, V. Holy, G. Bauer, K. Deppert, and L. Samuelson, Nano Letters **9**, 1877 (2009).

[118] K. A. Dick, P. Caroff, J. Bolinsson, M. E. Messing, J. Johansson, K. Deppert, L. R. Wallenberg, and L. Samuelson, Semiconductor Science and Technology **25**, 024009 (2010).

[119] M. Plante and R. LaPierre, Journal of Crystal Growth **310**, 356 (2008).

[120] R. Popovitz-Biro, A. Kretinin, P. Von Huth, and H. Shtrikman, Crystal Growth and Design **11**, 3858 (2011).

[121] A. Fakhr, Y. M. Haddara, and R. R. LaPierre, Nanotechnology **21**, 165601 (2010).

[122] C. Chen, N. B. C. Couteau, C. Fradin, G. Weihs, and R. R. LaPierre, Nano Letters **8**, 495 (2008).

[123] H. Okamoto, Journal of Phase Equilibria and Diffusion **25**, 197 (2004).

[124] H. Okamoto, Journal of Phase Equilibria and Diffusion **26**, 391 (2005).

[125] N. Grandjean and J. Massies, Physical Review B **53**, R13231 (1996).

[126] E. Tournié, N. Grandjean, A. Trampert, J. Massies, and K. Ploog, Journal of Crystal Growth **150**, 460 (1995).

[127] B. Vasallo, N. Wichmann, S. Bollaert, Y. Roelens, A. Cappy, T. Gonzalez, D. Pardo, and J. Mateos, IEEE Transactions on Electron Devices **54**, 2815 (2007).

[128] M.-E. Pistol and C. E. Pryor, Physical Review B **78**, 115319 (2008).

[129] A. De and C. E. Pryor, Physical Review B **81**, 155210 (2010).

[130] R. M. Martin, Physical Review B **6**, 4546 (1972).

[131] R. W. G. Wykcoff, *Crystal Structures*, Interscience, New York (1963).

[132] P. Lawaetz, Phys. Rev. B **5**, 4039 (1972).

[133] J. C. Phillips, Reviews of Modern Physics **42**, 317 (1970).

[134] J. A. Van Vechten, Physical Review B **3**, 562 (1971).

[135] L. Pauling, *The Nature Of The Chemical Bond*, Cornell University Press, Ithaca NY (1960).

[136] C. F. Cline, H. L. Dunegan, and G. W. Henderson, Journal of Applied Physics **38**, 1944 (1967).

[137] J. F. Nye, *Physical Properties of Crystals - Their Representation by Tensors and Matrices*, Oxford University Press, London (1985).

[138] O. Madelung, *Semiconductors Data Handbook*, Springer (2004).

[139] S. Timoshenko and J. N. Goodier, *Theory of Elasticity*, McGraw Hill, New York (1951).

[140] C. M. Warwick and T. W. Clyne, Journal of Materials Science **26**, 3817 (1991).

[141] Equation (9c) in the paper by Trammell [108] is incorrect. The final term should read as shown above in Equation (4.36) as verified through discussions with one of the authors of the original paper, Elizabeth Dickey.

[142] Y. Chou and J. Eshelby, Journal of the Mechanics and Physics of Solids **10**, 27 (1962).

[143] J. van der Merwe, Journal of Electronic Materials **20**, 793 (1991).

[144] M. Lowe, T. Veal, C. McConville, G. Bell, S. Tsukamoto, and N. Koguchi, Surface Science **523**, 179 (2003).

[145] M. D. Schroer and J. R. Petta, Nano Letters **10**, 1618 (2010).

[146] A. C. Bleszynski, F. A. Zwanenburg, R. M. Westervelt, A. L. Roest, E. P. A. M. Bakkers, and L. P. Kouwenhoven, Nano Letters **7**, 2559 (2007).

[147] O. Wunnicke, Applied Physics Letters **89**, 083102 (2006).

[148] K. K. Das and A. Mizel, Journal of Physics: Condensed Matter **17**, 6675 (2005).

[149] D. N. Talwar and B. K. Agrawal, Physica Status Solidi B **63**, 441 (1974).

[150] O. Madelung, *Physics of III-V Compounds*, John Wiley and Sons (1964).

[151] V. Bessolov and M. Lebedev, Semiconductors **32**, 1141 (1998).

[152] A. J. Lohn, T. Onishi, and N. P. Kobayashi, Nanotechnology **21**, 355702 (2010).

[153] J. Bao, D. C. Bell, F. Capasso, J. B. Wagner, T. Mårtensson, J. Trägårdh, and L. Samuelson, Nano Letters **8**, 836 (2008).

[154] A. Mishra, L. V. Titova, T. B. Hoang, H. E. Jackson, L. M. Smith, J. M. Yarrison-Rice, Y. Kim, H. J. Joyce, Q. Gao, H. H. Tan, and C. Jagadish, Applied Physics Letters **91**, 263104 (2007).

[155] P. J. Reece, S. Paiman, O. Abdul-Nabi, Q. Gao, M. Gal, H. H. Tan, and C. Jagadish, Applied Physics Letters **95**, 101109 (2009).

[156] M. Mattila, T. Hakkarainen, M. Mulot, and H. Lipsanen, Nanotechnology **17**, 1580 (2006).

[157] K. Pemasiri, M. Montazeri, R. Gass, L. M. Smith, H. E. Jackson, J. Yarrison-Rice, S. Paiman, Q. Gao, H. H. Tan, C. Jagadish, X. Zhang, and J. Zou, Nano Letters **9**, 648 (2009).

[158] K. Ikejiri, Y. Kitauchi, K. Tomioka, J. Motohisa, and T. Fukui, Nano Letters **11**, 4314 (2011).

[159] J. Wallentin, K. Mergenthaler, M. Ek, L. R. Wallenberg, L. Samuelson, K. Deppert, M.-E. Pistol, and M. T. Borgstrom, Nano Letters **11**, 2286 (2011).

[160] M. H. M. van Weert, O. Wunnicke, A. L. Roest, T. J. Eijkemans, A. Y. Silov, J. E. M. Haverkort, G. W. 't Hooft, and E. P. A. M. Bakkers, Applied Physics Letters **88**, 043109 (2006).

[161] N. Tajik, A. C. E. Chia, and R. R. LaPierre, Applied Physics Letters **100**, 203122 (2012).

[162] G. Mariani, P.-S. Wong, A. M. Katzenmeyer, F. Leonard, J. Shapiro, and D. L. Huffaker, Nano Letters **11**, 2490 (2011).

[163] Z. Jin, W. Prost, S. Neumann, and F. J. Tegude, Journal of Vacuum Science & Technology B: Microelectronics and Nanometer Structures **22**, 1060 (2004).

[164] R. Singh and G. Bester, Phys. Rev. Lett. **103**, 063601 (2009).

[165] G. W. Holloway, Y. Song, C. M. Haapamaki, R. R. LaPierre, and J. Baugh, *Trapped charge dynamics in InAs nanowires* (2012), arXiv:1209.3237 [cond-mat.mes-hall].

[166] *Maxima, a Computer Algebra System. Version 5.25.1*, `http://maxima.sourceforge.net/`.

[167] *GNU Octave, Version 3.6.1*, `http://www.octave.org/`.

Appendix A

Strain Model Supplementary Information

A.1 Derivation of Displacement Coefficients

The system of four algebraic equations derived from the boundary conditions solved in Chapter 4 are sought to determine the coefficients in the displacement solutions in Equation (4.39) and (4.40). They were omitted in the chapter due to length, but they are derived here. The system is solved using MAXIMA in Section A.2

(i) Equation (4.41), continuity of displacement across the core-shell interface:

$$u_r^c(r = R_c) - u_r^s(r = R_c) = 0$$
$$\alpha^c R_c - \alpha^s R_c + \gamma^s \frac{1}{R_c} = 0$$

(ii) Equation (4.42), continuity of stress across the core-shell interface. Let $\Gamma = a_r^c/a_r^s$ and $\Theta = a_z^c/a_z^s$.

$$\sigma_r^c(r = R_c) - \sigma_r^s(r = R_c) = 0$$
$$c_{11}^c \mathrm{e}_r^c + c_{12}^c \mathrm{e}_\theta^c + c_{12}^c \mathrm{e}_z^c - c_{11}^s \mathrm{e}_r^s + c_{12}^s \mathrm{e}_\theta^s + c_{12}^s \mathrm{e}_z^s = 0$$
$$c_{11}^c \frac{\partial u_r^c}{\partial r} + c_{12}^c \frac{u_r^c}{r} + c_{12}^c \frac{\partial u_z^c}{\partial z} - c_{11}^s \Gamma \left(\frac{\partial u_r^s}{\partial r} - m_r \right) + c_{12}^s \Gamma \left(\frac{\partial u_r^s}{\partial r} - m_r \right) + \dots$$
$$c_{12}^s \Theta \left(\frac{\partial u_z^c}{\partial z} - m_z \right) = 0$$
$$c_{11}^c \alpha^c + c_{12}^c \alpha^c + c_{12}^c \gamma^c - c_{11}^s \Gamma \left(\alpha^s - \frac{\beta^s}{R_c^2} - m_r \right) + c_{12}^s \Gamma \left(\alpha^s + \frac{\beta^s}{R_c^2} - m_r \right) + \dots$$
$$c_{12}^s \Theta \left(\gamma^c - m_z \right) = 0$$
$$\alpha^c \left(c_{11}^c - c_{12}^c \right) - \alpha^s \left(c_{11}^s \Gamma + c_{12}^s \Gamma \right) + \beta^s \left(\frac{c_{11}^s \Gamma - c_{12}^s \Gamma}{R_c^2} \right) + \gamma^c \left(c_{12}^c - c_{12}^s \Theta \right) + \dots$$
$$m_r \left(c_{11}^s \Gamma + c_{12}^s \Gamma \right) + m_z c_{12}^s \Theta = 0$$

(iii) Equation (4.43), lack of surface forces in the z-direction.

$$\int_0^{R_c}\int_0^{2\pi}\sigma_z^c r\,dr d\theta+\int_{R_c}^{R}\int_0^{2\pi}\sigma_z^s r\,dr d\theta=0$$
$$2\pi\int_0^{R_c}\sigma_z^c r\,dr+2\pi\int_{R_c}^{R}\sigma_z^s r\,dr=0$$
$$\int_0^{R_c}\left(c_{12}^c \mathrm{e}_r^c+c_{12}^c\mathrm{e}_\theta^c+c_{11}^c\mathrm{e}_z^c\right)r\,dr+\int_{R_c}^{R}\left(c_{12}^s\mathrm{e}_r^s+c_{12}^s\mathrm{e}_\theta^s+c_{11}^s\mathrm{e}_z^s\right)r\,dr=0$$
$$\int_0^{R_c}\left(c_{12}^c\frac{\partial u_r^c}{\partial r}+c_{12}^c\frac{u_r^c}{r}+c_{11}^c\frac{\partial u_z^c}{\partial z}\right)r\,dr+\int_{R_c}^{R}\left\{c_{12}^s\Gamma\left(\frac{\partial u_r^s}{\partial r}-m_r\right)+\dots\right.$$
$$\left.c_{12}^s\Gamma\left(\frac{\partial u_r^s}{\partial r}-m_r\right)+c_{11}^s\Theta\left(\frac{\partial u_z^s}{\partial z}-m_z\right)\right\}r\,dr=0$$
$$\int_0^{R_c}\left(c_{12}^c\alpha^c+c_{12}^c\alpha^c+c_{11}^c\phi^c\right)r\,dr+\int_{R_c}^{R}\left\{c_{12}^s\Gamma\left(\alpha^s-\frac{\beta^s}{r^2}-m_r\right)+\dots\right.$$
$$\left.c_{12}^s\Gamma\left(\alpha^s+\frac{\beta^s}{r^2}-m_r\right)+c_{11}^s\Theta\left(\gamma^c-m_z\right)\right\}r\,dr=0$$
$$\left(2c_{12}^c\alpha^c+c_{11}^c\gamma^c\right)\frac{R_c^2}{2}+\left\{2c_{12}^s\Gamma\left(\alpha^s-m_r\right)+c_{11}^s\Theta\left(\gamma^c-m_z\right)\right\}\frac{R^2-R_c^2}{2}=0$$
$$\alpha^c c_{12}^c R_c^2+\alpha^s\left\{c_{12}^s\Gamma\left(R^2-R_c^2\right)\right\}+\gamma^c\left\{\frac{c_{11}^c R_c^2}{2}+c_{11}^s\Theta\frac{R^2-R_c^2}{2}\right\}-\dots$$
$$m_r\left\{c_{12}^s\Gamma\left(R^2-R_c^2\right)\right\}-m_z\left(c_{11}^s\Theta\frac{R^2-R_c^2}{2}\right)=0$$

(iv) Equation (4.44), lack of surface stress.

$$\sigma_r^s(r=R)=0$$
$$c_{11}^s\mathrm{e}_r^s+c_{12}^s\mathrm{e}_\theta^s+c_{12}^s\mathrm{e}_z^s=0$$
$$c_{11}^s\Gamma\left(\frac{\partial u_r^s}{\partial r}-m_r\right)+c_{12}^s\Gamma\left(\frac{u_r^s}{r}-m_r\right)+c_{12}^s\Theta\left(\frac{\partial u_r^z}{\partial z}-m_z\right)=0$$
$$c_{11}^s\Gamma\left(\alpha^s-\frac{\beta^s}{R^2}-m_r\right)+c_{12}^s\Gamma\left(\alpha^s+\frac{\beta^s}{R^2}-m_r\right)+c_{12}^s\Theta\left(\gamma^c-m_z\right)=0$$
$$\alpha^s\left(c_{11}^s\Gamma+c_{12}^s\Gamma\right)+\beta^s\left(\frac{c_{12}^s\Gamma}{R^2}-\frac{c_{11}^s\Gamma}{R^2}\right)+\gamma^c c_{12}^s\Theta-m_r\left(c_{11}^s\Gamma+c_{12}\Gamma\right)-\dots$$
$$m_z c_{12}^s\Theta=0$$

To summarize, the four equations developed above are:

$$\alpha^c R_c - \alpha^s R_c + \gamma^s \frac{1}{R_c} = 0 \tag{A.1}$$

$$\begin{aligned}&\alpha^c \left(c_{11}^c - c_{12}^c\right) - \alpha^s \left(c_{11}^s \Gamma + c_{12}^s \Gamma\right) + \beta^s \left(\frac{c_{11}^s \Gamma - c_{12}^s \Gamma}{R_c^2}\right) + \gamma^c \left(c_{12}^c - c_{12}^s \Theta\right) + \dots \\ &m_r \left(c_{11}^s \Gamma + c_{12}^s \Gamma\right) + m_z c_{12}^s \Theta = 0\end{aligned} \tag{A.2}$$

$$\begin{aligned}&\alpha^c c_{12}^c R_c^2 + \alpha^s \left\{c_{12}^s \Gamma \left(R^2 - R_c^2\right)\right\} + \gamma^c \left\{\frac{c_{11}^c R_c^2}{2} + c_{11}^s \Theta \frac{R^2 - R_c^2}{2}\right\} - \dots \\ &m_r \left\{c_{12}^s \Gamma \left(R^2 - R_c^2\right)\right\} - m_z \left(c_{11}^s \Theta \frac{R^2 - R_c^2}{2}\right) = 0\end{aligned} \tag{A.3}$$

$$\begin{aligned}&\alpha^s \left(c_{11}^s \Gamma + c_{12}^s \Gamma\right) + \beta^s \left(\frac{c_{12}^s \Gamma}{R^2} - \frac{c_{11}^s \Gamma}{R^2}\right) + \gamma^c c_{12}^s \Theta - m_r \left(c_{11}^s \Gamma + c_{12} \Gamma\right) - \dots \\ &m_z c_{12}^s \Theta = 0\end{aligned} \tag{A.4}$$

A.2 MAXIMA Code

The expressions for α^c, α^s, β^s, and γ^c are obtained by using the linear solver in MAXIMA [166]. The code used to generate them is shown here. The expressions are passed as strings to GNU Octave where code is executed to determine the critical thickness for the core-shell system [167].

```
reset()$
kill(all)$
debugmode(false)$
keepfloat:true$

/*Define the displacements*/

urc:Ac*r$
uzc:Ec*z$
urs:As*r+Bs/r$
uzs:Ec*z$

/*Define their derivatives*/

durdrc:diff(urc,r)$
duzdzc:diff(uzc,z)$
durdrs:diff(urs,r)$
duzdzs:diff(uzs,z)$

/*Write the misfit strains*/

arc$azc$ars$azsm$
mr:(ars-arc)/ars;
mz:(azs-azc)/azc;

/*Write the total elastic strain in each layer*/

gamma:acr/ars$
omega:acz/az
erc:durdrc$
ers:gamma*(durdrs-mr)$
etc:urc/r$
ets:gamma*((urs/r)-mr)$
ezc:duzdzc$
ezs:Omega*(duzdzs-emo_sz)$

/*Write the stress equations*/
```

```
s1:sigma_rc=c11c*erc+c12c*etc+c13c*ezc$
s2:sigma_rc=c11s*ers+c12s*ets+c13s*ezs$
s3:sigma_rc=c12c*erc+c11c*etc+c13c*ezc$
s4:sigma_rc=c12s*ers+c11s*ets+c13s*ezs$
s5:sigma_rc=c13c*erc+c13c*etc+c33c*ezc$
s6:sigma_rc=c13s*ers+c13s*ets+c33s*ezs$

/*Displacement continuity at interface*/
i:subst(Rc,r,urc-urs=0);

/*No net force perpendicular to z*/
integrate(integrate(s5*r,r,0,Rc),theta,0,2*pi)
+integrate(integrate(s6*r,r,Rc,R),theta,0,2*pi)$
iii:rhs(%)=0;

/*No net force on the surface perpendicular to r*/
iv:rhs(subst(R,r,s2))=0$

/*The stress is continuous at the interface r=R*/
v:subst(Rc,r,rhs(s1))-subst(Rc,r,rhs(s2))=0$

/*Collect like terms in the boundary condition expressions */
i_f:facsum(i,As,Ac,Bs);
iii_f:facsum(iii,As,Ac,Ec);
iv_f:facsum(iv,As,Bs,Ec);
v_f:facsum(v,As,Ac,Bs,Ec);

/* Initiate the linear solver */
sol:facsum(linsolve([i_f,iii_f,iv_f,v],[As,Ac,Bs,Ec]),R)$
As_f:rhs(sol[1])$
Ac_f:rhs(sol[2])$
Bs_f:rhs(sol[3])$
Ec_f:rhs(sol[4])$

/*Generate the expressions for strain*/
ersf:float(subst([Bs=Bs_f,As=As_f,r=Rc+S],ers)),numer$
etsf:float(subst([As=As_f,Bs=Bs_f,r=Rc+S],ets)),numer$
ezsf:float(subst([sol[4],r=Rc+S],ezs)),numer$

/*Export the strain expressions as strings*/
stringout("~nw_rsstrain.m",ersf)$
printfile("~/nw_rsstrain.m")$
```

```
stringout("˜nw_tsstrain.m",etsf)$
printfile("~/nw_tsstrain.m")$
stringout("˜nw_zsstrain.m",ezsf)$
printfile("~/nw_zsstrain.m")$

/* Solve for the strain energies */
ic:facsum((rhs(s1)*erc)+(rhs(s3)*etc)+(rhs(s5)*ezc))$
(1/(2*Rc))*integrate(ic*r,r,0,Rc)$
Ecf:subst([Ac=Ac_f,Ec=Ec_f,R=Rc+S],%)$
is:facsum((rhs(s2)*ers)+(rhs(s4)*ets)+(rhs(s6)*ezs))$
(1/(2*Rc))*integrate(is*r,r,Rc,R)$
Esf:subst([Ec=Ec_f,As=As_f,Bs=Bs_f,R=Rc+S],%)$

/* Export the strain energy expressions as strings*/
stringout("~/nw_cenergy.m",Ecf)$
printfile("~/nw_cenergy.m")$
stringout("~/nw_senergy.m",Esf)$
printfile("~/nw_senergy.m")$
```

A.3 GNU Octave Code

GNU Octave is an free, open source interpreted language intended for numerical computations [167]. The stiffness constants and lattice constants are generated based on the composition of the shell ($Al_xIn_{1-x}As$ or $Al_xIn_{1-x}P$). The expressions for strain energy are then imported from the MAXIMA code outlined in Section A.2 and vectorized. The strain energy is compared to the dislocation energy, and the critical thickness is determined based on the lowest energy criterion as explained in the thesis in Chapter 4.

```
clear all
x=input("Alloy fraction between 0 and 1?");
choose_shell=input ("AlInAs=1, AlInP=2, Choose a shell material! ");
%Import the lattice constants
[ao_cr,ao_sr,ao_cz,ao_sz]=nw_vegard(x,choose_shell);
[cAlInP,cAlInAs,CWZ]=nw_tensorrot(x);
        c11c=CWZ(1,3)*1e9;
        c33c=CWZ(2,3)*1e9;
        c12c=CWZ(3,3)*1e9;
        c13c=CWZ(4,3)*1e9;
        c44c=CWZ(5,3)*1e9;
        c66c=CWZ(6,3)*1e9;

if choose_shell==1
%Import the stiffness coefficients
  shell='AlInAs';
  c11s=cAlInAs(1)*1e9;
  c33s=cAlInAs(2)*1e9;
  c12s=cAlInAs(3)*1e9;
  c13s=cAlInAs(4)*1e9;
  c44s=cAlInAs(5)*1e9;
  c66s=cAlInAs(6)*1e9;
elseif choose_shell==2
  shell='AlInP';
  c11s=cAlInP(1)*1e9;
  c33s=cAlInP(2)*1e9;
  c12s=cAlInP(3)*1e9;
  c13s=cAlInP(4)*1e9;
  c44s=cAlInP(5)*1e9;
  c66s=cAlInP(6)*1e9;
end
Q=1e-10:1e-11:50e-9; %Core radius
S=1e-10:1e-11:50e-9; %shell thickness
L=750e-9; %core length
```

```
fid = fopen ("nw_senergy.m");
e_temp = fgetl (fid);
fclose (fid);
U_s=vectorize(inline(e_temp));

fid = fopen ("nw_cenergy.m");
e_temp = fgetl (fid);
fclose (fid);
U_c=vectorize(inline(e_temp));

c13bar=sqrt(c11s*c33s);
Kn=(c13bar+c33s)*sqrt((c44s*(c13bar-c13s))/(c11s*(c13s+2*c44s+c13bar)));
a=Q; %core radius, or distance to interface
bperp=ao_sz; %burgers vector perpendicular to basal plane
bpar=ao_sr;
A=2*pi.*Q.*L; %interfacial area

U_cd=zeros(length(Q),length(S));
U_sd=zeros(length(Q),length(S));
W=zeros(length(Q),length(S));

for i=1:length(S)
    U_sd(:,i)=U_s(Q, S(i), ao_cr, ao_cz,
                  ao_sr, ao_sz, c11c, c11s, c12c, c12s);
    U_cd(:,i)=U_c(Q, S(i), ao_cr, ao_cz,
                  ao_sr, ao_sz, c11c, c11s, c12c, c12s);
    W(:,i)=(Kn*bperp^2)/(4*pi*L)
                  *log(((32.*a)/bperp)-2);
end

U_str=U_cd+U_sd; %Q rows S columns
U_tot=U_str-W;
out = zeros(length(Q),2);

for i=1:length(S) %loop across columns of shell thickness
    j=1;
        while U_tot(j,i)<0%test if U_str<W
          j++;
            if j>=length(Q) %don't exeed index
              break
            end
        end
```

```
    out(i,2)=1e9*S(j);%critical shell thickness
    out(i,1)=1e9*2*Q(i);%core diameter at critical shell thickness
end

filename = strcat(shell,num2str(x));
save('-ascii', filename, 'out')

function[ao_cr,ao_sr,ao_cz,ao_sz]=nw_vegard(x,choose_shell)

%InAs, InP, AlAs, AlP wurtzite lattice constants
  ao_InAs=6.0583e-10/sqrt(2);
  ao_InP=5.8687e-10/sqrt(2);
  ao_AlAs=5.66139e-10/sqrt(2);
  ao_AlP=5.4510e-10/sqrt(2);
  co_InAs=(sqrt(8/3))*ao_InAs;
  co_AlAs=(sqrt(8/3))*ao_AlAs;
  co_AlP=(sqrt(8/3))*ao_AlP;
  co_InP=(sqrt(8/3))*ao_InP;

%output the lattice core and shell-ternary lattice constants based on
%user selection
if choose_shell==1

  ao_cr=ao_InAs;
  ao_sr=ao_AlAs*x+((1-x)*ao_InAs);
  ao_cz=co_InAs;
  ao_sz=co_AlAs*x+((1-x)*co_InAs);

elseif choose_shell==2

  ao_cr=ao_InP;
  ao_sr=ao_AlP*x+((1-x)*ao_InP);
  ao_cz=co_InP;
  ao_sz=co_AlP*x+((1-x)*co_InP);

end

function[cAlInP,cAlInAs,CWZ]=nw_tensorrot(x);
%Tensor rotation to obtain WZ stiffness
%constants from ZB values
%     c11   c12   c44
%InP
%AlP
```

```
%InAs
%AlAs
C=[   101.1 56.1  45.6;
      188.3 67.1  36.9;
      83.29 45.26 39.59;
      119.9 57.5  56.6];
%CZB=[c11 c12 c12 0 0 0 ;
%    c12 c11 c12 0 0 0 ;
%    c12 c12 c11 0 0 0 ;
%    0 0 0 c44 0 0 ;
%    0 0 0 0 c44 0 ;
%    0 0 0 0 0 c44]
;
P=(1/6)*[3 3 6; 2 4 8;1 5 -2;2 4 -4;2 -2 2; 1 -1 4];
Q=(1/(3*sqrt(2)))*[1 -1 -2];
Delta=Q*C';
barCWZ=P*C';

for i=1:4
D(i,:)=[
        Delta(i)^2/barCWZ(5,i)
        0
        -Delta(i)^2/barCWZ(5,i)
        0
        Delta(i)^2/barCWZ(1,i)
        Delta(i)^2/barCWZ(5,i)
        ];
end

CWZ=(barCWZ'-D)'; %with internal strain compensation D
%output c11 c33 c12 c13 c44 c66 for InP AlP InAs AlAs
%***************************
%cAlInP(As) c11 c33 c12 c13 c44 c66

for i=1:length(CWZ)
    cAlInP_t=x*CWZ(i,2)+(1-x)*CWZ(i,1);
    cAlInP(i)=cAlInP_t;
    cAlInAs_t=x*CWZ(i,4)+(1-x)*CWZ(i,3);
    cAlInAs(i)=cAlInAs_t;
end
```